THE TEMPORAL CORRELATABILITY OF DIGITAL THERMAL INFRARED SCANNER DATA

By

EDMUND HENRY CONROW

Bachelor of Science
University of Arizona
Tucson, Arizona
1971

Master of Science
University of Arizona
Tucson, Arizona
1974

Submitted to the Faculty of the Graduate College
of the Oklahoma State University
in partial fulfillment of the requirements
for the Degree of
DOCTOR OF PHILOSOPHY
December, 1976

THE TEMPORAL CORRELATABILITY OF DIGITAL

THERMAL INFRARED SCANNER DATA

Thesis Approved:

Bennett Basore
Thesis Adviser

J. K. Norton

Gerald D. Parker

Zuhair al-Shaieb

Norman N. Durham
Dean of the Graduate College

ACKNOWLEDGEMENTS

Among the many people who helped the author in this work, he would like to thank the following individuals and groups for their assistance:

Dr. Bennett Basore, doctoral committee adviser, associate dean of instruction, College of Engineering, Oklahoma State University, for his help in the pattern recognition, change detection and theoretical aspects of this work;

Dr. Joseph Norton, doctoral committee chairman, department head, School of General Engineering, Oklahoma State University, for his confidence and assistance to me as an engineer and student;

Dr. Zuhair Al-Shaieb, doctoral committee member, associate professor, Department of Geology, Oklahoma State University, for his help in the geological and statistical analyses in this work;

Dr. Jerald Parker, doctoral committee member, professor, School of Mechanical and Aerospace Engineering, Oklahoma State University, for his help in the thermal radiation theory and applications portion of this work;

The entire staff of the University Computer Center, Oklahoma State University, for their help and patience in the data processing used in this work;

Dr. Ronald Oines, research scientist, Cities Service Corporation, Tulsa, Oklahoma, for his broad help in data processing and applied remote sensing in this work;

Dr. Dave Pitts, research scientist, NASA-JSC, Houston, Texas, for his help and support in pursuing this research;

Health Applications Group, Life Sciences Directorate, NASA-JSC, and Lockheed Electronics Company support personnel, NASA-JSC, Houston, Texas for their data support and processing assistance;

Mr. Everett Thompson, research analyst, Lockheed Electronics Company, NASA-JSC, Houston, Texas, for his substantial data processing and analysis assistance;

The entire staffs of the Research Data Facility (READAF) (L-IX), Project Support Office (PSO) (Bldg. 17) and Project Support Facility (PSF) (Bldg. 17), NASA-JSC, and Lockheed Electronics Company Support personnel, Houston, Texas, for their broad documentation support;

The Spaceflight Meteorology Group (Bldg. 30), National Weather Service, NOAA and NASA, NASA-JSC, Houston, Texas, for supplying the NOAA-3 emphemeris data and orbital plotting board used in this work;

Mr. Russell Koffler, research analyst, National Environmental Satellite Service, NOAA, Suitland, Maryland, for his data support assistance;

Mr. Frank Kniskern, research analyst, National Environmental Satellite Service, NOAA, Suitland, Maryland, for his data support assistance;

Dr. Richard Legeckis, research analyst, National Environmental Satellite Service, NOAA, Suitland, Maryland, for his assistance in quantifying some of the non-linear geometric distortions present in the data.

Mr. Larry Breaker, research analyst, National Environmental Satellite Service, NOAA, San Francisco, California, for supervising

the NOAA-3 data acquisition; and Mr. Richard Hodur, graduate student, Department of Meteorology, University of Oklahoma, for his help in the meteorological analyses performed in this work.

The author also wishes to thank his parents for their assistance and support over the several years he has been in school, and the Office of the Dean, College of Engineering, and School of Civil Engineering, Oklahoma State University, for financial support which aided this research.

TABLE OF CONTENTS

LIST OF TABLES

LIST OF FIGURES

NOMENCLATURE

A = pixel area

A_D = along-track pixel dimension

A_S = along-track pixel spacing

A_{sc} = ascending satellite mode (night)

B = crosscorrelation shift index

C = crosscorrelation shift index

C_D = cross-track pixel dimension

C_S = cross-track pixel spacing

C_n = constant

D = diameter of the microwave antenna

D_e = descending satellite mode (day)

$Disp_a$ = the along-track displacement in the data due to the earth's rotation

$Disp_c$ = the cross-track displacement in the data due to the earth's rotation

E = expected value

EU = the line error in the new coordinate system present due to neglecting the non-linear scan angle and curvature effects

EV = the column error in the new coordinate system present due to neglecting the non-linear scan angle and curvature effects

H_0 = radiometer altitude

$H_T(Z)$ = atmospheric transmission as a function of zenith angle

IR = infrared

$I(U,V)$ = computed intensity value at an output point in (U,V)

J = number of sets of ground control points used in data registration

K = number of terms used in data registration

K_1 = perpendicular displacement between two adjacent scan lines due to the earth's rotation

K_2 = parallel displacement between two adjacent scan lines due to the earth's rotation

L = number of 200 column increments in data

L_D = distance between untransformed scan lines at nadir

M = mean

MAD = mean absolute difference

MBD = mean-biased difference

M_D = mean of a difference "vector"

MSV = mean square value

N_a = the total number of scan lines (X_{total}) in the data transformed to (U,V)

NEΔT = noise equivalent differential temperature

P = representation of a data point between coordinate systems

P_i = thermal inertia of the ground

P_s = satellite period

Q = the angle of inclination in retrograde of the satellite's orbital plane

R = ratio of Y_{ver} spacing distances

RMS = root mean square

R_{approx} = linear approximation of ratio of Y_{ver} spacing distances

R_e = radius of the earth

S = radiometer sampling rate

SD = straight difference

SI = sample (pixel) number in untransformed data

SNR = signal-to-noise ratio

S_O = solar constant

T = absolute temperature

T_{AD} = effective daytime air temperature

T_{AN} = effective nighttime air temperature

T_B = microwave brightness temperature

TCE = total column error between data sets

T_H = hotter temperature of area a_p

TLE = total line error between data sets

TRCE = total random column error between data sets

TRLE = total random line error between data sets

T_a = absolute atmosphere temperature

T_{av} = average temperature of the remainder of the pixel

T_c = corrected temperature of object scanned

T_g = absolute ground temperature

$T_{g,s}$ = absolute ground temperature in the sth interval

T_r = the earth's rotational period

T_s = absolute sky temperature

T_{se} = sensed temperature

U = new coordinate system lines

U_c = line distance from scene center in new coordinates

U_m = measured line location of a point in the new coordinate system

U_o = translation between old and new coordinate system lines

U_{ver} = line distance from scene center in new coordinates to the vertices

V = new coordinate system columns

V_c = column (pixel) distance from scene center in new coordinates

V_m = measured column location of a point in the new coordinate system

V_o = translation between old and new coordinate system columns

V_{ver} = column distance from scene center in new coordinates to the vertices

W = radiometer scan rate

X = along-track, old coordinate system lines

X_R = random variable

X_c = line distance from scene center in old coordinates

X_m = measured line location of a point in the old coordinate system

X_{ver} = line distance from scene center to the vertices contained in the transformed data

Y = cross-track, old coordinate system columns

Y_c = column (pixel) distance from scene center in old coordinates

Y_m = measured column location of a point in the old coordinate system

Y_{ver} = column (pixel) distance from scene center to the vertices contained in the transformed data

Y_0 = number of pixels (columns) between subsynch lines

Y_1 = number of pixels (columns) to the first subsynch line

Z = local zenith angle

Z_e = the element elevation relative to the datum

a_p = smaller ground area within a pixel, $a_p < A$

a_0, a_1, a_2 = constant registration coefficients

b_0, b_1, b_2 = constant registration coefficients

c_c = cloud cover factor

c_ℓ = speed of light

c_0, c_1, c_2 = constant registration coefficients

ds = along-track ifov of scanner

d_0, d_1, d_2 = constant registration coefficients

exp = 2.71828...

$e_{\lambda b}(\lambda)$ = blackbody hemispherical emissive power

f_i,$f_{i,j}$ = intensity computation coefficients

h = Planck's constant

i = incremental index

in = inverted atmospheric gradient

j = incremental index

k = Boltzman's constant

ℓ = total number of increments in a dimension

m = total number of increments in a dimension

n = noise component "vector"

nor = normal atmospheric gradient

n_p = number of points in a subscene

q = incremental step in flux calculations

r = reference pattern "vector"

s = time interval

sl = slight atmospheric gradient

t = test pattern "vector"

un = unstable atmospheric gradient

w = total number of increments

α = radiometer scan angle

α_i = constant

β = target angle to radiometer

β_i = constant

γ = earth center angle

ε = emissivity

ε_a = emissivity of the atmosphere

ε_{av} = emissivity of the remainder of a pixel

ε_g = emissivity of an object (ground)

ε_H = emissivity of an area a_p

ε_r = dielectric constant

ε_{se} = emissivity of the pixel

θ_i = angle between two vectors

θ_ℓ = angle of latitude

λ = wavelength of radiation

η_i = imagery scale factor

ζ = period of the thermal flux

ρ = correlation coefficient

ρ_g = reflectivity of an object (ground)

τ_i, τ_j = shift location in crosscorrelation

σ = Stefen-Boltzman constant

σ_D = standard deviation of a difference "vector"

σ_i = standard deviation of the registration error

$\sigma_{n/p}$ = standard deviation of the noise/point

σ_r = standard deviation of a reference "vector"

σ_{std} = standard deviation

σ_t = standard deviation of a test "vector"

σ_{TE} = standard deviation (temperature) of a data substring

σ_0 = standard deviation of a reference and test "vector" if statistically independent

ψ_{q-s-1} = set of coefficients determined by the number of incremental steps, q, in the period ζ

ϕ = imagery rotation angle between coordinate systems

ϕ_{An} = atmospheric heat transfer flux in the nth interval

ϕ_{Gn} = reradiation from the ground in the nth interval

ϕ_{Sn} = absorbed solar flux in the nth interval

ϕ_n = absorbed thermal flux in the nth interval

π = 3.14159...

$d\alpha$ = differential scan angle

$d\nu$ = cross-track ifov of scanner

$d\gamma$ = differential ground pixel angle

Δ = the incremental spacing distance in the data

$\Delta Disp_c$ = the difference in cross-track displacements between test site boundary latitudes

ΔE_d = the resulting displacement at ground scale in the untransformed data from elevation relief due to scan angle effects

ΔEU = the differential line error in new coordinates due to neglecting non-linear scan angle and curvature effects between data sets

ΔEV = the differential column error in new coordinates due to neglecting non-linear scan angle and curvature effects between data sets

ΔT = point-by-point difference temperature

ΔT_a = loss temperature through the atmosphere

$\Delta U, \Delta V$ = difference between the measured and predicted location in the new coordinate system at any X,Y in the old coordinate system

$\Delta X, \Delta Y$ = difference between the measured and predicted location in the old coordinate system at any U,V in the new coordinate system

Δz = equivalent ground track sampling interval (ifov in X or Y)

LIST OF PROGRAMS UTILIZED IN THIS WORK

"CROSS" --Performs a two dimensional crosscorrelation between digital data sets of size ℓ by m. The algorithm utilizes eq. 2.18, is normalized and compensates for the pyramid effect.

"GREY" --Produces a pictoral simulation by a line printer using a densenometric range of preselected characters that vary from blank (light) to a set of eight multiple overstrikes (dark). Here, a linear relationship exists between the specified number of input ($\geq$ 1) data and computed output ($\leq$ 21) levels.

"GREYEXP" --Same as "GREY" except uses an exponential or logarithmic function to determine the relationship between input and output levels.

"NIGHT" --Given the transformation coefficients from "TRNSFM" it computes the magnitude of a location in (U,V) from (X,Y) with bilinear interpolation. Designed for use with night data edits.

"NOAA" --Reformats data from "UNSPEC" for use with "NIGHT" or "NOAATR".

"NOAADIFF"--Determines the point-by-point difference temperatures between two data sets. Processing utilizes eqs. 2.28 and 2.32 to generate straight and mean-biased difference temperatures, computes the data set means, and classifies each (straight and mean-biased) ΔT point into one of seven

classes given in Table IV. Resulting (U,V) point-by-point output is straight and mean-biased difference temperatures (sign and magnitude preserved) and classes.

"NOAATR" --Same as "NIGHT", but used with day data edits.

"PLOTCL" --Used to produce a line printer plot of classified data. Here, each class having previously been assigned an integer number (≥ 1) is represented by a standard IBM symbol. The resulting spatial output plot contains a symbol at each point within a designated class, and a blank at those locations where a points' class was not specified. As few as 1 or as many as "ALL" possible classes may be printed on one form.

"TRNSFM" --A CPS program used to determine transformation coefficients between old and new (or vica-versa) coordinate systems. In the three term (linear) case used in this work eqs. 2.11 thru 2.14 were utilized for registration.

"UNSPEC" --Used to transfer the magnitudes and signs of a selected area on a CCT to another tape for additional processing. The desired locations of the scene pulloff are input; specifically the first record (line) number, first column (pixel) number, total number of records and the sub-block size utilized (related to the total number of columns). Additional features include a level (energy or temperature)--frequency histogram of the transferred area, printout of the magnitudes of the pixels in the last line of the data transferred (up to 800 columns), and the calibration data for that line.

CHAPTER I

INTRODUCTION AND STATEMENT OF PROBLEM

Various forms of position-locating systems have been proposed in recent years, many of high accuracy and sophistication. One fundamental concept is determining location by reference to recognizable landmarks. Position-locating systems based on this concept are under development and have stimulated research into automatic pattern recognition techniques.

There appears to be agreement that the process of pattern recognition is similar to that modeled mathematically by crosscorrelation. Other concepts of pattern matching have been proposed, but each is similar in that an effort is made to locate invariants between reference and test scenes.

The purpose of this work is to investigate the feasibility of a method of pattern recognition which will use input data from a scanning radiometer. Given that some optimal data (spectral and spatial) is available, it can be processed with reference or predicted data to accomplish pattern recognition and from the recognition information, infer the location. If the degree of correlation between reference and test sets is below acceptable limits, however, the implied concept fails and accurate position fixes would not be obtained.

Inherent in performing this work is the availability of suitable data to be used in the experimental analysis. There are two primary

considerations in initially selecting the proper data type. First is the proper spectral choice of data that will contain sufficient information to allow a nontrivial analysis over a variety of physical and environmental factors (i.e., diurnal, seasonal and meteorological Second is the selection of an adequate (spatial) resolution element area to use in the experimental analysis.

The appropriateness of various types of remote sensing data that could be utilized in the experimental analysis must be carefully considered. Because of the various wavelength dependent limitations imposed on the use of data generated in the electromagnetic spectrum the question arises: what wavelength interval would be optimum for use in the experimental analysis? Although in initial stages radar data could be utilized in the experimental analysis, an actual position-locating system should preferably be passive to avoid detection (for military purposes); hence active techniques such as radar and lasers would not be considered. The wavelength of spectral measurements is limited in a practical sense to that of visible light and longer due to the lack of suitable atmospheric windows and increased photon energy (increased scattering and high energy interactions) in the hard ultraviolet and shorter wavelengths.

The use of visible wavelengths in such a system might be adequate in some circumstances, but poor bad weather penetration and the inability to be utilized during darkness (except near large man-made areas) would limit its application as an all-purpose system. In addition to these factors a pronounced seasonal effect (i.e., spectral changes of vegetation) would hamper the experimental use of this data. Reflective near-infrared data, while capable of providing useful

terrain related information (i.e., vegetation discrimination), is susceptable to most of the same environmental constraints as visible data. Middle infrared data is useful for thermal investigation of terrain hot spots (i.e., forest fires and volcanoes), but because of the low emitted power in this spectral region at the ambient temperatures of most terrain features, a middle-IR scanner would not be applicable in a high signal-to-noise ratio (SNR) position-fixing system that requires diurnal operation.

The two realistic remaining choices for experimental data are in the thermal infrared (IR) and microwave parts of the spectrum. In commonly used thermal IR wavelengths (8μ-14μ) diurnal data can be readily obtained and is less sensitive to most environmental constraints than visible data. Thermal IR imagery, however, is not suitable for bad weather applications as it has only moderate cloud penetrating capabilities. Microwave data is more desirable than thermal IR in some respects; particularly its relative insensitivity to weather conditions. Its disadvantages, however, include a moderate sensitivity in perceived brightness temperature change as a function of soil moisture content and scanning wavelength, and general lack of availability except in high resolution low altitude and low resolution orbital altitude form.

Another factor that must be considered is the resolution size of the data. In this work the "highest" resolution data available might not be more desirable than "low" resolution data within the same wavelength interval. Since the amount of data generated to cover a given area increases inversely as the square of the resolution size, a very high resolution scanner can produce a serious data management problem. Although cultural features may be difficult to detect in low resolution

data, their frequency of occurrence in undeveloped regions could be so low as to negate any benefit from the use of high resolution data to detect and use them on a global basis. In effect, then, the resolution size should be chosen so that it does not eliminate textural features nor create a data management problem by being too small. Certainly here (as in other types of research) many trade-offs exist in determining an optimal data type (spectral and spatial) for evaluation; unfortunately this choice is often difficult to make.

After these two factors are evaluated to determine an optimal data type, a representative reference set for each region must be chosen for the pattern-matching analysis. If a crosscorrelation analysis is utilized in this procedure then the resulting magnitude peak between reference and test sets must always have a high enough SNR to allow hardware system operation. If an "unrepresentative" reference scene is correlated with test data a low magnitude peak may result. This fluctuation from an acceptable SNR could cause a hardware system malfunction and loss of position-fixing ability. In addition to this factor it is necessary that the resulting crosscorrelation magnitude peak between a reference and test set be unambiguous. Any ambiguity in peak location would negate the use of this concept in a navagational guidance system since position and heading information are generated at each grid interval. Obviously if a test signal is unavailable because of some factor (i.e., diurnal or environmental), which causes an incompatability with the sensor system's dynamic range, a null or uncorrelated output could result. It is not necessary that only one reference pattern exist for a given area. Representative reference patterns, however, should exist for any predictable effect (i.e., diurnal, seasonal and

environmental). Obviously real-time processing requirements would increase proportionally to the number of reference patterns necessary to adequately describe a given region over a period of time. These requirements could pose a severe restriction on the development and implementation of this type of system.

Inherent in using radiometer data to experimentally investigate the correlatability between test and reference patterns is the assumption that the noise present is sufficiently low to avoid significant data quality degradation. Noisy data will affect the analysis in several ways; among these are decreased accuracy in the geometric registration of the patterns and a decreased correlation peak SNR due to the noise content of the data itself. Obviously, then, data considered "too noisy" is unusable in this type of analysis because of the resulting inaccuracies.

Due to a lack of readily available (diurnal and seasonal) microwave data this investigation was performed utilizing thermal IR (10.5μ → 12.5μ) very high resolution radiometer (vhrr) scanner data from the NOAA-3 satellite. The resolution element size was .91 km at nadir and the noise standard deviation (in terms of temperature) of typical scenes was $\leq .5^{o}C$, which was considered acceptable for this analysis.

In this work point-by-point differencing was to be used to determine the degree of similarity between data sets assuming that they could be geometrically registered. A goal here was to identify whether or not regions of thermal invariance could be detected within the test site. If these regions could be detected they would be revealed by being near zero ΔT in the difference patterns. The existence of

time-invariant "no-change" regions as small as a pre-determined minimum cell size could possibly form the theoretical basis for a thermal IR navigational guidance system. Even if only three recognizable "no-change" cells were available within a given regions they would potentially be adequate for local navigation (within that region) and could supply the necessary heading to maintain the proper course. (This is possible since three spatially linearily independent points contain translation, rotation and scale factor coefficients within their angular and distance relationships to each other.)

Of potential additional interest is whether or not "no-change" regions have a unique correspondence to the associated geology; such that the thermal signature of these regions is directly correlatable to some combination of their thermal and material properties.

A second possibility for the basis of a thermal IR navigational guidance system would be: if the thermal signature of the test site changed in a known and consistent manner then this effect could be compensated for within the system itself, thus ideally yielding a high correlation between the adjusted reference pattern and terrain below. Specifically if the two patterns can be geometrically rectified and if the only thermal difference between them is of their means, then this bias can be eliminated by software or hardware during processing.

In addition, this "mean-biased" concept would also be useful if it appeared that day reference scenes were better correlated to day test scenes than night test scenes, and visa versa, since such a factor could be compensated for by the selection of the appropriate reference pattern. One factor that could decrease the resulting crosscorrelation peak magnitude would be if anomalous high (±) temperature regions

appeared between the two registered patterns whose difference distribution was centered around the average ΔT. An additional factor that could affect correlation between patterns might be due to seasonal changes. If this change can be accurately predicted so that "thermally-representative" reference patterns exist to describe it then the correlation process would not be adversely affected.

Hence an important part of this analysis is to observe and quantify anomolous thermal regions and to see whether or not they exist on a temporal basis between various difference pairs. If these regions are common to several difference patterns, then it is an indication that a "thermally-unrepresentative" reference pattern was chosen which will decrease all the resulting correlations between reference and test pairs accordingly in which it was utilized.

The third possibility would be a concept based upon a combination of straight and mean-biased difference pattern features. A hypothetical combination might include those regions centered near the average ΔT that can be located repetitively (i.e., between all day/day and night/night cases after any necessary seasonal biasing) between difference sets, and certain additional regions near zero ΔT. Of course the proper selection and combination of features would have to be known for this approach to be valid. If this information is available, however, such a hybrid approach would allow the use of those aspects of each case which have the highest probability of occurrence, which could then form a stable method. The difficulty here lies in defining and verifying the existence of the minimum information necessary to adequately describe the thermal signature of the test area.

Objectives

It is proposed to study the correlatability of patterns obtained by terrain mapping with a scanning radiometer. Specific objectives are:

1. To determine whether or not invariant and/or mean-biased consistent thermal features on the earth's surface can be detected using current thermal IR scanning radiometer systems. In addition, if such regions exist, is the overall resulting correlation between pairs of patterns sufficiently high to warrant further investigation of this concept for position-locating systems?

2. To attempt to determine the effect of observed physical and environmental factors (i.e., diurnal, seasonal and meteorological) on the correlatability of reference and test pattern pairs.

CHAPTER II

BACKGROUND

Thermal Radiation Theory

The question may arise as to why remote sensing data was used in this analysis when physically measured surface information could suffice. It can be argued that since thermal IR scanner data primarily responds to the upper .1mm of the material surface contact thermometric measurements of the temperature would be accurate, particularly if the previous thermal history of the material is known. Here a set of samples (sufficiently large in volume to negate effects from the surrounding environment) could be measured by thermocouple certainly as accurate as the best thermal IR remote sensor data available; with the added advantage of almost unlimited remeasurement under a variety of physical and environmental circumstances. (This would be unwieldy for microwave measurements because of the much larger penetrating depths and the component due to sky reflection which can be affected by the properties of the surrounding area.) The primary disadvantage of this technique lies in the inconvenience of making many accurate contact measurements under various environmental conditions, chosing representative samples and constructing the measurement "park."

The use of remotely sensed data alleviates this measurement problem but by no means is perfect itself. Because the effect of the

atmosphere becomes greater with distance traversed through it, accurate compensation for this and other factors is needed.

A brief discussion of basic radiation theory in the thermal IR and microwave portions of the electromagnetic spectrum is given here. A more detailed analysis with examples is presented in Appendix A.

Planck's equation gives the hemispherical emissive power emitted by a blackbody at a given temperature as (Siegel and Howell, 1972, p. 19):

$$e_{\lambda b}(\lambda) = \frac{2\pi hc_{\ell}}{\lambda^5(e^{hc_{\ell}/\lambda kT} - 1)} \frac{\text{power}}{(\text{area})(\text{wavelength})} \qquad (2.1)$$

where h = Planck's constant, c_{ℓ} = the speed of light, k = the Boltzman constant, T = the absolute temperature of the object, λ = the wavelength of radiation. For $\lambda \simeq 10\mu$ the -1 term in the denominator can be eliminated (Wien's approximation), and integration of the resulting equation shows that emitted power in the thermal IR is proportional to the fourth power of absolute temperature. In the microwave region the exponential term in eq. 2.1 can be approximated by a truncated power series, giving the resulting relationship:

$$e_{\lambda b}(\lambda) = [\frac{2\pi kc_{\ell}}{\lambda^4}]T \frac{\text{power}}{(\text{area})(\text{wavelength})} \; . \qquad (2.2)$$

Hence in the microwave region the power emitted from a body is proportional to its absolute temperature.

Because of the relatively small amount of energy available from the radiating sun at thermal IR (< .1%) and microwave wavelengths ($<10^{-9}$%) reflective solar components in these spectral regions are minimal. Because of high emissivities (ratio of the emissive power of an object to that of a blackbody) of most materials in the thermal IR,

the energy received at the detector in this region is a representation of the thermal flux balance of the surface being scanned. In the daytime the flux absorbed into the ground is related to the net incident shortwave solar flux absorbed, plus the atmospheric heat transfer flux absorbed, minus the reradiated ground flux. At night the net incident solar flux is zero, and the net flux absorbed into the ground is given by the atmospheric heat transfer flux absorbed, minus the reradiated ground flux.

In the microwave portion of the spectrum the energy balance of a surface is primarily related to the components from its emissivity and absolute temperature, and reflectivity and sky temperature. Assuming a cloudless sky and no transmission through the earth the microwave brightness temperature is given by:

$$T_B = \varepsilon_g T_g + \rho_g T_s \quad , \tag{2.3}$$

where ε_g and ρ_g are the emissivity and reflectivity of the object, and T_g and T_s are the absolute ground and sky temperatures. Hence the brightness temperature is the sum of emitted and reflected radiation components. In the microwave region, water and metals have low emissivities, hence their perceived brightness temperature is usually very low since the $\rho_g T_s$ component dominates. Because of this, microwave or radar scanners are often used in military reconnassaince work for detecting man-made (metallic) objects. A potential limiting factor, however, in the use of microwave remote sensing data is the sensitivity of T_B to soil moisture content. Because of the relatively high reflectivity of water, changes in the amount of soil moisture/water content present in an object will be perceived as changes in the brightness

temperature. Specifically as the soil moisture content of the object increases, T_B decreases. In addition, because of the increased penetration depths of microwave radiation, the properties of subsurface regions may have a direct effect on T_B.

The scanning wavelengths commonly employed in both the thermal IR and microwave regions are located in atmospheric windows which have relatively low attenuation for radiation transmitted through them. In bad weather, however, due to the increased concentration of aerosols (water droplets, etc.), anomolous attenuation increases and the strength of the transmitted signal decreases. Since the diameter of water droplet aerosols in most clouds is $\geq$ the wavelength of thermal IR radiation, significant signal attenuation in this spectral band can occur. (For visible wavelengths the attenuation in this case would be several times larger than for thermal IR wavelengths.) For microwave wavelengths, however, the dimension of the scanned radiation is often significantly greater than the aerosol diameter and less attenuation occurs. Microwave radiation even possesses a fair penetration of precipitating rain clouds and a good penetration of snow. Because of this property the microwave region is a better "poor-weather" penetrating wavelength band than the thermal IR, but in good weather both wavelength regions are adequate for remote sensing purposes.

Thermal IR data is directly affected by diurnal and seasonal influences since the emissive power of an object is proportional to the fourth power of its absolute temperature in this spectral region. Hence, as these factors influence the surface temperature, so do they influence the scanned signal from the object. In the microwave region a similar effect is present when $\varepsilon_g >> \rho_g$. Here $T_B \simeq \varepsilon_g T_g$ and diurnal

seasonal factors that influence the absolute ground temperature (T_g) can have a direct effect on the perceived brightness temperature, particularly for materials with low water concentrations or porosity.

Because of the long scanning wavelengths in the microwave portions of the spectrum, large receiving antennas are required. In most applications, however, antenna sizes (diameters) must be limited, and the angular resolution of the scanner system is diffraction limited and given by:

$$d\nu \simeq \lambda/D \tag{2.4}$$

where $d\nu$ = the crosstrack ifov,

λ = the wavelength of radiation, and

D = the diameter of the antenna.

Because of this, resolutions utilized in the microwave region are often several times poorer than those available in the thermal IR. In addition, the microwave brightness temperature of an object is somewhat dependent on the scanning wavelength; particularly for materials containing significant amounts of water. (This is caused by the wavelength dependence of reflectivity of water in this region.) Furthermore T_s is also dependent on the microwave scanning wavelength; the result of this being that a test site scanned by one microwave radiometer may provide brightness temperature information considerably different than from another radiometer operating at a different scanning wavelength at the same time.

Even though microwave brightness temperature data is sensitive to scanning wavelength, water content (of the object), and degraded resolution (compared to thermal IR), its bad weather penetrating capabilities make it an attractive wavelength region to obtain the necessary

data for this analysis. Because such microwave data was not available, however, high quality thermal IR data was utilized instead for this work.

In this work, the following nomenclature is used to designate the temperature of an object. Since a blackbody is a perfect emitter, its temperature is absolute and given by T. The atmospheric corrected scene temperature used in this research, T_c, assumes that the terrain scanned is a blackbody. (Since in the thermal IR the emissive behavior of most natural materials approaches a blackbody, this assumption is reasonably accurate.) Finally, in microwave applications, absolute ground temperatures are designated as T_g to indicate one component of the perceived brightness temperature, T_B. (Other components of T_B are the absolute sky (T_s) and atmosphere (T_a) temperatures.) In the thermal IR analyses performed in this work the author assumes $T = T_c$ ($= T_g$), and consequently $\Delta T = \Delta T_c$ ($= \Delta T_g$). (From eq. 2.3 $T_B \neq T_g$ and these temperatures are only similar if T_s is small and $\varepsilon_g \simeq 1$.)

Geometric Registration

Since remote sensing data obtained from a moving platform is subject to the (reference system) coordinates of the platform, a transformation procedure is often employed to geometrically register the scanner data to a reference image or standard projection. In temporal analyses this procedure is mandatory, otherwise substantial alignment errors may degrade the accuracy of the resulting operations.

There are two common types of image registration utilized. The first employs registering successive images to a reference set. This is often utilized when accurate maps are not available, but is limited

by the necessity to locate identical (or at least local) ground control points (g.c.p.'s) between two or more different scenes. (In temporal data analysis of visible band imagery on a seasonal basis this may be a severely restricting factor due to spectral changes of vegetation.) The second (and probably better) technique requires that all data sets are registered to a standard projection (usually cartesian, orthogonal). In this case it is not necessary to locate the same g.c.p.'s, and in addition, measurements can be made from the image (old coordinate system) to the map (new coordinate system which has identical scale in both dimensions), to allow the initial evaluation of potential g.c.p.'s.

Specifically, the X and Y scale of the old coordinate system (η_1,η_2) (see below) can be determined by computation from distances between known points on the image and comparison to distances on the map (where $\eta_1 = \eta_2 = \eta$). From this an initial check can be made to eliminate any g.c.p.'s with large variations between a predicted (from distance between points on map and knowing η_1, η_2 on the image) and measured (on image) distance due to measurement errors. In temporal analyses where η_1 and η_2 in the old coordinate system may vary significantly between data sets, this second technique can be more accurate than the first.

The three geometric corrections most commonly employed are translation, rotation and scale factor. Translation errors occur if a test site is imaged and the platform travels off of the plane of symmetry in the along-track path (i.e., the vehicle is not centered over the axis of symmetry of the test site during scanning). Rotation errors are generally due to a non-zero azimuth between the symmetry axis and heading of the platform. A scale factor is present in all remote sensing

data and is the ratio of the observation size of the medium to the actual ground scan size.

If these factors are approximately linear in the data (assuming negligible non-linear platform and scanning distortions) they can be readily determined and compensated for. If the intention of the analysis is to register a data set to a standard projection (i.e., UTM Grid Lines) then a set of coefficients will define each point in the old coordinate system of the scanned data (two dimensional) into a location in the map (new coordinate system; also two dimensional) where the exact position is determined from the mapping functions of translation, rotation and scale factor.

These mapping equations are generally known as conformal similarity equations and are of the form (Baker and Mikhail, 1975, p. 202):

$$U = \eta_1(X\cos\phi_1 + Y\sin\phi_2) + U_0 \tag{2.5}$$

$$V = \eta_2(-X\sin\phi_1 + Y\cos\phi_2) + V_0 \tag{2.6}$$

where X and Y = the 2-dimensional position of a data point in the old coordinate system,

U and V = the computed 2-dimensional position of a data point in the new coordinate system,

U_0 and V_0 = translations between the old and new coordinate axes,

ϕ_1 and ϕ_2 = the rotation angles between the two systems, and

η_1 and η_2 = the scale factors between the two systems.

In remote sensing data obtained from a platform with good attitude control $\phi_1 \simeq \phi_2$ and $\eta_1 \simeq \eta_2$. In some satellite imagery, however, where significant panorama distortion may be present $\phi_1 \neq \phi_2$ and $\eta_1 \neq \eta_2$. A

detailed analysis of non-linear distortions present in the vhrr data used in this work is given in Appendix B.

By combining rotational and scale factors in equations 2.5 and 2.6 another form directly yields the necessary registration factors between coordinate systems by fitting a low-order bilinear distortion model to the subimage being investigated. (In this work the scene is represented as a single subimage, and non-linear local and global distortions are not removed.) This model is of the general form (Riffman, 1973):

$$U = a_0 + a_1X + a_2Y \tag{2.7}$$

$$V = b_0 + b_1X + b_2Y \tag{2.8}$$

where a_0, ... a_2, b_0, ... b_2 = constants. For the reverse transformation case the variables X and U, and Y and V are respectively interchanged in eqs. 2.7 and 2.8 so that:

$$X = c_0 + c_1U + c_2V \tag{2.9}$$

$$Y = d_0 + d_1U + d_2V \quad . \tag{2.10}$$

where c_0, ... c_2, and d_0, ... d_2 are constants.

A commonly used method for the implementation of this technique is to devise an algorithm to solve J sets of K (equal to the number of terms) simultaneous equations to obtain the constant coefficients. In this linear case, potential g.c.p.'s are entered in sets of three (K = 3); a total of J sets.

Based on equations 2.7 through 2.10, a method is presented for determining the error between measured and computed locations in either coordinate system. The primary use of this is to check the accuracy of

a potential g.c.p. between the old and new coordinate systems. These equations are of the form:

$$U_m - U = \Delta U = \bar{a}_0 + \bar{a}_1 X + \bar{a}_2 Y \qquad (2.11)$$

$$V_m - V = \Delta V = \bar{b}_0 + \bar{b}_1 X + \bar{b}_2 Y \qquad (2.12)$$

where ΔU, ΔV = difference between the measured and predicted location in the new coordinate system at any X,Y in the old coordinate system;

U_m, V_m = measured location of a point in the new coordinate system;

U, V = computed location of a point in the new coordinate system; and

$\bar{a}_0, \ldots \bar{a}_2, \bar{b}_0, \ldots \bar{b}_2$ = mean of the J constants for each coefficient.

Likewise a similar relationship between the new and old coordinate systems can be generated by interchinging (X,Y) for (U,V) and ($\bar{c}_0, \ldots \bar{c}_2$ and $\bar{d}_0, \ldots \bar{d}_2$) for ($\bar{a}_0, \ldots \bar{a}_2$, and $\bar{b}_0, \ldots \bar{b}_2$) as:

$$X_m - X = \Delta X = \bar{c}_0 + \bar{c}_1 U + \bar{c}_2 V \qquad (2.13)$$

$$Y_m - Y = \Delta Y = \bar{d}_0 + \bar{d}_1 U + \bar{d}_2 V \quad . \qquad (2.14)$$

The representation of each potential g.c.p. in the J sets is P(X,Y,U,V) which provides coefficients and error determinations (ΔU, ΔV) from the old to the new coordinates, and P(U,V,X,Y) and (ΔX,ΔY) from the new to the old coordinates. Hence, J number of coefficients are computed for each constant; ($a_0, \ldots a_2$ and $b_0, \ldots b_2$) or ($c_0, \ldots c_2$, and $d_0, \ldots d_2$). The mean (simple average) of each set of constant

coefficients is then determined; ($\bar{a}_0$, ... $\bar{a}_2$ and $\bar{b}_0$, ... $\bar{b}_2$) or ($\bar{c}_0$, ... $\bar{c}_2$ and $\bar{d}_0$, ... $\bar{d}_2$). These means are used to compute the (ΔU, ΔV) or (ΔX, ΔY) discrepancies between the two coordinate systems (either old to new or new to old depending on the function order of the point (P)) for every g.c.p. entered (J times K or J times three in a three term linear case), as given in eqs. 2.11 through 2.14.

Once g.c.p.'s are determined accurately the data intensities are computed and registered to the image or projection in the new coordinate system. To perform this the acceptable g.c.p.'s are reverse transformed using eqs. 2.13 and 2.14. Here we are only interested in determining (X,Y) from (U,V) and the mean coefficients. The intensity value at a desired point (X,Y) in the old coordinate system is computed and then placed on the corrected grid location (U,V) of the new coordinate system. Several methods can be used to calculate the intensity value of the output point in (U,V) (an integer location only if local non-linear distortions are removed from the data.) For example (in discrete form) (Bernstein, 1976): the nearest-neighbor method, which selects the intensity of the closest input point (X,Y) and assigns that value to the output point (U,V):

$$I(U,V) = I(X,Y)\Big|^{\text{nearest neighbor}} . \qquad (2.15)$$

The bilinear interpolation method, which uses four neighboring input values to compute the output intensity (in (U,V)) by 2-dimensional interpolation:

$$I(U,V) = f_1 I(X,Y+1) + f_2 I(X,Y) + f_3 I(X+1,Y+1) + f_4 I(X+1,Y) . \qquad (2.16)$$

The cubic convolution method approximates the $\text{sinc}(X_r)$ function (with

$X_r \leq 2$), and thus uses 16 neighboring values in the two dimensional case to compute the output intensity (in (U,V)):

$$I(U,V) = \sum_{m,\ell} f_{m,\ell} I(X+m, Y+\ell), \quad -1 \leq m, \ell \leq 2 \quad . \qquad (2.17)$$

The processing rates decrease for an increase in the complexity of the three methods (eqs. 2.15 through 2.17). Hence processing rates are the highest for the nearest-neighbor algorithm, decrease for the bilinear interpolation routine and decrease further for the cubic convolution algorithm. In addition to this there is a difference in output data quality between the three algorithms. The nearest neighbor technique can result in assigning a data value as much as ±.5 line or column off from (X,Y) to (U,V). Thus, neither intensity nor slope continuity is preserved in the transformed image (X,Y to U,V). In the bilinear interpolation technique use of the four nearest neighbors preserves slope continuity (in U,V), but with slightly degraded resolution, due to the smoothing properties of this algorithm. Both slope and intensity values are preserved in the cubic convolution algorithm (from X,Y to U,V).

As implemented in this work, intensity computations were performed at integer locations in (U,V) with bilinear interpolation from locations determined in (X,Y) by eqs. 2.13 and 2.14. Consequently, the effect of non-linear geometric distortions was neglected to allow the use of a cartesian, orthogonal grid in (U,V) for the transformed data. Since these distortions were present in (X,Y), however, they also occurred in (U,V) and produced some slope discontinuity in the computed scene. In most cases, however, this was negligible since the rate of change of these distortions (i.e., scan angle effect and curvature)

within a subscene was small. Instead their major effect in (U,V) appeared as a registration "error" between measured and computed locations. Hence, the linear registration and bilinear interpolation technique utilized provides a processing trade-off; it does not remove non-linear geometric distortions present in the data, but does provide the desired (cartesian, orthogonal) grid relationship in (U,V) within an acceptable degree of accuracy. (In fact, since g.c.p.'s were often absent from certain positions of the test site (the western edge and four corners), no accurate local geometric correction would be possible in these regions even if a suitable technique (i.e., Kalman filter) was available for this purpose.)

Techniques are also available for image registration that do not depend on g.c.p.'s. Examples are Discrete Fast Fourier Transform cross-correlation (Anuta, 1970) and the Sequential Similarity Detection Algorithm (SSDA) (Barnea and Silverman, 1972). As implemented, these methods assume that a rough initial alignment exists between reference and test data sets, and are used to fine-align the images to each other. Both are sophisticated, and (may) thus present challenging problems in utilization and implementation. Furthermore they are only intended for use with sub-frames between data sets, as excessive processing requirements will result if used for large data arrays. Their complete description is beyond the scope of this work and the reader is referred to the thorough references given.

In this work, X and Y refer to untransformed lines (along-track) and columns (cross-track) respectively, while U and V refer to transformed lines and columns respectively. Individual elements are indexed (or referred to) in subscripted array notations; i.e., the jth element

(column) of the ith row would be given as (X_i,Y_j) and (U_i,V_j) in old and new coordinates respectively, from a (0,0) location. (Since reference and test scenes always refer to transformed data in this work, their element notation is simply given as $(r_{i,j})$ and $(t_{i,j})$ respectively.)

Change Detection

Given that the data sets have been properly registered to a standard projection, a technique such as change detection is desired for measuring thermal invariants. Basically, in using change detection we are interested in locating those regions that have a difference or mean-biased difference centered near zero. It is these "no-change" or "average-change" regions that exhibit pattern invariants in the data utilized. Hence "no-change" or "average-change" regions define isotherms between data set pairs and their occurrence can be used to determine whether or not a position locating system utilizing thermal IR data is feasible.

Change detection is usually defined as a search for differences (or similarities) between two or more spatially congruent data sets obtained at different times. Change detection is not (strictly) the same concept as that implied in a temporal statistical analysis. There exists in the literature articles dealing with the use of the temporal dimension as an independent variable together with spectral information to form a spectral or multispectral temporal array. The principle use of the temporal dimension in these cases has been to develop a time-dependent signature for crop and soil discrimination. This information was primarily used to implement temporal spectral classifiers to aid in

the identification of crop types over long periods of time, and not to locate significant (±) change, "no-change", or "average-change" regions (as a function of time). Though most of that work was performed in the visible and near-IR wavelengths, the fact that classification accuracies often improved when a temporal dimension was included suggests the seasonal effect in these spectral regions is significant. The widest use of change detection has been with military planners for reconnaissance evaluation purposes and land use planners for monitoring urban and agricultural changes over a period of time.

Both Control Data Corporation and the Westinghouse Defence and Space Center have developed change detection systems utilizing Side Looking Airborne Radar (SLAR) data with real-time processing capabilities. The Westinghouse System (Tisdale, 1971) can process one 1000 x 1000 element 4-bit byte, frame per second and is capable of recognizing up to 100 different classes after geometric registration and differencing.

The Control Data System (Lillestrand, 1972) is likewise capable of high processing rates. A current base system can process up to 400,000 6-bit bytes per second (with expanded capabilities available) including geometric rectification and classification.

Anuta and Bauer (1973) used four band digital ERTS-1 data in agricultural and urban change detection with mixed success. Using reflected difference data (.5μ to 1.1μ) they obtained a 68% classification accuracy using corn as the agricultural test crop. In their urban experiment they had a high "false alarm" rate (where construction existed). In addition to this they found that rainfall previous to the time the data was scanned adversely affected classification accuracy

and suggested using data obtained in periods of mean (temporal) rainfall. Kawamura (1971) utilized digitized aerial photographs to analyze urban changes. The digitized data was geometrically registered and processed with algorithms selected to find (in part) high reflectance areas (correlated with man-made constructions). Training cells were selected and used to classify the test set for various types of urban changes.

Pohn, et al. (1974) used digital Nimbus IV thermal IR data to investigate thermal inertia effects in rock units of Oman. One pair of day/night data sets (obtained eight days apart) were geometrically registered and straight differenced; where the night set was subtracted from the day set at "all points where contours on the two maps intersected". They used temperature differences since this minimized the effects of emissivity and elevation differences, as ΔT is dependent primarily on thermal inertia and to a lesser extent on reflectivity. (Assuming other factors constant: as the thermal inertia decreases, ΔT increases; and as short wavelength reflectivity decreases, ΔT increases.) They stated that the ΔT map showed more detail and had a stronger correlation with a modified geologic map than did individual reflectivity or temperature maps.

Additional factors to those already presented may govern the application and utilization of change detection to solving specific problems. (Several points in this discussion were also raised by Rosenfeld (1961)). In some cases it may be adequate to know that a particular type of change has occurred at a given region as a function of time. Here crosscorrelation can often be utilized to determine the degree of similarity between the two subscenes, and from this infer the degree of

change. In other cases, however, differencing is preferable since it may be necessary to determine the location, magnitude and sign of the change. Differencing will also reveal whether the changes that have occurred are minor and widespread or local and significant. A disadvantage of differencing is its sensitivity to scanner noise on an individual point basis and criteria such as (in this case) classification of temperature differences is often needed to distinguish between significant changes and irrelevant ones. Hence an optimal combination for change detection analyses is often the use of both crosscorrelation and differencing.

Given a fixed spectral and spatial data format (i.e., wavelength region and resolution) certain types of changes can be monitored while others cannot. With the relatively large fixed pixel size used here (.91 km at nadir), man-made changes are generally overshadowed. Diurnal, seasonal, and environmental changes, however, will tend to affect much larger regions and may have a noticeable effect on the data. A portion of the observed seasonal changes, i.e., due to differences in the sun's declination can possibly be eliminated by using mean-biased analyses; thus allowing the investigation of other factors on the thermal signature of the site.

The size of a given change is also a significant factor. Obviously due to physical factors that introduce non-linear location errors into the data (i.e., curvature, scan angle and attitude errors) registration between temporal data sets is not exact. Hence a minimum cell size must be determined and utilized in analyzing data processed by change detection. In addition to this, one must decide whether observed changes of a particular type are local or global in

nature. If a significant local change occurs only in one region, an upper limit as to the area it occupies is available. If many local cells or regions show this same type of change it is possible that they may have been due to a single cause (i.e., in the upper limit they may produce a uniform mean-biased difference between two data sets). Hence the type of change detected, as well as the location and size of the regions it is associated with can often provide significant information to the user.

Because of this a careful analysis should be made of the type and context of the changes observed. Concepts such as a change of acutance or boundary gradient, change of size and shape, change of textural properties, context of change among changes and context of change among unchanged areas should all be examined (Rosenfeld, 1961).

Crosscorrelation and Differencing Analysis

A crosscorrelation algorithm is often employed to determine the degree of similarity between two sets of discrete (or continuous) observations. A second (previously mentioned) use is to fine-align two images already approximately in geometric registration. There are several forms of the discrete crosscorrelation algorithm. The simplest is the unnormalized case (Bakis, et al., 1971):

$$\rho^*(\tau_i,\tau_j) = \sum_{j=1}^{\ell} \sum_{i=1}^{m} t_{i,j} r_{i+\tau_i,j+\tau_j} \quad , \tag{2.18}$$

where t and r are the test and reference pattern "vectors" respectively, and the estimation of translation (τ_i,τ_j) between the two vectors occurs at the maximum value (peak) of $\rho^*(\tau_i,\tau_j)$. In this work multiple

test "vectors" are single subscripted as $t_1 \ldots t_n$, while double subscripted reference or test "vectors" (i.e., $r_{i,j}$ or $t_{i,j}$) always refer to "vector" elements. For small ℓ and m, ρ^* does not necessarily have a global maximum at the true registration position; this is caused by the finite value of ℓ and m permitting fluctuations to dominate the function.

If the correlation function is normalized and compensated for the pyramid effect, one obtains:

$$\rho(\tau_i,\tau_j) = \frac{\sum_{j=1}^{\ell}\sum_{i=1}^{m}(t_{i,j} - \bar{t})(r_{B,C} - \bar{r})}{(\ell - |\tau_j|)(m - |\tau_i|)\sigma_r\sigma_t}, \qquad (2.19)$$

where for $\tau_i < 0$, $B = |\tau_i| + i$; for $\tau_i \geq 0$, $B = i - \tau_i$;

$\tau_j < 0$, $C = |\tau_j| + j$; for $\tau_j \geq 0$, $C = j - \tau_j$;

$\bar{r}$ and $\bar{t}$ are the means of the reference and test vectors; and

σ_r and σ_t are the standard deviations of the reference and test vectors.

The factor $(\ell - |\tau_j|)(m - |\tau_i|)$ compensates for the decreased size of the overlapping set as τ_i and τ_j approach their maximum values. Otherwise, a pyramid shaped surface would appear, with the peak at the center (highest magnitude) and these maximum shift locations at the other vertices. A minor scale error exists if the unbiased estimates of σ_r and σ_t are used in eq. 2.19.

In the simplest (unnormalized) case, if the test pattern is given by the matrix [t] = [r] + [n], where the difference between the reference and test patterns is due to a noise component [n], then eq. 2.18 becomes:

$$\rho^*_{r,t}(\tau_i,\tau_j) = \sum_{j=1}^{\ell}\sum_{i=1}^{m}(t_{i,j})(r_{i+\tau_i,j+\tau_j}) \quad , \tag{2.20}$$

which for maximum correlation ($\tau_i = 0$, $\tau_j = 0$) becomes:

$$\rho^*_{r,t}(0,0) = \sum_{j=1}^{\ell}\sum_{i=1}^{m}[r^2_{i,j} + r_{i,j}n_{i,j}] \quad . \tag{2.21}$$

The "noise" component, $n_{i,j}$, are not in general independent of $r_{i,j}$, and may contribute a positive or negative increment to $\rho^*_{r,t}(\ )$. Here when $n_{i,j} = 0$, we have the familiar autocorrelation case.

A second class of algorithms for detecting similarities between two vectors (patterns) includes the Mean Absolute Difference (MAD) and differencing techniques. The MAD algorithm is given by:

$$\text{MAD} = \sum_{j=1}^{\ell}\sum_{i=1}^{m}|r_{i+\tau_i,j+\tau_j} - t_{i,j}| \quad , \tag{2.22}$$

$$= \sum_{j=1}^{\ell}\sum_{i=1}^{m}\sqrt{t^2_{i,j} - 2t_{i,j}r_{i+\tau_i,j+\tau_j} - r^2_{i+\tau_i,j+\tau_j}} \quad . \tag{2.23}$$

When the MAD minimum occurs at $\tau_i = \tau_j = 0$, assuming [t] = [r] + [n] we have:

$$\text{MAD} = \sum_{j=1}^{\ell}\sum_{i=1}^{m}|n_{i,j}| \quad , \tag{2.24}$$

and when in addition $n_{i,j} = 0.0$ we have:

$$\text{MAD} = \sum_{j=1}^{\ell}\sum_{i=1}^{m}(0.0) \quad . \tag{2.25}$$

A second observation that can be made from this technique is when $n_{i,j} = 0.0$, eq. 2.23 reduces to:

$$\text{MAD} = \sum_{j=1}^{\ell}\sum_{i=1}^{m}(r_{i+\tau_i,j+\tau_j} - r_{i,j}) \quad . \tag{2.26}$$

In the MAD algorithm (eq. 2.23) the terms that contribute a maximum of $\rho^{*}_{r,t}(\ )$ (eq. 2.21) are subtracted under each radical. In addition, $t^{2}_{i,j}$ contains a noise component which will generally be positive, but occasionally may have a negative effect. It should be noted that in the MAD algorithm (eq. 2.23) the $t_{i,j}$ and $r_{i,j}$ components are assumed identical except for a noise ($n_{i,j}$) component and possibly the assignment of i and j. The presence of noise in either the MAD or correlation cases degrades the ability of the algorithm to select a proper minimum or maximum.

In the MAD algorithms the sign of the resulting difference between test and reference cases is lost. In change detection it is often necessary to differentiate between an increase or decrease in an object's spectral property (i.e., reflectance or (energy) temperature) with time as well as knowing that a change has occurred. Often the change must be determined on a point-by-point basis in attempt to identify the region in which the change occurred, or the specific cause or result of this change. Since in this work there was an interest in identifying terrain features whose associated temperatures were time-invariant or else deviated significantly from the "average-change", all difference processing was performed on a point-by-point basis. Consequently all differencing formulas utilized were developed for a point-by-point and not an overall (double summation) analysis. In some cases crosscorrelation was used to determine the overall degree of similarity and the local registration error between two geometrically transformed images of the same subscene.

A modified form of eq. 2.22 implemented for point-by-point straight differencing which also preserves the sign of the change is:

$$SD_{i,j;\tau_i,\tau_j} = (r_{i+\tau_i,j+\tau_j} - t_{i,j}) \quad , \tag{2.27}$$

and assuming the vectors are in registration we have:

$$SD_{i,j} = (r_{i,j} - t_{i,j}) \quad . \tag{2.28}$$

Here again, if [t] = [r] + [n], the images are in registration and if [n] is zero, we find:

$$SD_{i,j} = 0.0 \quad . \tag{2.29}$$

In addition to this, if [n] is everywhere the difference in vector means between [r] and [t] then we have the mean-biased difference case:

$$MBD_{i,j;\tau_i,\tau_j} = (r_{i+\tau_i,\, j+\tau_j} - r_{i,j} - \bar{r} + \bar{t}) \quad . \tag{2.30}$$

Since the noise component [n] may not simply be the difference in means between [r] and [t], the general form of eq. 2.30 for data sets in registration is:

$$MBD_{i,j} = [(r_{i,j} - \bar{r}) - (t_{i,j} - \bar{t}] \quad , \tag{2.31}$$

$$= [(r_{i,j} + (\bar{t} - \bar{r})) - t_{i,j}] \quad . \tag{2.32}$$

If the relationship between [r] and [n] is not known, the form used (assuming registration between [r] and [t]) is given by eq. 2.32. Specifically, eqs. 2.28 and 2.32 were utilized in straight and mean-biased difference point-by-point processing done in this work. The result of this is straight and mean-biased difference temperatures for every data point. This is performed for computational convenience in analyzing the resulting output. In reality the only variation between these two values at any point is related to the difference in data set

means since otherwise, the distributions are identical. In the straight difference case the distribution mean lies at $(\overline{r} - \overline{t})$, where in the mean-biased case it has been compensated for and lies at zero. Thus, the straight-difference algorithm subtracts each point without compensation, whereas the mean-biased difference algorithm removes the difference in data set means before subtraction.

In the differencing analysis used here, the resulting distribution of points contains three regions of interest. The first is centered near zero ΔT, and is indicative of the number of temperature invariant points present between the two data sets. These points can be of interest for position fixing purposes as previously discussed. The next region of interest in the resulting distribution lies near the difference of the data set means $(\overline{r} - \overline{t})$. This "average-change" or average ΔT portion can also be used for position fixing if the point-by-point difference between data sets is primarily related to the mean temperatures of these scenes. (This assumes that the standard deviations of the data sets are not widely different.)

The third portion of the distribution that is of interest is the highest (±) change or highest ΔT region. If the standard deviations between the data sets are similar, then a significant population of points in this region (or at the opposite side of the distribution) can cause a reduced correlation by increasing the variance of the difference distribution. (If the difference between data set means $(\overline{r} - \overline{t})$ is large, then those points near zero ΔT will also be far from the average ΔT, and will similarly increase the variance of the difference distribution.) If the population of this portion of the distribution varies between difference sets (i.e., the size and location of the

anomalous regions are time dependent), then little can be done in compensation. If, however, the population of this region is invariant among difference distributions that utilized the same reference pattern, then the reference pattern itself may be thermally anomalous, and a higher degree of correlation may exist between test sets. Using a "thermally-unrepresentative" reference pattern should decrease the resulting correlation between it and other data sets. There is no guarantee, however, that choosing a more representative reference pattern will increase the resulting correlation, even though that is expected.

A two dimensional (spatial) output plot of individual point intensities in each of the two cases will reveal which areas produce changes of the greatest value, and locate the terrain features to which these regions correspond. In addition to this, boundaries between regions of significant change will be readily observed. In fact for homogeneous areas if an anomalous temperature change occurs most of the region in general will be affected. This will reveal the thermal boundary between the area of anomalous change and the surrounding region and aid in identifying the terrain feature that this area represents.

CHAPTER III

INSTRUMENTATION

Data Parameters

In order to generate statistics of the thermal IR signatures as a function of time of day, season of year, and environmental conditions, it is necessary that the same location be imaged on a number of representative occasions. Though ideally a large number of data sets would be obtained of the test site for each of these categories, practical considerations limit the actual number that can be analyzed. These limitations include the overall computer budget allocated for the work, the large amount of analyst time needed in several aspects of the data processing, occasional delays in obtaining scanner data due to satellite and environmental factors, and potential scanner reliability problems. It is clear, however, that diurnal or seasonal information extrapolated from a data bank containing information primarily gathered at one time of day or in close succession could contain significant errors.

Data generated from multiple day/night pairs of passive microwave data was not available for this investigation. The only repetitive passive microwave data of this type, to the author's knowledge, was generated by the Electronically Scanning Microwave Radiometer (ESMR) flown aboard the Nimbus V and VI satellites. It was felt, however, that because of inherently low resolution (25 kilometer-square pixels

at nadir, degrading to 160 km cross-track by 45 km along-track at the edges of the scan width) and a small number of scan positions (78 per line), the data might not have been sufficient for use in this analysis. A search of existing NASA thermal IR missions also proved negative for repetitively scanned day/night data of a given test site (Pitts, 1975). After approximately ten months, contact was made with the Environmental Products Group, National Environmental Satellite Service, National Oceanic and Atmospheric Administration (NOAA), who agreed to provide digital and photographic thermal IR data from the very high resolution radiometer (vhrr) aboard the NOAA-4 satellite. In June, 1975 the first data was obtained and analyzed at OSU. It was determined that the data was too noisy (due to synchronous and non-synchronous electromagnetic pickup interference, and random noise) to be useful. In fact, the data typically had an RMS noise of between one and three counts in the eight bit-byte dataword (Koffler, 1975). Since a goal of this work was to investigate whether or not constant or mean-biased temperature invariants existed within the test site, the substantial noise present in this data was judged to render it unuseable.

Such noise present in the data can influence the proposed differencing analysis in two major ways; the first is a salt-and-pepper effect due to random noise which tends to obscure terrain boundaries and potential g.c.p.'s. In this work potential g.c.p.'s were often contained within terrain boundaries; which typically had gradients of between two and four counts. Consequently, noticeable errors in geometric registration could occur if potential g.c.p.'s were determined from noisy data (such as NOAA-4 vhrr). In fact, it can be shown that when overlay quality between images is affected solely by additive noise

(which is also signal-independent) the standard deviation of the registration error is inversely proportional to the square root of the SNR; specifically (McGillem and Swedlow, 1976):

$$\sigma_i = \frac{\Delta z}{\pi} \sqrt{\frac{3}{SNR}} \quad , \tag{3.1}$$

where Δz = equivalent ground track sampling interval (ifov in X or Y). Secondly, if the noise (random or systemic) is signal independent (statistically independent of the terrain signal), it can decrease the overall correlation between the reference and test data sets.

Because of this inherent noise problem, additional data was sought and special authorization to transmit and obtain data from another scanner system, NOAA-3 was granted for this work. The NOAA-3 satellite was in utilization as a backup system to NOAA-4, and had an expected expiration time of November, 1974. Each NOAA Improved Tiros Operational Satellite has a design lifetime of six months and a goal lifetime of one year (NOAA-1, 1972, p. 7). Due to fortunate circumstances, however, this scanner was still operational through February, 1976, and for vhrr thermal IR data produced a noise level considered to be the lowest of any existing ITOS system (Breaker, 1975).

The instantaneous field of view (ifov) of each vhrr scanner in the ITOS series was a fixed design parameter. With the vhrr thermal IR scanner this was .60 milliradians, which equates on the ground to approximately .91 km at nadir, degrading to $\sim$1.53 km at the subsynch lines. (The subsynch lines represent the useful limit of cross-track scan due to (rapidly) non-linearly increasing geometric distortion.) Since the platform altitude was nearly constant from orbit to orbit and

the ifov was a fixed parameter, pixel area as a function of scan angle (α) was constant between orbits. The pixel area, however, increases with angle from nadir non-linearly because of scan angle effects and the earth's curvature, since the differential scan angle $d\alpha$ per pixel remains constant, independent of α.

Clarification is given here between $d\alpha$ and the ifov; both are fixed parameters of the scanner system. The ifov (.60mr) corresponds to the equivalent ground area that is viewed by the scanner and recorded in the data as a pixel; whereas $d\alpha$ (.3927 mr) is related to the ground separation distance between adjacent cross-track pixels (Legeckis, 1976). At nadir (where $\alpha = 0.0$) the NOAA-3 vhrr cross-track ifov and $d\alpha$ correspond to a ground distance of .91 km and .59 km respectively, and the separation between adjacent scan lines is .88 km. Hence in this data we have the representation shown in Figure 1. From Figure 1 there is an overlap between pixels which corresponds to the difference of the ground-distance equivalents between the ifov and $d\alpha$. The ratio between the ground distances of these parameters is fixed, but the actual magnitudes vary non-linearly with α due to the earth's curvature and scan angle effects.

Given the fixed nadir pixel size of the NOAA-3 vhrr thermal IR data different types of recognizable terrain features were considered. In the first case where the terrain feature was large in area compared to the pixel size, relative shape and magnitude was preserved except for small discontinuities due to discrete sampling at the boundaries. This effect was frequently observed along large water, land, and mountain-desert boundaries in data used for this work. In the second case, as the area of the terrain features decreased to that of a few

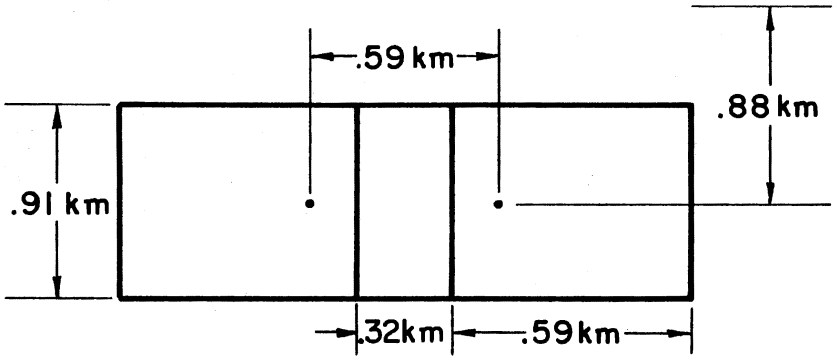

Figure 1. Ground Representation Between Two Consecutive NOAA-3 Vhrr Pixels at Nadir

pixels, boundary discontinuities became more obvious due to the reduced area/perimeter ratio. This effect was noticed while investigating small towns for use as potential g.c.p.'s in registration of the untransformed data.

Finally when a target had an area less than one pixel neither shape nor magnitude was preserved. This was generally expected in cases where small heterogeneous regions existed within a pixel area, such as in man-made developments or geological anomolies. Still a single object thermally dissimilar from its background can possibly be detected.

If the target within a pixel has an area and temperature magnitude large enough, then it can effectively be seen against the cooler background region. Since the signal within the ifov is integrated to produce the observed magnitude for that pixel, the contained target must have a sufficient temperature and area to be detected. If the minimum statistically detectable temperature differential is a fixed parameter for the scanner at a given temperature, then the corresponding minimum target area can be computed. Likewise, if a target of known area is contained within a pixel, then the minimum temperature differential for detection between the object and its background can be found. The relationship between target, background, and detection temperatures and pixel and object area is given by (NASA-JPL, 1975):

$$A\sigma\varepsilon_{se}T_{se}^4 = a_p\sigma\varepsilon_H T_H^4 + (A - a_p)\sigma\varepsilon_{av}T_{av}^4 \quad , \qquad (3.2)$$

where A = pixel area,

a_p = smaller ground area, $a_p < A$,

T_H = hotter temperature of area a_p,

T_{se} = sensed temperature,

T_{av} = average temperature of the remainder of pixel,

ε_{se}, ε_{H}, ε_{av} are the emissivities of the respective temperature regions, and

σ = Stefen-Boltzman constant.

One might argue that small ifov's are desirable for performing an analysis of this type; both from the viewpoint of increased available g.c.p.'s for registration, and the potential for investigating "no-change" regions in man-made facilities. However, solely decreasing the ifov while maintaining other scan and satellite parameters poses several problems. Reducing the ifov to that of Landsat size (.086 mr) in this case would drastically increase the number of points per scan line, assuming the NOAA-3 altitude of ∿1508 km is maintained. Specifically the original number of data points in the test site in this case would increase by $[\frac{\text{ifov NOAA}}{\text{ifov Landsat}}]^2$ or approximately 133. This would increase the total points within the test site from 107,920 to over 14.5 million. From this a significant data management/processing problem would develop unless the test site area was decreased substantially.

The amount of data generated by the vhrr thermal IR sensors is 106,666 samples/second (S), at 6,667 rotations/second (W) of the scan mirror (Legeckis and Pritchaird, 1976, p. 2). Current real-time image correlators are capable of 400,000 pixel/second processing rates (6 bit-byte) (Lillestrand, 1972). If the vhrr thermal IR scanner was used in such a real-time correlation system with a halved ifov (.3 mr) this upper limit figure would be met. Reduction in the ifov, however, affects several other parameters besides data rate; specifically increasing scanner weight, and altering the optical design (Mundie, et al.,

1975). These trade-offs must be weighed against any expected gains of even a two-fold increase in resolution. To approach an increase in resolution of five to ten times would require a complete redesign of the system with much added complexity, or a platform at much lower altitude, which would likely decrease the overall field of view.

The results in this work are bounded in a two-fold manner. First, the analysis of thermal signatures was only carried out over a small region and global extrapolation of results should only be done cautiously. Secondly, the ifov and hence the nadir pixel area of the data were fixed parameters in this work. Clearly, the type of terrain features observed as individual pixels in the data is dependent upon the ifov for a fixed scanner altitude.

NOAA-3 Vhrr Thermal IR Scanning System

The ITOS satellite first launched in October, 1972, forms the basis of current NOAA environmental research observation platforms. The primary sensor systems each satellite contains are a two-channel (visible and thermal IR) scanning radiometer (ifov = 5.3 mr), a vertical temperature profile radiometer utilized to obtain measurements of the vertical temperature structure of the atmosphere, a vhrr scanner similar to the scanning radiometer but with an ifov = .60 mr, and a solar proton monitor. The mean altitude for NOAA-3 is $\sim$1508 km while for other ITOS satellites it is $\sim$1464 km. The angle of inclination is 101.7^{o} and nodal period is 116.20 minutes for NOAA-3 which processes a sun-synchronous orbit (Daghir, 1976).

Each sensor system on the ITOS satellites is duplicated to provide backup in case the primary sensor fails. A representation of the

external configuration for the various sensor systems is presented in Figure 2. In some sensors, such as the vhrr, ordinary operation utilizes both units. Here the visible data is scanned using the visible channel of one radiometer, while the thermal IR data is scanned 180^{o} later with the thermal IR channel of the second radiometer. While radiometer one is viewing the earth, radiometer two is looking upward at its housing. By proper electronic switching it is possible to transmit first the IR channel from one radiometer, then one-half mirror rotation later the visible data from the second radiometer. (This will lead to about a 5 km spatial offset between the two spectral data forms.) In the event of the loss of a single radiometer, data from a single channel from the other system can be obtained, or at a greater loss of SNR, data from both channels can be obtained, frequency multiplexed and transmitted.

In addition, when potential transmission interference with other satellites is possible, or when the distance to the nearest ground receiving station is too large, data is often recorded on the spacecraft recording system instead of using direct real-time transmission. Time-sharing (visible and thermal IR data) from two radiometers is generally used in conjunction with the recorder. Unfortunately, the recording system is responsible for the largest single degradation of the SNR in normal operation, and this fact must be weighed against any expected advantage from using a test site located too far from a ground station for adequate real-time data transmission.

In this work direct real-time transmission of thermal IR data from vhrr scanner number one (serial number 106) was used exclusively for all seven edits due to failure of the second vhrr unit and the

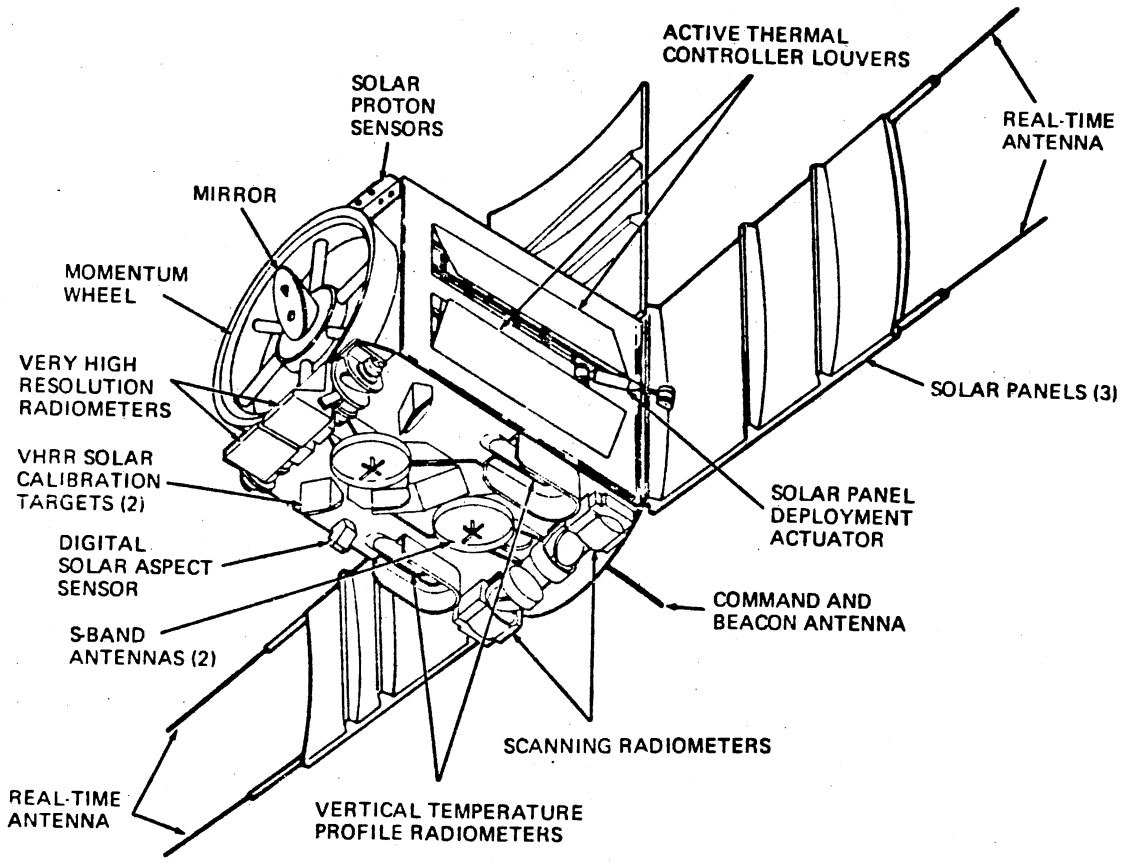

Source: National Oceanic and Atmospheric Administration (Schwalb, A.). Modified Version of the Improved TIROS Operational Satellite (ITOS D-G). NOAA Technical Memorandum, NESS-35. Washington, D. C.: NOAA-NESS, 1972, p. 6.

Figure 2. External Features of Modified ITOS Spacecraft

capabilities of direct real-time transmission to the San Francisco Satellite Field Service Station (SFSS) without the need for on-board data recording. Data from the vhrr sensors is transmitted in analog form in the microwave s-band (17.67 cm) and converted to 8 bit-byte digital form at the ground station. The very high resolution radiometer (vhrr) is described by Schwalb (NOAA-1, 1972) as:

> A two-channel scanning instrument sensitive to energy in the visible spectrum 0.6 to 0.7 μm and the infrared (IR) window 10.5 to 12.5 μm. As in the Scanning Radiometer (SR), energy is gathered by a 12.7-cm (5-inch) eliptical scan mirror with a plane surface area of 100.4 cm^2 (15.6 $in.^2$) and a telescope. The scan mirror is set at an angle of 45^o to the scan axis and rotates at 400 rpm. A Dall-Kirkham optical system focuses the incoming radiation at a point behind the primary mirror; the visible energy is detected by a silicon photo diode detector located at this focal point.
>
> A dichroic beam splitter reflects the IR radiation which comes to a focus in the plane of a field stop which, together with the detector size defines the channel field-of-view. Relay optics are used to re-image the IR radiation on a mercury-cadmium-telluride (H_gCdTe) detector. Bandpass filters in both channels define the spectral characteristics of each.
>
> The infrared detector is cooled to its operating range (near 105^oK) (-270^oF) (-168^oC) by a radiant cooler. A relatively large cooling patch provides the cooling capacity to bring the detector below the temperature 105^oK (-270^oF) (-168^oC) which provides desired signal-to-noise ratio (pp. 24-25).

Also included in the vhrr system is a set of internal calibration devices for both visible and thermal IR channels. In the thermal IR section, a set of electronically controlled voltage wedges are provided to aid in data calibration. An IR blackbody calibration target is provided to compensate for the spectral dependence (between 10.5μ and 12.5 μ) of the detector response. Three thermistors are used to determine the effective temperature of the calibration target, and a portion of the scan which views space (space view average) is used to determine

the effective temperature of the instrument noise. Since this information is provided for each rotation of the scan mirror (i.e., each line of earth data) accurate calibration of the data is possible. Thermal IR data can thus be converted from energy to equivalent blackbody surface (ground) temperatures using this information and compensating for atmospheric attenuation.

Typical noise equivalent differential temperature (NEΔT) values (the minimum temperature that can be differentiated between two adjacent blackbodies; which is related to the noise/signal ratio of the system) for the vhrr scanner in various types of data gathering modes have been determined (NOAA-1, 1972).

Quoting the NESS-35 manual,

> The infrared channel output can be used to determine the equivalent black-body temperature of the radiating surface. The NEΔT as measured at the instrument output is estimated to be 0.5°C (0.9°F) for a 300°K (80.6°F) (27°C) scene and 2.0°C (3.6°F) for a 185°K scene. These values will be degraded by the transmission, receiving, and data processing equipment. In the normal time-sharing mode of operation at a local station the NEΔT for a 300°K scene is expected to be approximately 1½° to 2°C, for a 185°K scene, 6°C to 8°C. In the backup mode of operation, in which data from both channels are frequency multiplexed, the NEΔT will be degraded to 4° to 5°C for a 300°K scene and 20° to 25°C for a 185°K scene. When tape recorded and analyzed centrally, the NEΔT is expected to be degraded somewhat over that received directly without recording. For a 300°K scene NEΔT is estimated to be 2° to 3°C; for a 185°K scene, 12° to 15°C (p. 31).

The typical NEΔT's observed from vhrr thermal IR NOAA-3 terrain data were much less than these predicted values. In fact, in all data sets used here the computed NEΔT (assuming mean zero noise) was $\leq$ .5°C, and in some cases about half of this value. Additional discussion of the sensor system is beyond the scope of this paper, and the reader should refer to Schwalb (NOAA-1, 1972, pp. 24-31) for further information.

Test Site

A test site utilized in this type of analysis should include as many different terrain and land use types as possible; yet the imaged data should contain a significant number of points for each type so the resulting analyses are statistically valid. Results from a site composed of a homogeneous material would probably lead to significant errors if applied to other terrain types. (For example, conclusions obtained from an agricultural region might be dissimilar from those of a mountainous area.) Ideally then, many different terrain types should be present within the test site.

The location of the test site used in this work was limited by the necessity of direct transmission from the satellite to the San Francisco SFSS. Because of this factor and since the site had to be kept within the 65.2^{o} field of view between the scanner subsynch lines, potential site locations were limited to California, Arizona and Nevada. In addition, the cross-track spacing error in the data (which cannot be removed by a linear transformation) increases non-linearly with the scan angle, α, along a scan line. This is of consequence since in six of the seven data sets either the east or west edge of the potential site location was close to a subsynch line; thus fixing the area that could be processed without excessive pixel spacing error.

Cloud cover over the test site was another factor that had to be weighed in chosing the actual location. Deerwester, et al. (NASA, 1972) determined that southeastern California and southwestern Arizona had the smallest percentage of overall cloud cover for each season of any location in the continental United States. In fact, in the fall and winter this area had substantially less cloudcover than any other

region including the area to the north (Nevada) and to the east (central to eastern Arizona.)

Because of these reasons and the fact that some of the desired terrain types were not found elsewhere, the area chosen for this work was located in southeastern California and western Arizona, within $\sim 32.15^{o}N$ to $\sim 35^{o}N$, by $\sim 114^{o}W$ to $\sim 116.50^{o}W$. A 1:1,500,000 scale map representing the test site is presented in Figure 3 (Rand McNalley, 1975). (Boundaries shown are only approximate since UTM grid lines are not registered with longitude and latitude lines.) Specifically, the test site was in UTM Grid Zone 11S, markers $360_{0000}N$ to $387_{0000}N$, and $78_{0000}E$ to $54_{0000}E$. UTM line $78_{0000}E$ is the eastern-most grid line in zone 11S and was used as the eastern test site boundary. To include any area to the east of this would have required correction of the data to the 11S zone markers. Since each major UTM number represents 10,000 meters at the scale used (1:250,000), the dimensions were 270 km N→S by 240 km E→W, and thus the total area was 64,800 km^2. The major terrain types present were desert, agricultural, lake, barren mountains and wooded mountains. Urban areas were also located within the site, but because of the relatively large pixel size of the NOAA-3 data they formed a very small percentage of the total test points within a data set.

Agricultural regions were located in two main areas within the site, the first along the Colorado River, specifically in the Mohave Valley near Needles, Calif., and in the Palo Verde Valley (centered south of Blythe). The second area was in the Imperial and Coachella Valleys located south and north respectively of the Salton Sea. A large saline lake known as the Salton Sea was located near the central

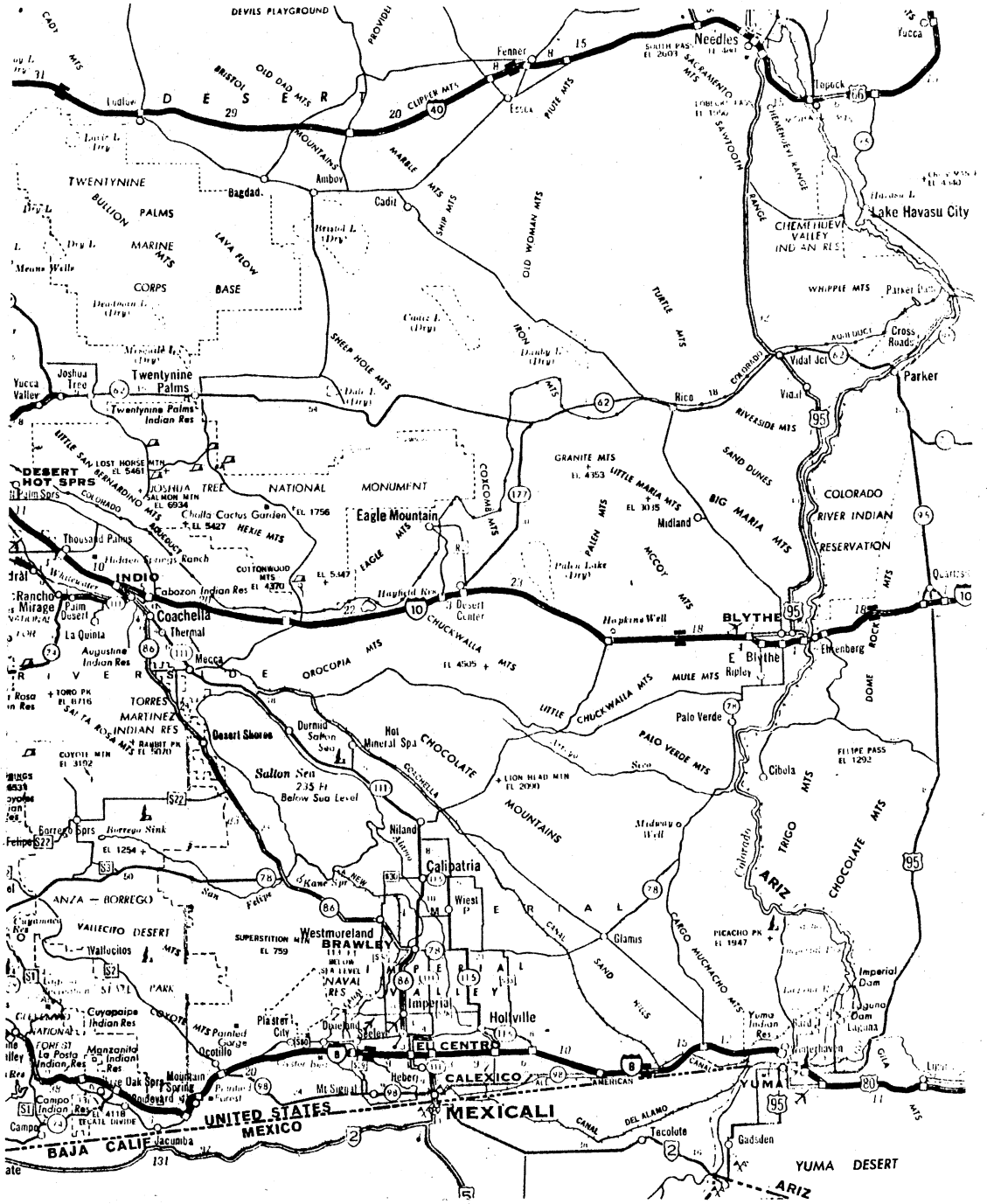

Source: Rand McNally, Rand McNally Road Atlas, New York, New York: Rand McNally and Company, 1975, p. 19.

Figure 3. Approximate Map of the Test Site

portion of the site. Its surface area fluctuates with time due to evaporation and changes of flow rates of the incoming New and Alamo Rivers. Created by a man-made accident in the early 1900's, it is one of the lowest points in the United States at ∿231 feet below sea level. The Colorado River was the sole large body of flowing water within the test site.

Urban regions within the site were primarily located in the agricultural areas previously discussed; specifically along the Colorado River and in the Imperial and Coachella Valleys. The western portion of the site was highly mountainous, with national forest regions located in the southwest and west. Mountains were also present over much of the remainder of the site. Valleys between mountains that were not agricultural were primarily desert land. Sand dunes were located in many of these valleys in the central portion of the site.

The lowest elevation in the site was located at the Salton Sea; the highest was at Toro Peak (8716'), in the Santa Rosa Mountains west of the Salton Sea.

Selection of Data Sets

After the test site location had been chosen, data collection began at the San Francisco SFSS.[1] The initial objective was to obtain three or four diurnal data pairs spaced over an approximate time of six months. The data collected for this research at the SFSS included one digital data tape and one photographic paper image per orbital pass over the test site. The photographic paper imagery was used

---

[1]Under the supervision of Mr. Larry Breaker.

preliminarily to screen the data for further use. With this imagery, verification was made that the test site was located between the subsynch lines and that cloud cover was absent over the test site during the scan. The absence of detectable cloud cover was the only environmental constraint imposed on data collection.

The initial day/night pair was obtained on 21 September, 1975 (orbits 8477 and 8483 respectively). A second day/night data set pair was obtained on 23 October, 1975 (orbits 8874 and 8880 respectively). Approximately five weeks later an attempt was made to obtain another data set pair. At this time, however, a severe brush fire was in progress in the area north and east of Los Angeles. Because of this, high concentrations of aerosol (smoke) were present in the atmosphere over the test site area. These smoke particles would have caused substantial attenuation of the thermal IR signal from the ground to the scanner, and since correction for this effect would have been difficult, data collection was postponed for approximately two weeks.

During this period of time, however, the efficiency of the satellite's daytime solar battery recharging cycle had decreased below the point of allowing night scans over the test site, even though for approximately one-half of each orbital period the satellite is in sunlight (local day). Consequently, only day scans could be collected at this time, and one was obtained on 11 December, 1975 (orbit 9481). Approximately one month later the battery recharging problem had disappeared but potential satellite transmission interferences now existed for local daytime orbits over the United States. Consequently, only nighttime edits could be generated, and one was obtained on 10 January, 1976 (orbit 9859). An additional data set was obtained from

the files of the Health Applications Group, Life Sciences Directorate, NASA-JSC. This group had been using NOAA-3 vhrr thermal IR data since 1974 in a screw worm eradication project in cooperation with the United States Department of Agriculture and NOAA. Here, direct vhrr data transmissions were collected at Houston, Texas, where the data was cataloged and processed. Since the area of interest for this work was central Mexico, only one filed data set was located that contained the test site between the subsynch lines. This data set was a daytime edit obtained on 4 June, 1974 (orbit 2590). Photographic film imagery produced from the digital data edit was obtained from NASA-JSC and photographic paper imagery which included the test site and a large area to the north was obtained from NOAA-NESS, Suitland, Maryland. Thus, seven data sets in all were obtained and screened for additional analyses. In total, digital computer-compatable tapes (CCT's) and photographic imagery were supplied to the author by NOAA (six) and NASA-JSC (one) for use in this work.

In order to obtain accurate meterological information from recording stations within the test site, exact scan times for each data set were needed. This timing information was sometimes provided on the photographic paper imagery, but was often erroneous. Exact test site crossing times were obtained from ephemeris data transmitted by NOAA-3 at the equatorial crossings of each orbit. This information consisted of the GMT equator crossing time, longitude of crossing and altitude of the spacecraft. From this information and knowledge of the spacecraft velocity the time of any latitude crossing can be computed accurately to within a few seconds. Test site crossing times were computed by the author from this ephemeris data and an orbital plotting chart at the

Spaceflight Meterology Group, NASA-JSC. Ephemeris information could not be located for orbit 2590, and the test site crossing time in this case was computed by the National Weather Service, NOAA, Suitland, Maryland.

The computed crossing time (to the nearest minute), date and equitorial satellite altitude were compiled and presented in Table I. Here the orbit date and crossing times are given in Pacific Standard Time (PST), not GMT.

TABLE I

SATELLITE ALTITUDE, SCAN DATES AND TIMES FOR DATA SETS

Orbit #	Day/Night	Mode*	Equitorial Altitude (km)	PST Local Date	PST Crossing Time
2590	Day	D_e	Not Known	4 June, 1974	10:31 am
8477	Day	D_e	1507.46	21 September, 1975	8:22 am
8483	Night	A_{sc}	1507.41	21 September, 1975	7:23 pm
8874	Day	D_e	1504.84	23 October, 1975	9:07 am
8880	Night	A_{sc}	1504.83	23 October, 1975	8:09 pm
9481	Day	D_e	1508.57	11 December, 1975	8:34 am
9859	Night	A_{sc}	1512.53	10 January, 1976	7:58 pm

*D_e = descending; A_{sc} = ascending.

Meteorological Analysis

Surface air temperature recording stations within the test site were located at Yuma (Ariz.), Blythe (Cal.), Needles (Cal.), Thermal (Cal.) and Imperial (Cal.). An additional station was located at Daggett (Cal.). Although it was 30 km west of the northwestern corner of the site it was utilized in the analyses, since the nearest recording station to the northwest corner of the test site was at Thermal, 150 km away. Hourly surface temperature observations were obtained from the Environmental Data Service (EDS), NOAA, Ashville, North Carolina.

Air temperature and elevation observations from 850 mb radiosonde barometric pressure data was available directly from Yuma at 12Z GMT and in plotted isotherm contour form at 00ZGMT and 12ZGMT. Charts were obtained from EDS, NOAA, and the Department of Meterology, University of Oklahoma, Norman, Oklahoma. In addition facsimile charts for six of the seven edits (except June, 1974) were also obtained from the University of Oklahoma.[1]

Surface observations indicated an unusual directional temperature profile over the test site at the time of the June 4, 1974, edit (orbit 2590). Here air temperatures in the northern part of the site were warmer than those in the south (also confirmed from the thermal IR scanner data). This condition, which was the reverse of the normal directional surface profile, existed as long as ten hours before the edit was scanned. No cloud cover was present at the edit time and the atmospheric gradient to 850 mb (temperature/elevation) was not inverted.

---

[1]Help in preparing this analysis was given by Mr. Richard Hodur, graduate student, Department of Meterology, University of Oklahoma.

Wind speeds were between 4 and 16 knots at the recording stations at edit time.

A ridge was aloft on September 21, 1975, over Southern California and fair skies dominated during both 8477 and 8483 edit times. This led to strong warming during the day (as evidenced by the $\sim 100^{o}F$ temperatures) and radiational cooling at night. Here daytime temperature variations over a horizontal area were primarily dependent on the short wavelength reflectivity of the ground surface. There was no cloud cover present over the test site at the time of the two edits. Recorded wind speeds ranged between 4 and 25 (gusts) knots at the edit times and only Yuma, Blythe and Needles had wind speeds > 10 knots.

A cold front had passed through the test site shortly before the October 23 edits (8874 and 8880) were imaged. This appeared to be the only active meterological period of (the edit time) conditions analyzed and cold air advection dominated the area. Since the front had already passed clear skies again predominated and no cloud cover was present over the test site in either edit case. Wind speeds at the time of the morning edit were between 15 and 20 knots, except at Daggett where a speed of six knots was recorded. At the time of the night edit, wind speeds of between three and eight knots were recorded.

The December day and January night cases were meteorologically similar to the September day and night cases respectively. High pressure aloft dominated the area resulting in light winds and temperatures directly related to surface properties. Shortly before the December day edit time fog was reported in the Imperial Valley area with a resulting visibility (for visible wavelengths) of approximately three miles. (This was believed to be related to the thermal inversion over the

site.) There was no additional cloud cover over the test site at that time (although cloud cover existed northeast of Needles outside the test site boundary). Wind conditions at the time of the December day edit were stagnant (zero to four knots) except at Dagget where a speed of 10 knots was reported. In the December day case analysis of 850 mb charts showed a strong inversion was present over the test site in the early morning which probably still existed at edit time. Clear skies and radiational cooling predominated in the January night case. No cloud cover was present over the test site and wind speeds ranged from four to eight knots at the recording stations at edit time.

CHAPTER IV

DATA PROCESSING AND EXPERIMENTAL PROCEDURES

Preliminary Processing

Since all analysis work performed here was from digitized computer compatible tapes (CCT's), the first step was to be able to read the data on the tape. The CCT format is specific for vhrr data and is given in Table II (NOAA-2, n.d.). All raw CCT data tapes are 1600 BPI, unlabeled, with unformatted records and a record length and blocksize of 5340 characters (or bytes); with all data in 8-bit byte form.

The next step, given the vhrr format, is to pick the desired area (test site) for analysis on the photographic imagery, locate this area on the CCT, reformat this area on the CCT and transfer it to another tape to allow for additional processing. To begin, it is first necessary to determine what portion of the CCT contains the test site previously located on the photographic image. When the image is oriented properly ($\sim$ north at top) the first subsynch line will be on the left side for day edits and on the right for night edits. From this and the scale of the photographic imagery, the record and pixel locations of the four vertices of the site can then be determined. In this work software dictated a maximum of 800 pixels of data across the test site (cross-track) with the exact number preferably an integer multiple ($L \leq 4$) of 200.

TABLE II

VHRR CCT FORMAT

First 10 characters--time code, ASC-II	
Character 11	Space View Average
Character 12	Space View Average Duplication
Character 13	Voltage Wedge - 0 volts
Character 14	Voltage Wedge - 1 volt
Character 15	Voltage Wedge - 2 volts
Character 16	Voltage Wedge - 3 volts
Character 17	Voltage Wedge - 4 volts
Character 18	Voltage Wedge - 5 volts
Character 19	Voltage Wedge - 6 volts
Character 20	Visible Calibration Target
Character 21	IR Calibration Target
Character 22	T1--(Thermistor in IR cal Target)
Character 23	T2--(Thermistor in IR cal Target)
Character 24	T3--(Thermistor in IR cal Target)

Source: NOAA-2, Tape Format and Temperature Conversion Information for ITOS VHRR Scanners. Suitland, Maryland: NOAA-NESS, n.d.

Finally a software program is utilized to locate the desired area on the CCT (computed from the above analysis), and to label and store the resulting array on a separate tape. The software used in this work for performing the above functions was developed and written by Dr. Ronald Oines, Research Scientist, Cities Service Company, Tulsa, Oklahoma. Entitled "UNSPEC" (by this author) it is a PL/1 program executed in PLILFCLG (as were all subsequent programs). Input besides the CCT was the desired locations of the scene pulloff; specifically the first record (line) number, first column (pixel) number, total number of records, and total number of columns. This program uses the generic PL/1 built-in 'unspec' and 'substring' functions to address and pick up the bit count (value) of characters between character location (column) boundaries in a character string (record). Additional features of this program include a level (energy or temperature)--frequency (count) histogram of the transferred test area, printout of the magnitudes of the pixels in the last line of data transferred (up to 800 columns), and the calibration data for that line.

The histogram allows a qualitative check of the data besides giving the shape of the resulting data distribution within the area transferred. (This also allows computation of the mean and standard deviation of the transferred scene.) The second feature in "UNSPEC" allows the computation of cross-track (along a scan line) statistics for the scene. (This is important since some types of systemic "noise" only occur in the along-track direction.) In addition, the calibration data provided can be used as a check on scanner operation and for converting the raw data (energy) on that scan line to equivalent blackbody surface temperatures.

The "UNSPEC" program was used twice in analyzing each data set. In the first case the desired scene (test site) was transferred from the raw CCT for data quality evaluation. From this (among other things) accurate record boundary locations of the site were determined and used to limit the region processed by the (costly) temperature conversion program given below. In the second case, it was used to transfer the atmospheric corrected temperature converted data of the scene to another tape so that an evaluation of potential g.c.p.'s used in geometric registration could be performed. A complete description of the transferred data format used in this work is given in Appendix C.

Temperature Conversion

The temperature conversion processing for all seven data sets was performed by Mr. Everett Thompson, Lockheed Electronics Company, NASA-JSC, Houston, Texas. (In some cases the author directly assisted Mr. Thompson.) The program developed by NOAA-NESS was implemented on the Passive Microwave Investigation System (PMIS) Data Analysis Station (DAS) at NASA-JSC, by Mr. Thompson. (An extended description of the utilization of the PMIS DAS is presented in NASA-JSC-1, 1971.) It was first necessary to density and format convert the raw CCT's to a product that could be read by the PMIS DAS. Specifically, the 1600 BPI vhrr tapes had to be copied down to 800 BPI to be compatable with this system. (In some cases this was performed at Oklahoma State University, in others at NASA-JSC.) It was then necessary to convert these 800 BPI vhrr format tapes to LARS-II format for compatability with the PMIS DAS software. (In each of the seven cases this conversion was

performed by Mr. Thompson.) (A description of the LARS-II format is given in NASA-JSC-2, 1975.)

The actual temperature conversion is described below. The temperature and voltage of the space view average and the IR calibration target were calculated from the internal calibration data and known sensor parameters (Kniskern, 1975). This information was used to form the range of temperature evaluation of Planck's equation. Here, Planck's equation (eq. 2.1) was evaluated between $10.5\mu \leq \lambda \leq 12.5\mu$ at integer temperatures between the two calibration points to produce a look-up-table for energy-to-temperature conversion. (This process can be extrapolated accurately to temperatures greater than the IR cal target; up to $\sim 330^{o}K$.) Hence, the energy--temperature relationship was derived once for each block of data analyzed and a look-up-table was utilized for the actual conversion step of each data record processed. Incorporated within this temperature conversion program was an atmospheric correction subprogram based on the empirical model of Koffler (1975) for ITOS-1 vhrr thermal IR data. A brief discussion of this and other atmospheric correction models is now presented.

Atmospheric Correction Models

As electromagnetic radiation passes through the atmosphere its amplitude is attenuated. If aerosol diameters and concentrations are small, then scattering at long wavelengths ($\lambda \geq$ thermal IR wavelengths) is negligible, and the primary cause of attenuation is due to molecular absorption from gasses found in the atmosphere. This absorption is pseudo-random in nature and highly wavelength dependent; thus making analytical evaluations very difficult (La Rocca, 1975). The first of

these utilizes numerical integration of the line absorption spectrum over the desired wavelength interval. An example of this line-by-line method is that of Pitts (NASA-JSC-3, 1974). The second method, known as band modelling, utilizes an artificially created line structure to compute atmospheric transmission. The accuracy of these methods can approach that of experimental measurements in some cases. Two inherent problems, however, in using them are excessive computer processing requirements and difficulty in adequately describing the atmospheric structure utilized.

One method of alleviating these problems is to use an atmospheric transmission model based upon an empirical analysis of actual sensor system and ground temperature measurements. Though reasonably simple in nature, results from models of this type are not as accurate as those from line-by-line or band models. The primary reason for this is due to the difficulty of predicting the atmospheric transmission under a variety of physical (i.e., scan angle and altitude) and meterological (i.e., concentrations of precipitable water) conditions. The accuracy of this technique can be improved by utilizing a different set of computations as a function of scan angle for each scanner platform altitude, and by gathering sensor system and ground temperature measurements under typical atmospheric conditions. Never-the-less, a major source of error with this type of model is due to the variation of the amount of precipitable water in the atmosphere. Since atmospheric attenuation increases with the amount of precipitable water present a model based upon a "dry" atmosphere would undercorrect a data set obtained through a "wet" (or humid) one.

The atmospheric model used in this work is an empirical one developed by Koffler (1975) and relates the loss (attenuation) temperature to the ground temperature scanned and the local zenith angle at a constant satellite platform altitude. Specifically, it is given by:

$$\Delta T_a = (-26.81 + .1072*T_g)(\exp^{.000012(Z)^2}) , \qquad (4.1)$$

where ΔT_a = the loss temperature through the atmosphere;

T_g = the absolute ground temperature; and

Z = the local zenith angle.

Hence, the corrected temperature T_c for the object scanned is given by

$$T_c = T_g + \Delta T_a . \qquad (4.2)$$

To calculate the local zenith angle for NOAA-3 data it is first necessary to compute the nadir angle of the object scanned. From this the local zenith angle can be determined.

The ΔT_a correction in eq. 4.1 was based upon 106 ITOS-1 scanner and ground temperature observations by Koffler; most of which were over land (Koffler, 1976). In practice ΔT_a appears to threshold out at $T_g \simeq 310^oK$; thus any ground temperature above this value is replaced by 310^oK in calculating ΔT_a by eq. 4.1, but the exact value is used in eq. 4.2 to compute T_c. From eq. 4.1 ΔT_a varies with pixel location (local zenith angle) within the data set. Due to a software error on the PMIS DAS this function could not be directly utilized. What was used instead of ΔT_a varying with Z for each pixel location was a constant value of Z determined at the center of the desired scene location. At typical values of T_g and Z for the data scenes processed, the absolute value of this approximation error was computed to be $\leq .2^oC$ for a ΔT_a

of points at the scene edge determined from Z at the center of an 800 pixel wide test area.

The software algorithms for determining ΔT_a and T_c were implemented on the PMIS DAS in conjunction with the previously discussed temperature conversion procedure as one main program. Hence, the look-up table between energy and temperature is determined as is the local zenith angle to the center of the test site. The data is then temperature converted, and T_c is computed for each data point by eq. 4.2 and output for additional processing in LARS II format at 800 BPI. (Again, for the thermal IR data used in this work, assume $T_c = T$, and $\Delta T_c = \Delta T$.)

The generated T_c values were checked by the author with manual calculations from the raw data. Though very tedious in nature, this step was necessary since no simple relationship exists between energy (raw data) and T_c for a given data set. In fact, calculations of this type by the author verified by a video analysis on the PMIS DAS by Mr. Thompson detected two erronously processed data sets that proved to have an error in T_c of $\sim 10^{o}C$. This was later found to be due to reading the visible calibration target (byte 20) instead of the IR calibration target (byte 21) during computation of the energy--temperature look-up table. In two cases bit slips (dropouts and additions) were present in the corrected temperature data that were not found in the raw data. These slips were probably due to tape/transport incompatabilities and were limited to one line (dropout) in the orbit 8477 scene and five lines (four addition, one dropout) in the orbit 8483 scene.

Film imagery from the PMIS DAS was generated on a line-to-line basis simultaneously during the T_c data processing. This imagery was

produced by a beam writing process and was available in both black and white and color. Superimposed on the black and white imagery was a 50× 50 pixel grid, which was useful in determining the approximate location of terrain boundaries that contained potential g.c.p.'s.

Statistics of Data Sets

Sensor systems are affected by several noise sources, the first being wide-band random noise from the detector and preamplifier, onboard transmitter, ground station receiver and analog-to-digital converter. Such noise affects data quality both along-track and cross-track, and manifests itself as perturbations in data magnitudes for each pixel. Hence the standard deviation computed on consecutive pixels along-track or cross-track will indicate the extent of this type of noise present in the data.

Another source of noise was due to repetitive electromagnetic pickup from other onboard apparatus (Bakis, et al., 1971). This can take on two primary visual forms, both result from a periodic interference. The effect when the interference is synchronized in phase with the horizontal scan gives a vertical striation in the data (along-track: along columns between scan lines). The second, non-synchronized, gives an oscillatory herringbone pattern (primarily along-track). Hence, with both of these types of noise the major component of variation in the data will appear along a scan line (cross-track). NOAA-3 imagery appeared to be very clean in appearance from both of these types of noise except in the January night case, where a low intensity herringbone was present.

Though not used in this work, methods are available for reducing the vertical striation and herringbone noise that can be present in scanner data. The vertical striation interference can be removed by averaging the result of neighboring along-track elements and then eliminating by subtraction. This noise can also be removed by using Hadamard Transformation, since the noise always appears along one of the two orthogonal data axis. The averaging technique is easier to implement than the transformation method but yields imagery that has a slightly greater degradation. The herringbone can also be removed by averaging, but not as effectively as in the first case, since it appears as a two dimensional pattern in the imagery. Discrete convolution or Fourier Transformation can be utilized to effectively eliminate the noise peaks with substantially less data degradation than averaging in this instance. The technique is similar to the use of Hadamard Transformation in the striation noise case. The data is first transformed to the frequency domain, then the frequency and width of the noise peak are determined. A two dimensional digital filter (such as a truncated triangular notch filter) is then utilized to remove the noise peak before inverse transformation back to the spatial distance domain (Nathan, 1968). Identifying the frequency of the noise peak and properly constructing the digital filter are two of the difficulties commonly encountered in this type of restoration.

Since calibration data words in NOAA vhrr thermal IR data are only one byte in length, no sufficient uniform calibration source is available within the satellite for computation of the RMS noise of the data. In other scanner systems, however, such as the Bendix 24 channel multispectral scanner which generates 16 bytes of calibration data/scan

line/sensor channel/calibration source (NASA-JSC-4, n. d.) accurate RMS noise determinations can be computed directly from the calibration data.

To measure the total noise (random plus systemic) present in the vhrr thermal IR data the signal from several adjacent cross-track pixels over a "uniform" source were obtained, and their means and standard deviations determined. Since no true, natural, uniform blackbody sources of sufficient size for this analysis exist on the earth, an approximation was made in the statistical analysis by using consecutive cross-track pixels corresponding to homogeneous terrain regions. Cross-track data should be utilized, since by solely using statistics computed from along-track data, systemic noise which appears as cross-track variations (vertical striations and herringbone) is rejected and only the noise which appears as along-track variations (minimal in vhrr data) and random noise is observed (NASA-JSC-5, 1971, p. 23). Since vertical striations and herringbone (in practice) can only be determined along scan lines and since horizontal striations were missing in large extent from the vhrr NOAA-3 data analyzed here, cross-track evaluation was the method used for data quality assessment.

In the data utilized in this work, the Pacific Ocean (off-shore California) and the Sonoran desert were used as quasi-uniform water and land sources. Noise determinations calculated from consecutive cross-track pixels were thus conservative in nature and a fair approximation of this parameter as terrain data contains degradations from the entire scope of the sensor and ground support systems.

Data evaluated was generated by the last line feature of the "UNSPEC" program (previously discussed). Cross-track analysis regions

were chosen in a quasi-random manner by the author. Each potential region was correlated with imagery of the data set and the appropriate topographic maps to insure that a homogeneous area was used. In no case, however, was the number of consecutive cross-track points chosen in a manner to falsely influence the resulting computations. When jumps between consecutive pixels of two or more counts occurred the appropriate imagery and maps were consulted to determine whether or not a terrain boundary was crossed. If no boundary was crossed, then this jump was probably caused by noise and the points included. Though the ideal situation would find taking strings from several non-consecutive scan lines; data taken from segments of one scan line never-the-less can provide a good estimate of the total (random plus systemic) noise present. Accurate computations over water were often difficult to formulate primarily due to the north-south thermal currents present off the California coast, and the lack of local landmarks usable in pinpointing areas for investigation.

Because of the often small number of consecutive points that were available for analysis (from 18 to 100), and the limitation of 800 total consecutive points from the last line feature of "UNSPEC", derived statistics were only an approximation of the total noise present. These statistics tended to be conservative, however, since they were generated from real data and often contained substrings that had substantially less noise. (In several cases substrings of up to 17 consecutive pixels were found with zero variance.)

The first step in the statistical analysis (after choosing the appropriate locations) is to compute the mean and NEΔT for each data string. In this analysis the mean utilized was the simple average of

cross-track elements. The NEΔT (previously defined) is a measure of the RMS noise level of the instrument at a particular scene temperature. The NEΔT can approximately be determined from a data string by the computation of the (cross-track) standard deviation. Specifically, for random variables $E[(X_R - M)^2] = \sigma^2_{std}$, and since $E(X_R^2) = MSV$ we have:

$$\sigma_{std} = MSV - M^2 , \tag{4.3}$$

or

$$\sigma_{std} = \sqrt{MSV - M^2} . \tag{4.4}$$

If the mean is identically zero then eq. 4.4 reduces to:

$$\sigma_{std} \equiv RMS , \tag{4.5}$$

i.e., the standard deviation is identical with the RMS noise present. If temperature converted thermal IR data is utilized in this type of analysis then both σ_{std} and RMS are a function of T, and since RMS(T) = NEΔT we have from eq. 4.5:

$$\sigma_{TE} \equiv NE\Delta T . \tag{4.6}$$

(This standard deviation is not to be confused with the standard deviation of the data scene. In the context used here it represents the standard deviation of a data string and is related to the noise present in the data, and not the standard deviation of the data scene level--frequency distribution.)

The standard deviation of temperature for the data strings utilized in this analysis was calculated by two different techniques. Due to data format requirements in a subsequent transformation program, only the first 200 columns of the 800 total columns of corrected temperature

data was printed out by the last line feature in "UNSPEC". Consequently, in some cases not enough consecutive pixels were available to determine representative statistics, and temperature data that had been manually converted and corrected from "last lines" (800 columns) of raw data were utilized. This conversion was performed by the author from a technique developed by NOAA (Kniskern, 1975). (Since the raw data (energy) was only used for preliminary analyses to verify data quality, reformatting was not necessary, and hence 800 columns were available.) In cases where temperature converted strings of sufficient length existed, means and standard deviations were directly computed.

A compilation of temperature equivalent data string means and standard deviations is presented in Table III. Also given in this table is the number of consecutive points utilized in each (cross-track) string analysis, whether the area was over land or water, and whether the computation was made from manually or directly converted temperature data. From the σ_{TE}'s computed from the strings analyzed the total noise present was within acceptable limits ($\leq \pm .5^{o}C$) so that the data could be utilized for additional analyses in this research.

The herringbone observed in high contrast imagery of orbit 9859 had a (cross-track) "period" of $\sim$12.5 pixels throughout the edit. Thus, the σ_{TE} evaluated in this case (Table III) included data over more than one complete (cross-track) cycle of the herringbone and was still modest in value. This herringbone pattern was believed to be intensified in the data by a drain of the satellite power source during simultaneous operation of the s-band microwave (vhrr) and vhf (scanning radiometer) transmitting systems (Koffler, 1976). Here the overall

TABLE III

CROSS-TRACK STRING STATISTICS DETERMINED FROM VHRR NOAA-3 DATA

Orbit #	Location	Mean(M)°C	σ_{TE} °C	Number of Points Analyzed	Computation Mode
2590	water	12.63	±.50	19	direct
2590	land	41.11	±.32	19	direct
8477	water	13.44	±.47	100	manual
8477	land	40.93	±.26	27	direct
8483	water	14.78	±.54	26	manual
8483	land	9.27	±.45	34	direct
8874	water	16.87	±.48	72	manual
8880	water	14.24	±.53	75	manual
8880	land	4.37	±.54	18	manual
9481	water	13.40	±.43	46	manual
9481	land	17.56	±.36	26	manual
9859	land	6.05	±.42	18	manual

signal strength for each transmitter would be reduced, thus causing a decrease in the data SNR.

It is important to realize that the value of a scanner NEΔT is also dependent on the scene temperature. Schwalb (NOAA-1, 1972) states that

> . . . when measuring warm targets, the NEΔT's will be significantly lower (better) than when measuring cold targets since the instrument response is linear with input energy and the system noise is not affected by target temperature. System noise, and therefore NEΔT, is affected by the temperature of the radiometer itself so that no single number can be used to define the system NEΔT (p. 14).

From Table III the two warmest targets (orbits 2590 and 8477 land) had the lowest NEΔT's (.32^{o}C and .26^{o}C, respectively), while colder targets generally had higher NEΔT's.

An additional type of noise was present in NOAA-3 vhrr data on an intermittent basis. It appeared in the data as a bit dropout or addition intermittently along a scan line (cross-track). This error occurred as a variation in the least significant bit (lsb) in the data analyzed; thus a variation of ± 1 count in energy or temperature was sometimes present. In addition to this, the calibration data was occasionally affected; thus producing a larger count fluctuation in the temperature converted data (if processed line-by-line instead of in blocks) than existed in the raw data (energy). Furthermore, this lsb problem only occurred infrequently. In viewing high contrast imagery of a scene it was often possible to find sub-blocks of 50 records or more that were free from this type of noise; while in another portion of the data every second or third record might be affected. The cause of this noise is unknown (Koffler, 1976), and because of its intermittent nature, it was difficult to quantify.

An analysis was performed in which cross-track and along-track statistics (mean and standard deviation) were computed along 1^{o} scan angle increments to determine if an angular as well as a track dependent noise (such as along-track striations and herringbone, and cross-track lsb variations) was present in the data. (Obviously, these types of noise are often time dependent in nature, and results obtained from an analysis performed with a single set of data should be carefully extrapolated.) The area analyzed was transferred from orbit 9481 data and contained a large region (over ½ the total field of view (32.76^{o})) located over the Pacific Ocean, west of central Baja, California. The analysis was developed by the author and programmed by Dr. Ronald Oines.

The standard deviations in the along-track case were found to be on the average ∿12% greater than those in the cross-track case, whereas mean values were similar. This could have been caused by as few as a single scan line having an intermittant lsb variation or from surface temperature gradients in the water induced by directional differences in the ocean currents present in this region. (Currents vary from north-south close to the Baja California shoreline, to northeast-southwest to the west of the shoreline.) In addition, any smoothing present in the instrumentation would reduce noise along a scan line, but not affect adjacent lines. It did not appear from this analysis that significant cross-track lsb variations were located within the transferred region, and hence this type of costly, time consuming procedure is probably not satisfactory for determining such variations. Perhaps a better technique is to use high contrast, gridded film imagery to locate the individual lines affected and obtain magnitude printouts of them to verify the lsb variation and its severity.

Geometric Registration Processing

After a statistical analysis has verified the data quality of the atmospheric corrected, temperature converted data scenes transferred by the "UNSPEC" program, it is necessary to determine g.c.p.'s for geometric transformation. One method of performing this is to locate potential g.c.p.'s on filmed imagery. The primary advantage of this method is the relative ease of approximately locating these points. The primary disadvantage lies in a difficulty to sometimes make accurate measurements of a potential g.c.p. between the old and new coordinate systems due to the limited size and scale of the imagery. Crosscorrelation is sometimes used as a fine alignment technique after transformation to minimize registration errors.

A second technique (used in this work) exists in which a more accurate initial location of a potential g.c.p. can be obtained in each coordinate system, but at a much greater time expenditure to the analyst. Here a pictorial output plot is generated of the scene (old coordinates) by a line printer. The scale of the resulting line printer plot is usually much smaller than that of available imagery. The pictorial effect is simulated by a densenometric range of preselected line printer characters that vary from a blank (light) to a set of eight multiple overstrikes (dark).

Two programs of this type were developed by Dr. Ronald Oines, based upon a corrected version of the density codes employed by Macleod (1970). In the first program, "GREY", a linear relationship exists between the number of input (≥ 1) data and output (1 to 21) density levels. In the second program "GREYEXP", an exponential (or logarithm) function is utilized to set the relationship between data input levels (≥ 1) and

output density levels (1 to 21). In either case the range of input data levels is determined from a level--frequency histogram of the data scene. Given this information and assuming the data is properly formatted, the program computes the number and densenometric values of the output levels, and assigns every point contained within the scene to one of the resulting density "classes". The result of this is a pictorial simulation, but one that appears "quantized" due to the finite number of output levels and a greater line printer spacing distance between lines than columns (usually 10 columns/inch and 6 lines/inch). Exponential grey scale plots (GREYEXP) are usually used to non-linearily stretch (exponential--small data set variance) or compress (logarithmic--large data set variance) the output density scale with regards to the input data level range. Linear grey scales are utilized when the data set contains an "adequate" variance to allow the resulting density plot to have an acceptable amount of overall contrast for viewing purposes. The primary disadvantage of the linear grey scale is a tendency to visually lose density levels in the dark portion of the plotted range. A densitometer may have a linear response with "darkness", but the eye probably does not; thus necessitating a replotting of the scene with reversed contrast (i.e., black (old) is now white (new)) if it is necessary to differentiate all the levels present. This problem is eliminated on the "light" end of the range of density levels, since for the first 13 levels (of 21 possible), two or less characters are used to produce the overstrike and the exact density level can be determined simply by recognizing the character(s) present.

The level-frequency histogram from the "UNSPEC" program provides sufficient information to determine the range of desired levels for the

grey programs. The resulting plot of the scene contains the density information of each data point, as well as a marked boundary in lines and columns along the left side and top of the output. Hence the exact line and column (pixel) location of any point within the plot can be determined and related back to the identical location in the (digital) scene since spatial continuity is preserved. The procedure for determining the constants in eqs. 2.7 thru 2.14 involves finding the X and Y and U and V locations for a series of potential g.c.p.'s. The X and Y locations are determined directly from the line and column markers of the grey scale data plot (old coordinate system).

The U and V locations for the same points are determined as follows. The first step is to choose a reference point in the UTM grid that will form a vertex of the desired transformation area in the new coordinate system. Consequently, from this point (which is the upper left-hand corner point in the day and night transformed scenes), a two-dimensional orthogonal distance in mm can be measured to any point in the map (transformed scene). To convert this measured distance to equivalent lines and columns in U and V it is only necessary to determine the horizontal and vertical line printer scale factors. For this work at the map scale used (1:250,000) these factors were .3953 line printer columns/map mm and .2370 line printer lines/map mm. Hence, the resulting measurement units used in both coordinate systems were in lines and columns (scaled to a line printer plot).

A CPS program named "TRNSFM" was developed and written by Dr. Ronald Oines for computing the constant coefficients in eqs. 2.7 thru 2.14. Here the line and column values of the potential g.c.p.'s in the old coordinate system (X and Y) and new coordinate system (U and V) are

entered in the program in sets of three (for the three term case). These points should be as far apart, and the lines connecting them as orthogonal (in X,Y) to each other (within the scene) as possible. (This allows a more accurate determination of the resulting constant coefficients by tending to minimize the effects of measurement errors.)

To initially check the validity of each potential g.c.p. the forward transformation is utilized (P(X,Y,U,V)). Hence resulting differences generated between computed and actual measured locations of these points are determined by eqs. 2.11 and 2.12 in the new coordinate system (map). The reason the forward transformation is used for verifying potential g.c.p.'s is because a greater amount of accurate terrain information is available from the continuous, topographic maps in the new coordinate system than is provided by the discrete, quantized grey scales in the old coordinate system.

Maps utilized in this process were (1:250,000) USGS Topographic Maps (USGS - 1-3, 1969; USGS-4, 1970; USGS-5-6, 1969). They are Transverse Mercator Projections of 2^{o} longitude by 1^{o} latitude, possess a UTM grid system and a 200' contour interval. The following maps were used: El Centro (NI 11-12, 1969), Needles (NI 11-6, 1969), Salton Sea (NI 11-9, 1969), San Bernardino (NI 11-5, 1969), San Diego (NI 11-11, 1970), and Santa Anna (NI 11-8, 1969). A UTM grid was superimposed on all maps except Santa Anna, where one was carefully constructed from the tick mark information contained on the margins.

Terrain locations of frequently utilized g.c.p.'s corresponded to land/water boundaries (Salton Sea, Colorado River), and small towns located in agricultural regions (Colorado River, Coachella Valley and Imperial Valley). In addition to this, mountain (rock)/desert

boundaries were often utilized in regions where water bodies or agricultural activity did not exist.

A representation of a typical g.c.p. utilized in this work is given in Figure 4. Here a grey scale of the September day scene centered on the Colorado River near Lake Havasu City, Arizona is presented with the pixel circled (A) used as a g.c.p. The peninsula represented is $\sim 7^{o}C$ warmer and $\sim 4^{o}C$ colder respectively than the adjacent water and land, and the location utilized as a g.c.p. lies between Site Six (boat landing on water) and Lake Havasu City (inland). Features such as this with identifiable thermal contours (boundaries) were often utilized as g.c.p.'s because of their correspondence to known (topographical) locations with good ground control.

Because non-linear local errors in the data (X,Y) exist, a large number of potential g.c.p.'s were usually determined and entered in "TRNSFM". Potential g.c.p.'s found to have a large discrepancy between computed (determined with the mean of the constant coefficients, as in eqs. 2.11 and 2.12) and measured (map) locations in the new coordinate system were dropped from further usage, while those containing smaller discrepancies were accurately remeasured in an attempt to reduce the magnitude of this variation.

After a suitable number of accurately located g.c.p.'s were found, a set of reverse transformation coefficients (c_0, ... c_2, d_0, ... d_2) was generated by "TRNSFM" (i.e., eqs. 2.9 and 2.10 were solved with g.c.p.'s entered as P(U,V,X,Y)). After these constants were determined, the simple mean of each group of coefficients was computed ($\bar{c}_0$, ... $\bar{c}_2$, $\bar{d}_0$, ... $\bar{d}_2$); as in example:

$$\bar{c}_0 = ({}^1c_0 + {}^2c_0 + \ldots {}^Jc_0)/J \quad , \tag{4.7}$$

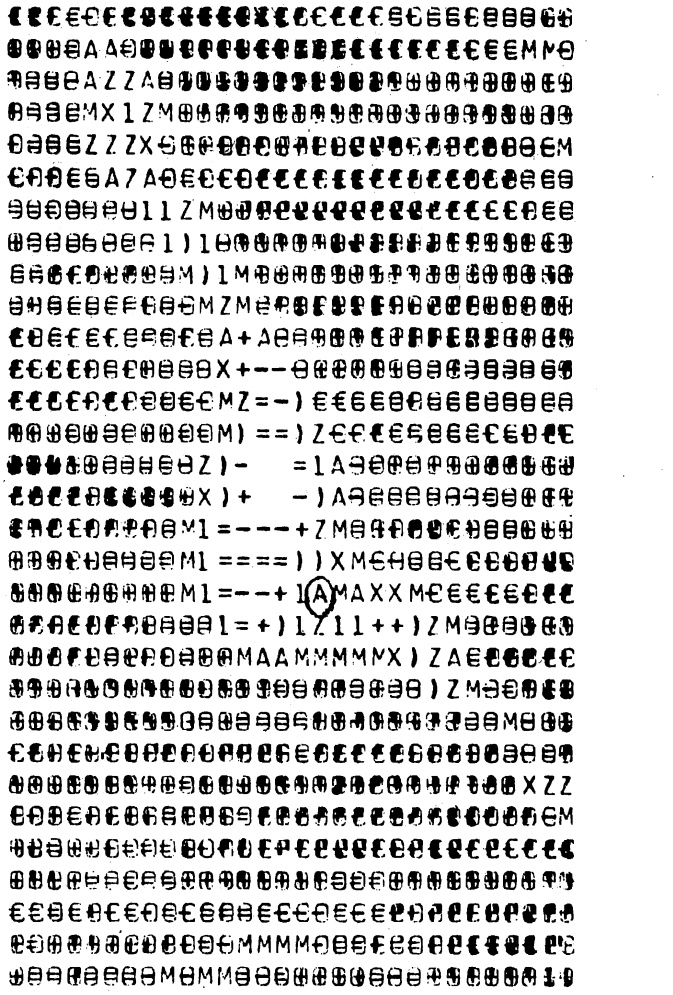

Figure 4. Grey Scale Representation of a Typical Ground Control Point Used in Registration. Plot is From the September Day Scene. A Thermal Contrast of ∿7°C and ∿4°C Respectively Exists Between the Point Utilized (Circled A) and the Adjacent Water and Land Mass

where J = the number of three term (K) sets of g.c.p.'s entered into "TRNSFM". These reverse-transformed mean coefficients were then utilized to determine the location in X and Y (old coordinates) that corresponded to integer line and column locations in U and V. Specifically, eqs. 2.13 and 2.14 were used, but here we were only interested in the computed (X,Y) locations from a given (U,V) since it was this information that was used in the transformation procedure. (The computed locations in X and Y were generally not integers.) The temperature associated with the desired (X,Y) to (U,V) location was determined from the bilinear interpolation algorithm previously given (eq. 2.16). These magnitudes were stored as floating point variables (since they often were non-integers) and placed in the proper location of the U, V (array or) transformed scene.

Two programs, named "NOAATR" and "NIGHT", were developed and written by Dr. Ronald Oines to implement the registration procedure presented above. Since the location of the first (1,1) point in the X,Y array was different for day scenes (upper left-hand corner) than night scenes (lower right-hand corner) separate programs were used to transform the data ("NOAATR" and "NIGHT" respectively). In either case, the first point in the transformed scene output was placed in the upper left-hand corner of the resulting U,V array to correspond to the proper UTM grid positioning. The programs proceed until magnitudes (temperatures) have been determined for all U, V locations within the specified bounds of the transformed data scene (i.e., U_1, ..., U_i, V_1, ..., V_j). The resulting transformed scene is formatted and stored on digital tape.

To verify the correct operation of the transformation program the transformed data set (stored on tape) is then grey-scaled. This allows

the investigation of two potential problems that can affect the registration procedure. The first is related to utilizing incorrect mean coefficients ($\overline{c}_0$, ... $\overline{c}_2$, $\overline{d}_0$, ... $\overline{d}_2$), or the proper coefficients improperly sequenced (as an input to either transformation program). The result of this type of error is usually the computation of incorrect magnitudes placed at a given U,V location in the transformed scene, and the output of zero magnitudes for some U,V if X,Y scene boundaries have been exceeded (since no stored data exists outside the boundaries).

The second type of error that can be readily verified is caused by specifying incorrect boundary locations in the transformation program for U and V. (In either case the correct U,V vertices used here were U_1 = line 1, ..., U_i = line 284; V_1 = column 1, ..., V_i = column 380, or 284 total lines and 380 total columns, and thus 107,920 total points.) The grey scale also allows verification that the g.c.p.'s utilized to determine the transformation coefficients were positioned properly in the (U,V) transformed data set. Since a linear transformation was utilized, if the proper location in U,V of these points is verified then the quality of the entire transformed data set can generally be assured. A complete description of the transformed data format used in this work is given in Appendix C.

Differencing Analysis

Point-by-point differencing was used in this work in an attempt to determine whether or not invariant temperature regions, or regions with large (±) variation from the average temperature could be located within the test site. Straight and mean-biased differencing was used in the analysis. In the implementation, a reference pattern was chosen

and from it test patterns were differenced. (In all cases this was performed with transformed data.)

It was desirable to use a reference pattern that was "thermally-representative" of the test site. The October day scene was arbitrarily chosen as the reference pattern for the day/day and day/night analyses. (It was convenient to utilize one reference scene for both cases.) In the night/night analysis the October night scene was chosen as the reference pattern. The September day and night scenes were not utilized as reference patterns due to bit dropouts and additions in both sets and the unreliable absolute calibration of the night set.

In addition, a synthetic day reference pattern was created from the four available registered day scenes by point-by-point averaging at each location ($U_1, \ldots, U_{284}$; $V_1, \ldots V_{380}$) in the transformed grid. Though not used as the primary reference pattern for day/day and day/night analyses it was utilized in each of these cases to determine whether or not the October day scene was "thermally-representative" of the signature of the test site. (It is expected that if a data set obtained under "thermally-unrepresentative" conditions is compared with another imaged under "normal" conditions the resulting correlation between scenes will be less than the maximum possible.)

In each case the differencing analysis was performed by a program named "NOAADIFF" developed by the author and written by Dr. Ronald Oines. Here the reference and test sets were read in, and point-by-point straight and mean-biased differencing was performed (using eqs. 2.28 and 2.32 as the respective algorithms), with the result of this processing stored on an output data tape. In addition, the mean of each data set was determined using the floating point data, and integer

truncated level-frequency histograms of the difference distribtuions were also computed. Here the level boundaries utilized were between $\pm 25^{o}C$ (ΔT), and a different histogram was presented for the mean-biased and straight difference algorithms. Even though the two difference distributions are identical except for their mean temperatures, it was, however, convenient to utilize the mean-biased difference distribution histogram in cases where the data set means varied significantly to avoid losing detail of a portion of the pattern from straight-differencing because of the level boundaries used.

In the straight difference analysis the result was an uncompensated point-by-point subtraction, while in the mean-biased case, points were determined in terms of their variation from the difference in data set means. Obviously those points in the straight difference analysis centered near zero ΔT were generally of large ΔT in the mean-biased analysis due to substantial differences between most data set means. In another operation after point-by-point differencing was performed each point was assigned to one of seven designated ΔT classes, whose boundaries are given in Table IV. Since one of the methods of evaluating this differencing information included grey scale analysis, it was felt that printing out straight and mean-biased points categorized within finite ΔT boundaries would allow a rapid initial investigation of the difference sets. Hence, the four point-by-point output data files created were the straight and mean-biased difference sets (both of which preserved the sign and magnitude of the individual points), and the straight and mean-biased difference "quantized" or classified ones. A complete description of the output data format used in "NOAADIFF" is given in Appendix C.

TABLE IV

BOUNDARIES USED FOR ΔT CLASSIFICATION

Class	Boundaries (°C)
1	$10.0 \leq \Delta T$
2	$6.0 \leq \Delta T < 10.0$
3	$2.5 \leq \Delta T < 6.0$
4	$-2.5 \leq \Delta T < 2.5$
5	$-6 \leq \Delta T < -2.5$
6	$-10 \leq \Delta T < -6$
7	$\Delta T < -10$

Two programs were available to assist in visually screening the resulting difference sets. The first was "GREY" (as previously discussed), and it was used in evaluating the mean-biased difference data. Two versions of "GREY" were usually run. The first involved plotting the classes assigned in "NOAADIFF" to the mean-biased data set. Here individual classes (having boundaries given above) were densenometrically represented in the grey scale, and areas of highest ± change (classes 1, 2, 6, 7) could easily be located. The second version then implemented utilized the exact mean-biased difference data (sign and magnitude preserved) to determine more accurately the resulting ΔT at locations of interest. Because of the generally large difference in data set means and due to the limited density range of "GREY", a second program was utilized to locate straight-difference regions near zero ΔT

(class 4). This program, named "PLOTCL" was developed and written by Dr. Ronald Oines.

Here a single line printer symbol is assigned to a given, numbered class. In addition to this, any combination of classes can be printed on the same form simultaneously, with a blank space left at every point not contained within a specified class. In this work "PLOTCL" was used to generate a map of straight-difference classes 3, 4, and 5. It should be noted that in this analysis class 4 included points centered around zero ΔT. The boundaries for this class were constructed within the range of scanner noise and data processing effects that were expected. Specifically, if a given region possessed temperature invariance over a period of time, a difference magnitude other than zero ΔT would generally appear in the geometrically registered data due to scanner noise and truncation error in the energy-to-temperature conversion of the raw data.

The NEΔT error (previously discussed) was typically found to be $\leq \pm.45^{o}C$. A high degree of confidence can be associated with the statement that this contribution was $\leq \pm.90^{o}C$. Truncation errors could account for another $\pm.5^{o}C$, thus the total error per point could be as much as $\sim\pm1.4^{o}C$. Hence at a given point in a differencing operation, two times this error of $\sim\pm2.8^{o}C$ could occur. The boundary for this "no-change" class (class 4) was set to $\pm2.5^{o}C$ for convenience in evaluation; i.e., a total range of $5^{o}C$. Classes 1 and 7 were open ended, i.e., all points out of range of the boundaries of the remaining classes, classes 3 and 5 had boundaries $3.5^{o}C$ apart, and classes 2 and 6 had ΔT boundaries $4^{o}C$ apart.

Thus from analyzing "GREY" and "PLOTCL" runs of the resulting difference data sets, observations could be made and related to terrain features, the corresponding geology, and the results of other difference sets in an attempt to determine if any type of invariant or time dependent conclusions could be drawn.

Crosscorrelation Analysis

Even though crosscorrelation is often used to determine the degree of similarity between a reference and test pattern, it also provides information relating to the shift location of the resulting magnitude peak. Subscene crosscorrelation was used to generate shift location information in two different cases in this work. In the first case it was utilized to verify registration accuracy in a subscene that contained a g.c.p. used in registering the transformed data, and secondly in predicting the total random registration error between the data sets in a region that did not contain any g.c.p.'s used in deriving transformation coefficients.

In the first case a 30×30 pixel subscene region was chosen in the Palo Verde (Colorado River) Valley southwest of Blythe, California. The reference pattern for the day/day and day/night analyses was obtained from the transformed October day scene (orbit 8874). Test pattern subscenes were likewise chosen from other transformed data sets, using identical line and column vertex boundaries as in the reference case. In the 30×30 pixel night/night analysis the October night (orbit 8880) and January night (orbit 9859) subscenes were used as reference patterns. Equation 2.19 was implemented as the crosscorrelation algorithm in a program named "CROSS". This program was developed and named

by the author and written by Dr. Ronald Oines. Later, an error in evaluating the limits of shift evaluation was detected. The corrected algorithm (which also contained compensation for the pyramid effect) was reprogrammed by the author with the assistance of Mrs. Marsha Adams of the OSU University Computer Center before reprocessing (the crosscorrelation of) all data subscene pairs. Grey scales of the mean-biased differencing analysis of this subscene region were utilized in each case to determine the degree of local change at a (0,0) shift (presumably).

In the second case a 40×40 pixel subscene region was used in the Santa Rosa Mountains west of the Salton Sea. Here, the reference subscene was chosen from the October day set and the test subscene from the December day set. Because of the significant difference in scan angles (α) to this region in the untransformed data, a large line (ΔEU) and column (ΔEV) differential spacing error would occur between the subscenes, as shown in Appendix B. Here the difference between the crosscorrelation peak line and column shift location and the predicted ΔEU and ΔEV gives the total random line and column error between the data sets at this subscene location. The subscene region evaluated was devoid of large scale man-made development and any other usable g.c.p.'s; thus providing a manner to verify registration accuracy in a region not containing such identifiable features.

In both cases the two data subscenes were read into the program from an on-line disk unit. The crosscorrelation algorithm was evaluated over the desired shift limits (±10 for the 30×30 case and ±20 for the 40×40 case). The resulting sign and magnitude of the normalized

crosscorrelation ρ as a function of shift was determined and printed at each of the (τ_i,τ_j) shift locations evaluated.

CHAPTER V

RESULTS

Registration Errors

The maximum observed line and column errors in g.c.p.'s using the mean coefficients determined in the registration process were found to range between $-1.0 \leq \Delta U \leq +1.0$ and $-2.0 \leq \Delta V \leq +2.0$ respectively. The significant difference between the line and column registration errors and a major component of these errors was primarily due to scan angle effects and the earth's curvature associated with the cross-track scan (in Y) of the sensor. This mainly appeared as a column error along a scan line (in V) although a line error component (in U) was also present. The remaining errors in each case were believed to be random in nature (although no specific analysis was performed to verify this). There was no case where a g.c.p. failed to register by more than twice the typical ranges presented above. The only detected case where a local non-linearity produced an error this large was a column registration error (+4.0) within a perimeter of g.c.p.'s in a small portion of the September day set. (A grey scale of the subsynch lines of this edit revealed no observable satellite roll error; the error was probably due to an unknown satellite attitude anomaly.) Ground control points, however, were often not available along the west edge and in the vicinity of the four corners of the test site due to a lack of

identifiable features, and it is thus possible that other local non-linearities could exist within the data.

No additional types of registration errors were observed from the g.c.p.'s utilized in this work. If such errors actually existed, failure to detect them was possibly due to the limited number of points that were identifiable from the data (the number of g.c.p.'s utilized in registration varied from 9 to 13). If several times more g.c.p.'s were available within the scene, other sources (i.e., local non-linear distortions) that contributed to the registration errors could possibly have been determined.

The minimum cell resolution size used in this work to examine regions of transformed and differenced data was given by EU lines by EV columns (eqs. B.19 and B.20) and ΔEU lines by ΔEU columns between data sets respectively. Analysis of spots smaller than these sizes would be invalid because of possible registration errors due to noise, scan angle and curvature effects between data sets.

Statistics of Transformed Data Sets

Temperature means, standard deviations, and ranges of the transformed data sets were calculated and presented in Table V. Since the data was in floating decimal form, the use of integer truncated level-frequency formulas in the standard deviation and mean computations was not exact but never-the-less of sufficient accuracy for the intended purpose here. Data set means utilized in the differencing analysis were determined from an exact floating point representation while the standard deviations were determined from the truncated histograms in a separate analysis. Approximate data set means were also computed

from these truncated histograms and presented for comparison in Table V.

TABLE V

RANGES, MEANS AND STANDARD DEVIATIONS OF THE TRANSFORMED DATA SETS

Orbit #	Range (°C)	Approximate M (°C) Calculated	Exact M (°C)	Approximate σ_{std} (°C) Calculated
2590	26	43.89	43.10	3.75
8477	27	28.24	28.42	3.00
8483	27	14.31	15.04	3.37
8874	34	14.52	14.79	4.00
8880	36	1.13	-.54	3.90
9481	24	4.00	4.26	2.65
9859	31	-9.23	-8.75	3.78
DAY.AVG	15	---	22.89	2.06

The large difference between exact and approximate means in the October night scene was due to warmer temperatures present south of the test site boundary being included in the computation from the histogram due to a transformation program quirk. Bit dropouts and (primarily) additions in five lines of data in the September night scene contributed to the difference in mean temperatures between the two methods. In the June day scene, however, no such dropouts existed and the variation

between the two computed means was due to truncation error as it was in all other cases. Because of this variable random error, test site means used in differencing analyses were computed directly from the floating point data and not from the truncated integer histograms.

In addition, a synthetic day scene, produced by averaging the four registered day scene values point-by-point was generated for use in the differencing analyses. The range and standard deviation of this average scene was considerably less than any of the individual day or night data sets. This indicates that a smoothing effect has occurred, in that a perturbation component due to thermal anomolies present in individual (day) scenes has been lessened in this average pattern.

Because of the many different terrain types present within the test site no attempt was made to determine a best fit distribution to the actual data by a specific statistical test (i.e., χ^2 test for non-normality). Had the test site area been homogeneous such an analysis might have provided intrinsic information related to the time varying properties of the region itself. In this case due to geographical, material and meterological heterogeneities an interpretation of any results would be very difficult. For reference, however, the transformed October day set histogram was plotted against a normal distribution whose peak height, mean and variance were obtained from the actual data and given in Figure 5. Here the gaussian distribution was normalized to the data peak height, not the total number of data points.

In this case some observations were made and related to the low temperature tail and high frequency temperature region above the mean of the distribution. A low pressure front (previously described) produced a near-standard atmospheric temperature gradient above the test

site and a noticeable surface temperature gradient from north to south ($2.8^{o}C$) and particularly northwest to south ($5.6^{o}C$) was present in the data set.

Examination of a grey scale of this data set revealed the following information. Generally, a decrease in surface temperature was observed with an increase in elevation, and consequently the highest elevation mountains (in the north, west and west-southwest) had the lowest temperatures within the site ($10^{o}C$ or more below the mean). Lower elevation valleys throughout most of the site had temperatures above the mean, with the warmest area (4^{o} to $7^{o}C$ above the mean) located in the south central region.

The other edit data distributions similarly appeared non-normal as the June and December day scenes were pseudo-bimodal, the September night scene pseudo-trimodal, the October night scene had a long high-temperature tail, while the September day scene and the January night scene had a long low-temperature tail.

Correlation Analysis

The validity of the correlation algorithm (eq. 2.19) was checked by performing an autocorrelation of the 30×30 October day subscene of the Palo Verde (Colorado River) Valley perviously edited. The results agreed exactly with theory; the correlation peak was located at (0,0) shift, had a magnitude of 1.000, and possessed an even symmetry with respect to shift (such that $\rho(-\tau_i,-\tau_j) = \rho(+\tau_i,+\tau_j)$, and $\rho(-\tau_i,+\tau_j) = \rho(+\tau_i,-\tau_j)$).

A crosscorrelation analysis was performed that utilized the 30×30 October day subscene as the reference pattern for day/day and day/

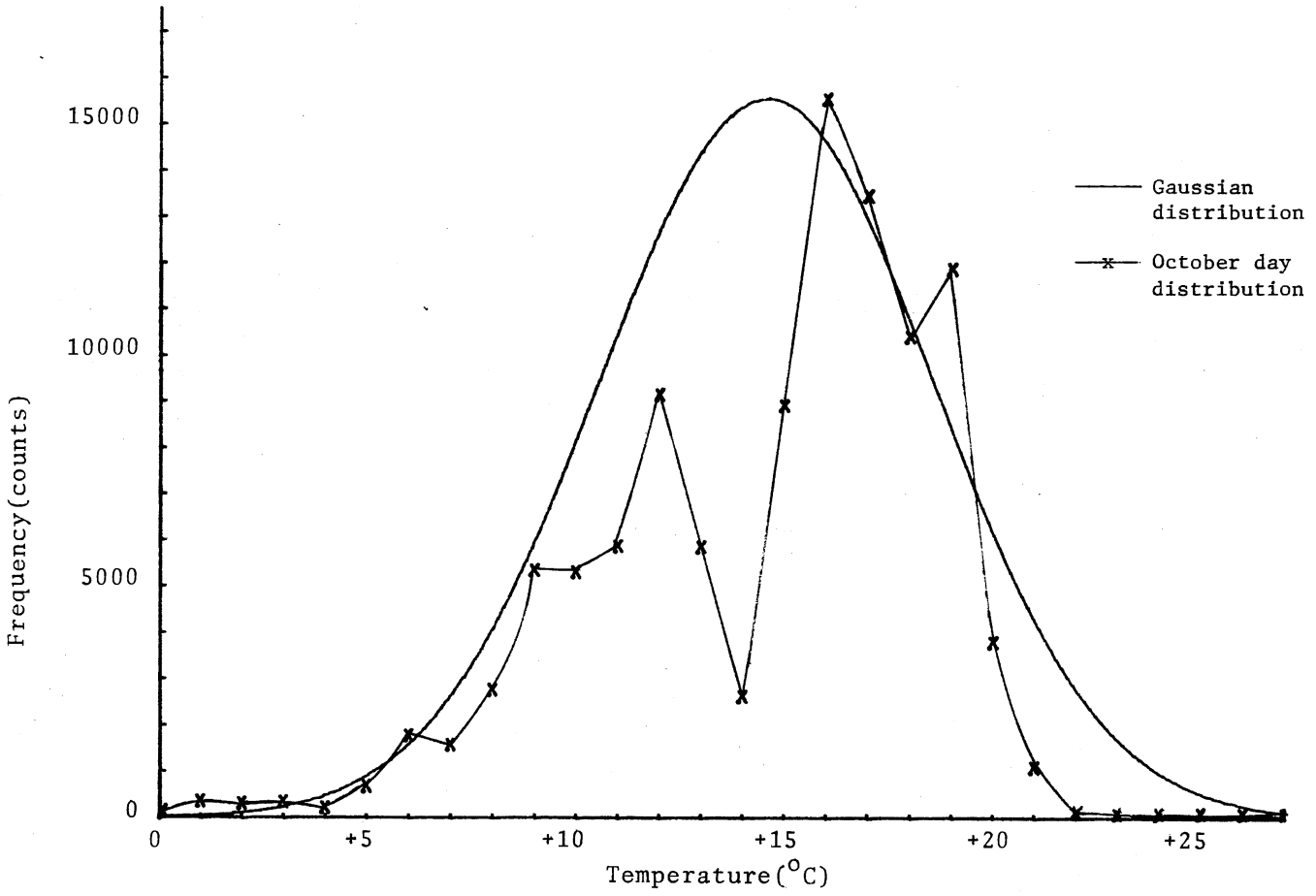

Figure 5. Comparison of Gaussian and October Day Data Distribution

night cases, the October 30×30 night subscene for night/night cases and the same subscene from other data sets as the test patterns. The peak magnitude, standard deviation of the noise/point, shift location of the peak (and its uncertainty), and the predicted registration error between the subscenes for day/day crosscorrelations are given in Table VI. For day/night and night/night analyses these results are presented in Table VII.

The peak magnitudes of 30×30 point day/day crosscorrelations performed with the October subscene were significantly less than those obtained between the other day/day subscene combinations. In addition, the peak magnitudes obtained from data that included the thermally inverted December day subscene were also reduced. It was clear from this that the October and December subscenes were not "thermally-representative" of the maximum correlatable data obtained from this region.

In the day/night analysis a crosscorrelation peak was determined in only two of the four cases. In the October/January and June/January day/night cases peaks were not found, but the distinctive shape of the river valley was visible in grey scales of the transformed data sets. Apparently, the crosscorrelation algorithm used was not sophisticated enough to detect this feature above the background noise. For reference purposes, grey scales of the October day and January night subscenes are presented in Figure 6. In both cases the darker a pixel is represented in the plots, the higher its temperature. (The mean temperatures of the October day and January night subscenes are 18.18^{o}C and -8.34^{o}C respectively. The apparent discrepancy in grey scale pixel sizes was due to using a smaller line printer chain in the January night subscene than the October day subscene.) The peak obtained in

TABLE VI

DAY/DAY CROSSCORRELATION PEAK MAGNITUDE, $\sigma_{n/p}$, SHIFT LOCATION, LOCATION UNCERTAINTY, AND PREDICTED REGISTRATION ERROR

Reference	Test	Peak Mg.	$\sigma_{n/p}$	Shift Location	Location Uncertainty	Predicted Registration Error
8874	2590	.6762	.0246	(-.5,1)	±(.25,.5)	(1.40,.87)
8874	8477	.6764	.0246	(0,4)	±(.5,.5)	(1.47,.43)
8874	9481	.5118	.0286	(-1,1)	±(.75,.5)	(-1.32,.78)
2590	8477	.8217	.0190	(.5,4)	±(.5,.25)	(-.07,1.30)
2590	9481	.7178	.0232	(0,0)	±(.5,.5)	(.08,1.65)
9481	8477	.6012	.0266	(1.5,2)	±(.75,.5)	(-.15,.35)
8874[1]	9481[1]	.7868	.0154	(-1.5,-5.5)	±(.5,.5)	[2]

[1]40×40 point West-Central case.

[2]See text.

TABLE VII

DAY/NIGHT AND NIGHT/NIGHT CROSSCORRELATION PEAK MAGNITUDE, $\sigma_{n/p}$, SHIFT LOCATION, LOCATION UNCERTAINTY AND PREDICTED REGISTRATION ERROR

Reference	Test	Peak Mg.	$\sigma_{n/p}$	Shift Location	Location Uncertainty	Predicted Registration Error
8874	8880	.4288	.0301	(.5,3.5)	±(1.0,.5)	(.22,1.06)
8874	9859	not found	----	----	----	(-.08,-.03)
2590	9859	not found	----	----	----	(1.32,.90)
8880	8477	.6263	.0260	(1.0,2.0)	±(.5,.75)	(1.68,-.63)
8880	8483	.8609	.0170	(0,0)	±(.5,.5)	(-.03,-.18)
8880	9859	.7975	.0201	(.5,-1.0)	±(.5,.5)	(-.29,-1.03)
9859	8483	.8415	.0180	(0,1.0)	±(.5,.25)	(.27,.85)

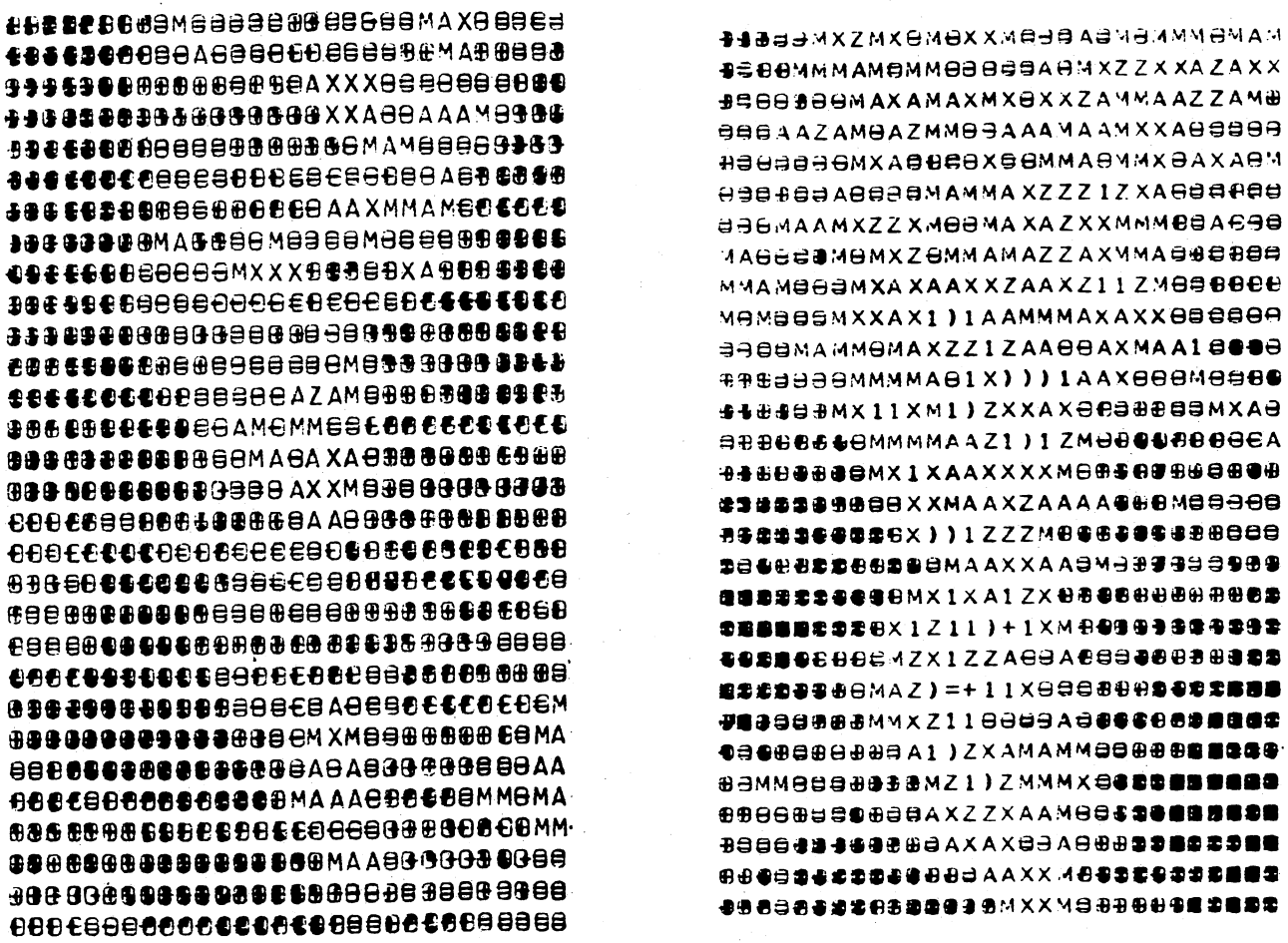

Figure 6. Grey Scales of October Day/January Night 30×30 Pixel Subscenes
(Palo Verde Valley; Colorado River)

the October night/September day case was significantly greater than that from the October day/October night case where the two edits were scanned only 11 hours apart. Again, it appeared that the October day subscene was "thermally-unrepresentative" of this region for day/night analysis. In both these day/night cases, however, the low peak magnitudes indicate a perturbation factor possibly related to material and atmospheric properties was present that could not be compensated for by simply removing the difference of the subscene means.

In the three night/night cases available crosscorrelation revealed a high degree of similarity between each of the subscenes. The magnitude peaks produced were all within ~7% of each other, and were among three of the four largest magnitudes of the 13 cases analyzed (30×30 point).

Assuming that the noise present between subscenes is statistically independent, a measure of the variation of the noise/point can be computed from the crosscorrelation peak magnitude. Specifically, the standard deviation of the noise/point is given by:

$$\sigma_{n/p} = \sqrt{\frac{1 - \rho^2}{n_p - 1}} \quad , \tag{5.1}$$

where ρ = the magnitude of the crosscorrelation peak, and

n_p = the number of points in a subscene.

The result of this analysis for day/day and night/night cases was that variations present in peak magnitudes generally (except in the October-Decmeber and June-September day cases) fell within $3*\sigma_{n/p}$ of those in their respective groups. The large magnitude of the June-September peak produced a significant variation from all other $\sigma_{n/p}$ day/day cases analyzed. In the day/night cases where a peak was identified the $\sigma_{n/p}$

was large due to the small peak magnitude. Because of the similarity of crosscorrelation peak magnitudes within the day/day and night/night cases, an analysis was performed to determine whether or not the perturbations present within a case group were correlated. This analysis is presented in Appendix D.

Because of its potentially high processing rate, differencing was chosen as the main analysis tool for this work. The differencing was performed at (0,0) shift between the reference and test data sets, thus assuming registration. Consequently any large uniform misregistration between data sets would substantially degrade the quality of the resulting analysis.

From Tables VI and VII the only 30×30 point crosscorrelations with peak shift locations $\geq$ 2 lines or columns from (0,0) involved the October night and September day subscenes. In all other cases where a peak was determined, registration differences between data subscenes were within acceptable limits, and consequently differencing performed at a (0,0) shift would introduce small errors. In addition, for all day/day and night/night cases a correlation peak was readily determined above the background noise. However, only in two of the four day/night cases was a peak located, and hence, the basic concept of correlatability in this case is somewhat questionable.

In the day/night case that utilized the October night subscene the moderate shift location from (0,0) was related to the difficulty experienced in determining the exact (shift) position of the peak above the background noise. In the cases that utilized the September day subscene a non-linear local column error (in Y) was apparently present in the untransformed data scene from Blythe to Yuma (north→south) and east

of the Colorado River to the test site border. This error was also located by using "TRNSFM" (specifically eq. 2.12), but could not be removed in registration due to its local, non-linear nature. Here representative ground control existed over much of the remainder of the test site in this data set compared to the subscene area. Crosscorrelation of another subscene locale would yield peak shift locations closer to (0,0) than in the Palo Verde Valley case; thus this data set was useable in the differencing analyses.

Given the standard deviation of the noise/point ($\sigma_{n/p}$) for each of the crosscorrelations obtained from the subscene pairs, a measure of uncertainty estimated in the shift location (τ_i, τ_j) of the peak can be determined. This measure is an indication of the degree of accuracy to which the shift location of the crosscorrelation peak can be found in the presence of background noise. Since the perturbation (or difference) between subscene pairs may be time dependent, no simple relationship between $\sigma_{n/p}$ and the estimated shift error may exist. Generally stated, however, crosscorrelations between subscene pairs that have a low resulting peak magnitude (large $\sigma_{n/p}$) will have a larger estimated error of the peak shift location than those cases with much higher peak magnitudes (lower $\sigma_{n/p}$).

This location uncertainty in τ_i and τ_j was determined by a graphical approximation method with a sensitivity of $\pm(\frac{1}{4},\frac{1}{4})$ lines and columns from the crosscorrelation magnitudes as a function of shift location in the peak neighborhood. Hence the location of the crosscorrelation peak is given by ($\tau_i \pm \text{error}_{\text{lines}}$, $\tau_j \pm \text{error}_{\text{columns}}$).

A comparison can be made between the shift location (± uncertainty) of the crosscorrelation peak and the predicted error between the

subscenes utilized; as determined from the registration procedure (i.e., eqs. 2.11 and 2.12). Here the crosscorrelation was performed over a local region while the geometric transformation utilized was global since coefficient means determined from the scene g.c.p.'s were used. Two of the three cases where the predicted error and peak shift location (± uncertainty) overlapped occurred in night/night analyses; which also had the largest peak magnitudes of any case analyzed (day/day, day/night, and night/night). At least here, local (subscene) and global ground control was quite similar, but this was generally not the case in most other data set pairs analyzed. From this, adequate registration between data sets may be obtained by using global transformation coefficients, but localized variations in ground control due to non-linear variables, measurement errors and noise may never-the-less exist.

A second crosscorrelation case was analyzed in this work. Here a region, which contained no significant man-made development, was obtained from a portion of the test set devoid of g.c.p.'s used in registration. It was located near the horizontal (east→west) edge of the transformed data sets and analyzed to determine the approximate total random line and column error between the data sets. The area utilized was the 40×40 October and December day subscenes previously described. The line and column displacement from center (after transformation) was approximately 14 (U) and 170 (V) respectively for both data sets. Here the ΔEU and ΔEV errors were computed to be -3.38 and -5.39 respectively, while the shift at the crosscorrelation peak was (-1.5,-5.5). From eqs. B.21 and B.22 the total random line error was approximately +1.88, and the total random column error was approximately -.12.

The standard deviation of the noise/point in this case was computed to be .0154, the smallest of any determined. Here, the October reference subscene standard deviation was exactly 50% larger than the (thermally inverted) December test subscene standard deviation.

Differencing Analysis

Point-by-point differencing was performed in the processing of the data sets after registering. In each case reference and test sets were selected which allowed day/day, day/night and night/night comparisons to be generated. Two different operations in each of two cases were then invoked in every analysis. In the first case each point was subtracted without compensation between reference and test sets and in a simultaneous second operation then catalogued into one of seven difference classes (previously discussed). In the second case the difference of the means was subtracted; then the points were similarly assigned into two groups as in the straight difference analysis.

Because of calibration problems in the September night edit no straight difference data from this set was utilized in this work. Here the entire data set was approximately average temperature biased to an unknown extent, but spatial continuity was preserved and the data set was incorporated in the mean-biased analysis. In this work the straight difference class (4) centered around zero ΔT is referred to as "no-change", and the mean-biased difference class (4) centered around the average ΔT is referred to as "average-change".

Histograms of the distribution of the points in the seven mean-biased difference classes and the "no-change" class were computed and presented in Table VIII. The histograms revealed that few points were

usually contained near zero ΔT (class 4) (at least in part due to the large difference between most data set means), while most were clustered near the mean difference between the reference and test sets (average ΔT). Presented in Table IX is the percentage of the total points found in the "no-change" class, "average-change" class, and the three central mean-biased classes (3, 4, and 5).

TABLE VIII

HISTOGRAMS OF MEAN-BIASED CLASSES AND THE STRAIGHT DIFFERENCE "NO-CHANGE" CLASS

Class	Difference Set[1]							
	2590	8477	8483	8880	9481	9859	8483n	9859n
1	2742	542	139	137	24	221	1160	113
2	10982	2622	4451	5070	4381	6901	2385	1617
3	17423	19398	23120	29087	23574	26659	15283	13949
4	40823	63458	55737	46810	53347	43852	73207	75169
5	25138	17695	18891	17229	18893	19382	13624	16009
6	9802	3737	4385	6864	6676	8746	1347	983
7	1010	468	1197	2723	1025	2159	914	26
4[2]	1	85	nc[3]	1083	2785	0	nc	1420

[1]Reference set - 8874 except 8483n and 9859n where reference set was 8880.

[2]Straight difference class 4 ($-2.5^{o}C \leq \Delta T \leq 2.5^{o}C$).

[3]Not calculated.

TABLE IX

PERCENTAGE OF THE TOTAL POINTS IN "NO-CHANGE" CLASS, "AVERAGE-CHANGE" CLASS AND THREE CENTRAL MEAN-BIASED CLASSES

Class	Orbit[1]										
	2590	8477	8483	8880	9481	9859	8483n	9859n	8874[2]	8880[2]	DAY.AVG[2]
A	9.27D-4	.079	nc	1.84	2.58	0.0	nc	1.32	n/a	n/a	n/a
B	37.83	58.80	51.65	43.38	49.43	40.63	67.84	69.65	41.33	57.23	70.79
C	77.26	93.17	90.57	86.29	88.78	83.30	94.62	97.41	91.20	86.36	98.17

A = "No-Change"
B = "Average-Change"
C = 3 central Mean-Biased Classes (3, 4, and 5)
n/a = not applicable
nc = not calculated

[1]Reference set - 8874 except 8483n and 9859n where reference set was 8880.

[2]8874, 8880 and DAY.AVG reference sets mean-biased to 0.0 test set.

The class boundaries utilized did not artificially alter the resulting difference distributions. Examination of discrete histograms between ±25°C for the mean-biased analysis revealed relatively smooth, quasi-symetrical distributions in all cases, as did the resulting histograms of the generated classes.

The count in the "average-change" class for night/night sets (Table VIII) was significantly greater than any day/day or day/night sets (∿9.0% greater than the maximum day/day and ∿17% greater than the maximum day/night sets). Observation of grey scales produced from mean-biased night/night processing revealed temperature similarities (near the average ΔT) between the reference and test patterns that often extended over large areas; such that many terrain features visible in grey scales of day/day or day/night patterns due to anomalies related to the thermal signature were no longer discernable. Obviously, crosscorrelations of these night/night difference set pairs should be significantly higher than in the day/day or day/night cases.

The straight difference patterns obtained from day/day, day/night and night/night analyses were analyzed for inclusive regions around zero ΔT, specifically in the "no-change" class larger than the (previously determined) minimum cell size. In the day/day analysis (where the reference was the October day scene) the September and December day test scenes contained two and 32 "no-change" regions respectively. The two "no-change" regions in the September day case were located at the southwest portion of Salton Sea (in water) and the eastern edge of the Laguna Salada in Northern Baja California (possible water; elevation ∿100'). Of the 32 identified "no-change" regions in the December day difference case, 31 were mountainous varying in altitude from 300' to ∿7500', the

remaining one occurred in the Valle De Laguna Salada (elevation ∿200'), in Northern Baja California. Of the 31 mountainous regions only three were identified as wooded by the maps (USGS 1--6, 1969 and 1970). The June day case produced zero "no-change" regions when differenced from the October day scene. (The only "no-change" point present was probably due to noise.)

In the day/night analysis (where the reference was the October day scene) only the October night (diurnal; obtained 11 hours later) test scene produced "no-change" regions. (The September night scene was not included due to calibration difficulties.) Of the seven "no-change" regions that were identified here, five were mountainous and two water. The mountainous regions ranged in elevation from 300' to 6500', with two of the four represented as wooded by the maps (USGS 1--6, 1969 and 1970). Of the two water bodies, the largest was the Salton Sea of which > 90% of its area was in the "no-change" class. The other was a small portion of the Colorado River opposite Lake Havasu City, Arizona, where relatively small river currents were probably present. In both the October/December day/day and October/October day/night analysis the eastern portion of the Sierra Juarez Mountains and the west-central portion of the Cerro Los Cupapas Mountains (centered on the Valle De Laguna Salada) had "no-change" regions (USAMS, 1938, and Geo. S. A., 1971).

In the night/night analysis only the October (reference)-January (test) case was investigated (due to the calibration difficulties of the September night scene). Of the 12 "no-change" regions identified, nine were mountainous whose elevations (three of which appeared wooded from the maps (USGS 1--6, 1969 and 1970)) ranged from 2500' to 7500'.

The remaining three regions were valleys; two of which were free of standing water and between 1700' and 2000' elevation. The third was the Palo Verde Valley between 33.2°N and 33.7°N latitude and 500' to 700' elevation through which the Colorado River flows.

The only water "no-change" region located commonly between two or more difference sets was the Salton Sea (October/September day and October day/October night). Large "no-change" areas in the Little San Bernardino and Santa Rosa Mountains to the north and west respectively of the Salton Sea were determined in the October/December day and the October day/October night difference pairs. Due to minimum cell sizes imposed, however, only small overlapping regions between the difference pairs were detected. Additional common "no-change" areas also found in these difference pairs corresponded to the Granite, eastern Sierra Juarez and western-central Cerro Los Cupapas Mountains. Elevations in the Little San Bernardino (∿4000') and Granite Mountains (wooded and ∿6500') would not have been favorable to snow cover until December. Snow was also probably not related to the "no-change" regions present in the eastern Sierra Juarez (∿800') and western-central Cerro Los Cupapas (∿800') Mountains due to the moderately low elevations.

In the mean-biased patterns, large common areas of highest (±) change and "average-change" were located in the day/day, day/night, and night/night difference pairs. Only highest (±) change regions common to multiple mean-biased difference sets were of interest here since most areas tended (on an overall basis) to be near the average ΔT, specifically in the central three classes (±6°C). In the day/day analysis mountains in the west, north and northwest had significant variations (-6°C to -12°C) from the difference of data set means. Only in the

October/December day analysis did some of these highest change regions associated with the mountains correspond to zero ΔT. (In this case the smallest variation between reference and test set means was observed of any day/day data set pair.) In addition to this, valleys through much of the site (including the Colorado River Valley) consistently had a large (+) deviation from the difference of data set means, although in no case were any close to zero ΔT.

Because of the large extent of common high (±) change mean-biased temperature regions between all day/day difference sets, the question of whether or not the October day scene was "thermally-representative" of the other day scenes was raised. This lead to the crosscorrelation analysis between pairs of the three other Palo Verde Valley (30×30 pixel) day subscenes, which showed (at least) for this region the October day scene was "thermally-unrepresentative" of the remaining three. Multiple observations from mean-biased difference gray scales revealed that several other anomalous areas (besides the Palo Verde Valley region) also appeared to exist, thus indicating that the October reference set was not (globally) "thermally-representative" of the (test site) data utilized.

In the day/night analysis mountains in the west and southwest had significant variations (-6°C to -12°C) from the difference in data set means. Only in the October day/night case did some of these highest change regions that were associated with mountains correspond to zero ΔT. The Borego Valley west of the Salton Sea was consistantly above the difference in data set means as were most of the valleys in the north-central portion of the site, the La Posa Plain (east of the Palo Verde Valley), and the area south of the Chocolate Mountains into Mexico.

As in the day/day case, simultaneous observation of continuous magnitude grey scales revealed many similarities between the day/night difference sets. The October night/September day 30×30 subscenes of the Palo Verde Valley were then crosscorrelated and the results showed a significantly higher peak magnitude than in the October day/night case. Thus the October day scene was not the best choice as a reference pattern for diurnal crosscorrelations in (at least) the subscene region tested. Hence on the basis of these observations the October day scene also appeared to be thermally anomalous for use in diurnal crosscorrelations. Again, multiple observations from mean-biased difference gray scales indicated that the October reference set was not (globally) "thermally-representative" of the (test site) data utilized.

In the night/night analysis of the two difference cases had few anomalous regions in common; in most regions temperatures were centered near the average ΔT. Two exceptions to this appeared in both difference cases. The first included the Salton Sea ($+6^{o}C$ to $+11^{o}C$ above the mean) and the Colorado River between Lake Havasu City and Parker Dam ($\sim+6^{o}C$ to $+10^{o}C$ above the mean). The other case was in the valleys of the central region which contained dune sand and were between $6^{o}C$ and $10^{o}C$ below the mean. From this analysis it appeared that the October night reference set was thermally similar to the two other night scenes used as test patterns.

Geology of the Locations of "No-Change" Regions

A preliminary analysis was made to determine whether or not any correlation could be confirmed between the "no-change" regions and the geology associated with these locations.

From the analysis of the geology of the "no-change" regions detected, most of these areas corresponded to features that contained pre-Cenozoic era rocks, and were of moderate density. Only two cases were found where "no-change" areas were associated with alluvial materials; the first in the Mohave Valley; the second south of Chemehuevi Peak. Both of these cases were in the northeastern portion of the test site, were of low elevation (500'-2000'), and found in the October/January night difference set. It did not appear from this analysis that the geology of the locations that corresponded to "no-change" regions was weighted significantly towards any particular rock type relative to the frequency of occurrence of that type in the terrain. For example, many of the "no-change" regions that corresponded to mountains were associated with granite or metamorphic rock, but most of the mountains in the test site were composed of this type of material. In some cases terrain associated with "no-change" regions was bounded by geological units, while in other cases it was not.

Determination of the Site Correlation Coefficient

In this analysis the correlation coefficient at (0,0) shift between a reference and test set was directly computed from the statistics of these data sets and the resulting difference distribution. In each case the data sets were assumed to be registered before differencing. Hence, the resulting correlation coefficient is determined at a (0,0) shift, and not at the shift-location of the maximum possible magnitude obtained (the true peak).

Data set standard deviations were previously computed and presented in Table V. Data utilized in this computation was in integer-truncated level-frequency form, hence some (small) errors were introduced. In addition, in the three night scenes, data south of the test-site boundary was included due to a transformation program quirk. This additional data was believed to have elevated the standard deviation of these scenes somewhat; in particular the October edit.

Means and standard deviations from the eight mean-biased difference sets were computed and presented in Table X. Here by definition the distributions should have a mean $\equiv 0.0$. The computed means agreed quite well to this; the largest deviation, $M_D = .225$, was in the September night case. The standard deviation of the mean-biased difference sets were computed from the discrete mean zero data with a standard level--frequency formula.

If the reference and test data sets were statistically independent random variables, then the variance of the sum of these variables (σ_0^2) would be equal to the sum of their individual variances. Hence:

$$\sigma_0^2 = \sigma_r^2 + \sigma_t^2 \tag{5.2}$$

or

$$\sigma_0 = \sqrt{\sigma_r^2 + \sigma_t^2} \ .$$

Actually, the variance of the difference set (σ_D^2) is given by:

$$\sigma_D^2 = E[r - t]^2 = E(r)^2 - 2E(rt) + E(t)^2$$

$$= \sigma_r^2 - 2\rho(0,0)\sigma_r\sigma_t + \sigma_t^2 \ . \tag{5.3}$$

After rearranging terms the site correlation coefficient, $\rho(0,0)$ of the two data sets is given by:

TABLE X

MEANS, STANDARD DEVIATIONS, C_n, CORRELATION COEFFICIENTS, RANK OF DIFFERENCE SETS AND THE STATISTICALLY INDEPENDENT STANDARD DEVIATIONS BETWEEN THE REFERENCE AND TEST SETS

Reference	Test	σ_D(°C)	M_D(°C)	σ_0 (°C)[1]	C_n[2]	$\rho(0,0)$	Rank[3]
8874	2590	4.60	.10	5.48	.84	.297	8
8874	8477	2.89	-.11	4.98	.58	.695	3
8874	8483	3.15	.23	5.24	.60	.647	4
8874	8880	3.92	-.06	5.59	.70	.509	6
8874	9481	3.43	-.03	4.80	.71	.532	5
8874	9859	4.02	-.04	5.51	.73	.466	7
8880	8483	2.62	.17	5.16	.51	.751	2
8880	9859	2.20	-.05	5.43	.41	.831	1
DAY.AVG	2590	2.25	-.09	4.28	.53	.858	-
DAY.AVG	8880	2.66	.17	4.41	.60	.770	-

[1] $\sigma_0 = \sqrt{\sigma_r^2 + \sigma_t^2}$

[2] $C_n = \sigma_D/\sigma_0$

[3] Rank (between 1 and 8) for crosscorrelation peaks.

$$\rho(0,0) = \left[1 - \frac{\sigma_D^2}{\sigma_r^2+\sigma_t^2} \right] \left[\tfrac{1}{2} \right] \left[\frac{\sigma_r}{\sigma_t} + \frac{\sigma_t}{\sigma_r} \right] . \qquad (5.4)$$

If

$$C_n = \frac{\sigma_D}{\sqrt{\sigma_r^2 + \sigma_t^2}} , \qquad (5.5)$$

then eq. 5.4 becomes:

$$\rho(0,0) = \left[1 - C_n^2 \right] \left[\tfrac{1}{2} \right] \left[\frac{\sigma_r}{\sigma_t} + \frac{\sigma_t}{\sigma_r} \right] . \qquad (5.6)$$

The term:

$$\left[\tfrac{1}{2} \right] \left[\frac{\sigma_r}{\sigma_t} + \frac{\sigma_t}{\sigma_r} \right]$$

in eq. 5.6 deviated from 1.00 only as the difference between reference and test set standard deviations became large. Also presented in Table X is σ_0, σ_D, C_n and $\rho(0,0)$ for the eight mean-biased difference cases analyzed, plus the two mean-biased cases that utilized the DAY.AVG pattern as the reference scene.

Table IX contained the percentage of the total points determined in the "average-change" class for the eight mean-biased difference sets. In each of the eight cases the computed correlation coefficient ($\rho(0,0)$) and this percentage had the identical rank in terms of peak magnitude versus percentage of points in the "average-change" class. At least in the data utilized in this analysis, the percentage of total points in the "average-change" class was an accurate indicator of the relative site crosscorrelation at (0,0) shift.

The difference between the 30×30 pixel Palo Verde Valley subscene crosscorrelation peaks previously computed and the overall site correlation coefficient was between ∿5% and ∿20% for five of the eight

cases. No discernable peak could be located in the October day/January night subscene crosscorrelation and the October day/September night subscene crosscorrelation case was overlooked and not run. In the October/June day case, however, a poor correspondence existed between the subscene crosscorrelation and site correlation peak magnitudes. This was believed to be related to a reversed north→south surface temperature gradient in the June day scene, and anomolous temperatures present between the patterns caused by differing local (material) thermal inertias due to a significant difference between the two data set scan times (∿1.5 hours). Other possible causes for this discrepancy were examined and rejected for lack of evidence. (An analysis of the atmospheric and ground temperature gradients of the test site area at the edit times and their possible effect on data quality is presented in Appendix E.)

A differencing analysis was performed between the DAY.AVG pattern and the June day and October night scenes to determine if the October day scene was "thermally-unrepresentative" of the test site signature for both day/day and day/night analyses. In addition, it was of interest to determine if the resulting site correlation coefficients utilizing this average pattern were higher than those obtained with the October day reference scene. (The October day scene, however, was one of the four data sets used to generate the average pattern. Furthermore, since these day scenes were obtained over a six month period of time, at least some smoothing of any seasonal effect would be present in this average pattern.)

As shown in Table X, a large resulting increase in correlation occurred by using the average day pattern instead of the October day

scene in the two day/day (189%) and day/night (51%) cases analyzed. From this it is clear that the October day scene was globally "thermally-unrepresentative" of the test site signature and the resulting degree of correlation obtained in day/day and day/night cases using the average pattern was considerably higher and acceptable.

CHAPTER VI

CONCLUSIONS, DISCUSSION AND RECOMMENDATIONS

Conclusions

The following conclusions were drawn from the analyses performed in this work:

1. From the site correlation coefficients determined (at (0,0) shift) by statistics from the transformed data and difference distributions, the reference and test sets were neither uncorrelated nor statistically independent. A higher degree of (site) correlation was observed in the night/night case than in the day/day and day/night cases that utilized the October day reference scene. When the average day scene was utilized as a reference pattern in day/day and day/night cases, however, the correlation between data sets increased significantly to the degree obtained in the night/night case. The percentage of points in the "average-change" class was an accurate qualitative indicator of the site correlation coefficient between difference sets.

2. Patterns produced by day/day differencing that utilized the October day reference scene appeared to be correlated with each other. In the day/night difference cases that utilized the October day reference scene the patterns also appeared to be correlated with each other; while in the night/night case the resulting difference patterns appeared to be uncorrelated with each other. From data used in this work, the night/night site correlations were acceptable, as were those

in the day/day and day/night cases that utilized the average day reference scene. In those day/day and day/night cases that used the October day reference scene, however, the resulting correlation between data sets was only marginally acceptable at best. This was at least in part due to the anomalous October day reference scene, and thus utilizing a more "thermally-representative" reference pattern did increase the degree of correlation obtainable. In any of these analyses, the choice of a "thermally-unrepresentative" reference pattern will lead to reduced correlation.

3. A substantial portion of any "seasonal effect" present between the thermal IR data sets used in this work was eliminated by removing the average temperature component present. The remaining perturbation component due to meterological, material and seasonal effects between data sets, however, may be difficult to predict.

4. The distributions produced by differencing were quasi-symetrical in nature with most points centered near the difference in data set means (average ΔT). Few points were found near zero ΔT in most difference distributions, which was at least in part due to the large difference between most data set means analyzed.

5. Only a few temporally common "no-change" regions existed between difference sets. In no case were any of these regions present in all difference sets.

6. Abnormal directional surface or atmospheric temperature gradients can affect the thermal signature of a siven site. Such a factor cannot generally be eliminated by removing the average temperature component present, and may be difficult to quantify unless accurate meterological information is available.

7. Global (mean) transformation coefficients were used to register the data to acceptable error limits. Adequate ground control was obtained from the global transformation coefficients for data registration, but local variations (distortions) did exist between data sets due to non-linear variables (scan angle effects, etc), measurement errors, and noise.

8. A major component of the column registration errors present in the transformed data (in V) was due to the non-linear effects of the sensor scan angle and the earth's curvature. Since a linear transformation was used to register the data, these distortions were not removed by this process.

9. The level--frequency shape of each of the transformed data sets deviated from a normal distribution due to the heterogeneous composition of the test site. No obvious time-dependent (i.e., diurnal, seasonal) relationship existed among the distributions of these data sets.

10. From the preliminary analysis performed there was no apparent correspondence between the location of "no-change" areas and the large-scale geology associated with these regions.

Discussion

Among the data sets, some thermal discrepancies existed between similar terrain classes within the test site. These anomalies are of two basic types; those related to constant physical properties that can be predicted, and secondly, those related to phenomena whose effects could not be compensated for in this work.

The analysis to determine whether or not a correspondence existed between "no-change" regions and the associated geology was only preliminary, and the results should not be broadly extrapolated. No attempt was made to compensate for factors such as the material density of the surface and subsurface, short wavelength reflectivity, long wavelength emmissivity, elevation, thermal inertia, surface conditions (i.e., coatings), soil types and depths, and vegetation present, and consequently, the analysis was limited to a correspondence with the gross geology.

Accurate ground truth can usually be obtained for constant factors such as differing densities of the upper surface fractions (i.e., between sand and rock), cover type (i.e., vegetation to bare surface), thermal inertia of materials and the geological formations present. Furthermore, since these factors are invariant or slowly varying they will not produce significant changes in the correlation between different data sets.

In the second case, however, factors such as the amount of precipitable water in the atmosphere, the atmosphere temperature gradient, and the directional air surface temperature gradient vary with time and local weather conditions throughout the test site. In addition, observed temperatures are influenced by locally varying material (thermal inertia, etc.) properties due to variations in local scan times between data sets. It would be extremely difficult to obtain adequate quantitative data related to these factors close enough to real time because of the large number of "representative" recording stations that would be necessary. Consequently, the resulting pre-processing analysis would be complex and far too costly to implement. The use of such a

pre-processing analysis in a test study (such as this work), however, might increase the overall correlation between data sets since these factors can have a significant influence on the thermal signature of the site.

From this work it appeared that the major perturbation components present between data sets were related to seasonal, material and meteorological factors. At least a major portion of the seasonal effect present between data sets used in this work can be eliminated by removing the average temperature present between scenes, as demonstrated in Figure 9. It should be noted, however, that as scan times are moved closer to local sunrise or sunset, seasonal changes between data sets due to slope differences between curves become important. Hence, the seasonal perturbation component between data sets is minimized only when data is scanned sufficiently away from local sunrise and sunset, and should increase if data is obtained near these times.

Perturbations due to material effects (including thermal inertia) were present between all data sets due to different time-dependent temperature responses of materials within the site. Consequently, this perturbation component is maximized when data sets are obtained at significantly different scan times; particularly for diurnal investigations. Hence, even if seasonal and meteorological perturbation components present are minimized, the correlation between day/night (diurnal) data sets should be less than that for day/day and night/night sets. In addition, it may be very difficult to quantify the different perturbation components between day/night data sets since in observed data there will be at least some correlation between the effects of material and meteorological factors even if the seasonal component is minimized.

In example, day/night data will be influenced by the material perturbation component present, but since test site meteorlogical conditions may be strongly time dependent (as in this case) no simple relationship may exist between the material perturbation component and observed diurnal temperature variations. Thus, a simple relationship may only exist if the meteorological perturbation component present between data sets can be minimized. Furthermore, if observations are made over long time periods this analysis will be further complicated by the correlation between seasonal (sun's declination) and material (time of observation) perturbation components present.

Finally, the meteorological perturbation component present between data sets can have a significant influence on the observed difference temperatures, and hence on the correlation between scenes. Even in day/day or night/night analyses, if seasonal and material perturbation components can be minimized by the proper selection of scan times, little control may exist over the meteorlogical perturbation component present. Since abnormal atmospheric and directional surface air temperature gradients, variations in the precipitable water concentration present and the passage of fronts over the site may only be weakly correlated joint events no simple procedure for their determination and compensation is likely to exist. Consequently, the observed effect of this perturbation component on the correlation between data sets may range from small to large, and will in general not be related to an average temperature difference between scenes.

Since an objective of this work was to explore the concept of correlatability between data sets imaged at different times and applications to different types of possible hardware systems a summary of

these findings for the thermal IR analyses performed here is given.

From the analyses performed the zero ΔT and hybrid concepts would fail as viable approaches for hardware systems. Only in three of the five straight difference cases analyzed were any "no-change" regions detected. Furthermore, none of these invariant regions was temporally common to more than two difference sets. Such a hardware system would require temporally common, thermally invariant regions to exist for position-locating purposes. Hence, in either the zero ΔT or hybrid cases, since no such required regions were found, an uncorrelated output would occur and the concept would not be applicable.

In addition, since all (surface) materials have defined thermal properties (i.e., thermal inertia, short wavelength reflectivity, etc.), which directly influence the observed temperature, there is no indication based upon radiation theory that "no-change" regions should exist over any significant period of time. It is clear that significant variations in the meteorological perturbation factor between data sets can increase the probability of occurrance of "no-change" regions, but because of the time dependent nature of this perturbation component no invariant relationships may exist. It may be possible, however, to maximize "no-change" regions between data sets by selecting day and night observation times shortly after local (seasonally adjusted) sunrise and sunset when the thermal contrast between materials is minimized.

Based upon this work, however, it is possible that the average ΔT concept could be utilized in such a position locating system. If "thermally-representative" or synthetic (averaged) reference patterns

are used an acceptable degree of correlation could exist between day/day and night/night cases to warrant further investigation of this approach for hardware applications. It is clear, however, that the correlation between day/night cases may only be marginally acceptable unless the material perturbation component is minimized and the scene component is related to the average ΔT present. In this case observations made near sunrise and sunset would tend to increase the degree of correlation between data sets if seasonal and meteorological effects can be removed since anomalous temperature differences due to the material perturbation component are minimized.

Even for day/day and night/night cases, however, a significant meteorological perturbation component present in the data could reduce the degree of correlation below the maximum possible. In addition, if a test scene was imaged with substantial cloud cover present an unacceptably low degree of correlation could exist between patterns. For that reason, it has previously been stated that a microwave radiometer, assuming similar thermal radiation phenomena apply, would be a better all-weather prospect.

As in any detailed investigation, errors were made by the author in applications of theory and data processing that impeded the course of this work. Some of these are pointed out to the reader in hope that they can be avoided in future work.

The primary theoretical error made was related to properties of the distributions derived from differencing. In differencing two data sets, only one distribution is produced at a given shift location (i.e., (0,0) as used in this work). Mean-biased differencing only changes the location of the distribution mean from $(\bar{r} - \bar{t})$ in the unbiased

case to zero. All other properties of the distribution remain the same. Furthermore, since $(\overline{r} - \overline{t})$ was generally large, points near zero ΔT often had significant deviation from the average ΔT. Consequently, temperature-invariant points would actually tend to reduce correlation in a system developed around an average ΔT approach.

In data processing some of the problems encountered that were unrelated to general errors follow.

1. Selecting the proper line locations for edit pull-offs from the raw data tapes was often difficult due to the varying vertical dimension of the photographic imagery provided. Since it was necessary to remove a specific area from the CCT in each case, a vertical overlap of 10% (top line) and -10% (bottom line) of the total number of desired lines was found to provide a sufficient safety factor. It is better to pull off too many lines of data in this type of work than not enough, which would force a rerun.

2. In the temperature conversion processing, manual verification of computer determined scene temperatures is necessary to detect processing errors. Reading the wrong calibration bytes (as done in one case in this work) can lead to significant errors, but subtle and more difficult-to-detect ones can occur in other stages of the conversion. Because of the non-linearity of Planck's equation, a uniform shift during conversion will lead to errors that cannot strictly be eliminated by mean-biasing.

3. It should be noted that a transformation program set up to handle day orbit data (such as LANDSAT) may not function properly when night orbit data is included. In day scenes the (1,1) point is in the upper left-hand corner, but in night scenes it occurs in the lower

right-hand corner. The difference between the two cases is equivalent to a 180° rotation in terms of pixel location. Consequently, it may be necessary to use a form of complimentary location numbering (as used here) to avoid this problem.

4. Due to the above transformation problem and in spite of the complimentary numbering that was included, a +20 column shift in the program numbering marker was noted for all night data. This led to the erronious assumption that the data was actually shifted +20 columns with respect to day data, and consequently all day/night processing was initially performed in a manner that shifted the night data -20 columns. As was later noticed by accident, the +20 column shift did not actually exist in the data at all, but only in the marker used for column numbering. Because of this all diurnal investigations had to be rerun without column shift compensation.

In addition, a general processing problem was often encountered with some data and scratch tapes utilized. It should be noted that digital tapes have a finite lifetime and serious problems can arise if highly processed data sets are stored on a tape that becomes defective. It is suggested that any data set having been processed in two or more analyses be duplicated on another tape to prevent such a problem. The effort necessary to do this is considerably less than that needed to read or load past a defective segment of a tape, or regenerate the "lost" data sets.

Recommendations

Based upon the results of this investigation, the following recommendations are made for further research and development efforts.

1. Consideration should be given to the method used in choosing reference patterns for thermal IR differencing or crosscorrelation. As demonstrated here, a "thermally-unrepresentative" reference pattern produced decreased correlation peaks. If possible, a "representative" reference pattern obtained under average scan times and meteorological conditions should be used. A better approach might be to create synthetic day and night reference patterns by determining the average value at every point in (U,V) from the respective data set groups as done in this work. This will tend to smooth out thermal anomalies that can be present in the data.

2. An investigation should be made to develop a less "analyst-dependent" approach to geometric registration than used here. Approximate geometric registration could be obtained from equitorial-crossing ephemeris data if an expression could be determined between this information and the scanner attitude over the test site. If one of the patterns is registered to a standard projection, then alignment of subsequent data sets near the scene center can be obtained by subscene crosscorrelations.

3. An investigation should be made to determine the maximum effective pixel size that can provide adequate correlation between data sets. From the scanner's frame of reference, this is related to altering the ifov used in collecting the data, and it can be approximated by replacing the value at a given point in the data set by the average value computed from a neighborhood. This will simulate the process of integrating the terrain signal over a larger aperature stop. By changing the size of the neighborhood, this approximates a varying scanner ifov. If a larger ifov can provide thermal signatures that have an

acceptable degree of correlation, then increased real-time processing rates are possible.

4. An investigation should be made with multispectral thermal IR, or thermal IR and microwave data imaged from the same test site to see if any improvement in site correlation is obtained from data sets having multispectral thermal signatures. Such an investigation should also attempt to determine if pre-processing the multispectral signatures by a technique such as principal components can increase the correlation between data sets. Because of the high degree of spectral redundancy typically present in multispectral data, the first principle component (from two or more original spectral bands) might provide more information related to the thermal signature than could be obtained from any individual spectal band. This could increase the resulting degree of correlation between data sets. (An analysis to determine whether or not intrinsic information related to the test site thermal signature is contained within day/day, day/night and night/night principal component eigenvectors is currently under way. Here the temporal dimension replaces the commonly used spectral dimension in this study, and the principal components are computed from available transformed day and night data sets.)

5. If vhrr data is to be used in an investigation where the registration error must be minimized, then redistribution of the data (in terms of equal increments of dγ of the earth's surface) should be utilized after temperature conversion to reduce scan angle and curvature effects. Redistribution should not be attempted before temperature conversion unless precautions have been taken to preserve the line-by-line calibration data.

6. Further investigation should be made to determine the minimum degree of correlation (or from this a minimum SNR) necessary to allow a given correlation hardware system to generate accurate position and heading information.

7. An investigation should be made to find the maximum amount of cloud cover that can be present in the data, and yet still provide the necessary minimum acceptable thermal signature for correlation. (Clouds can be simulated by blocking out spatial regions of the pattern. To avoid the swamping effect on the pattern mean, and minimize the increase in variance in the resulting difference distribution, a value equal to the mean of the remainder of the pattern can be assigned to points within their boundaries.) Assuming that registration can be obtained, an analysis should be performed to determine the effect that varying the amount of cloud cover would have on the site correlation coefficient. From this an upper-limit on the amount of cloud cover present in a data set that would yield acceptable correlation in a given case could possibly be determined.

A SELECTED BIBLIOGRAPHY

Anuta, Paul E. Spatial Registration of Multispectral and Multitemporal Digital Imagery Using Fast Fourier Transform Techniques. LARS Information Note 052270, Laboratory for Applications of Remote Sensing, West Lafayette, Indiana: Purdue University, 1973.

Anuta, P. and M. Bauer. An Analysis of Temporal Data for Crop Species Classification and Urban Change Detection. LARS Information Note 110873, Laboratory for Applications of Remote Sensing. West Lafayette, Indiana: Purdue University, 1973.

Baker, R., and E. M. Mikhail. Geometric Analysis and Restitution of Digital Multispectral Scanner Data Arrays. LARS Information Note 052875, Laboratory for Applications of Remote Sensing. West Lafayette, Indiana: Purdue University, 1975.

Bakis, R., M. A. Wesley, and F. M. Will. "Digital Correction of Geometric and Radiometric Errors in ERTS Data." Proceedings of the 7th International Symposium on Remote Sensing of the Environment, Vol. II. Ann Arbor, Michigan: Univ. of Michigan, 1971, pp. 1427-1436.

Barnea, Danial I., and Harvey F. Silverman. "A Class of Algorithms for Fast Digital Image Registration." IEEE Transactions of Computers, Vol. C-21, No. 2 (February, 1972), pp. 179-186.

Bartolucci, L. A., R. M. Hoffler, and T. R. West. Computer-Aided Processing of Remotely Sensed Data for Temperature Mapping of Surface Water from Aircraft Altitudes. LARS Information Note 042373, Laboratory for Applications of Remote Sensing. West Lafayette, Indiana: Purdue University, 1973.

Bernstein, R. "Digital Image Processing of Earth Observation Sensor Data." IBM Journal of Research and Development, Vol. 20, No. 1 (Jan. 1976), pp. 40-57.

Breaker, Larry, NOAA-NESS, private communication, 1975.

Conrow, Edmund H., unpublished data, 1975-1976.

Daghir, Earnie, NOAA-NESS, private communication, 1976.

Geological Society of America (Geo. S. A.). Reconnaissance Geologic Map of the State of Baja California (1:250,000 geological map). Compiled by R. Gordon Gastril et al. Boulder, Colorado, 1971.

Hooper, J. O., and J. B. Seybold. "Microwave Radiometric Images." In Remote Sensing of Earth Resources, Proceedings of the Third Conference on Earth Resources Observation and Information Analysis System, Vol. III. Tullahoma, Tennessee: University of Tennessee, 1974, pp. 174-191.

Kawarnura, Joseph G. "Automatic Recognition of Changes in Urban Development from Aerial Photographs." IEEE Transactions on Systems, Man, and Cybernetics, Vol. SMC-1, No. 3 (July, 1971), pp. 230-239.

Kennedy, J. M., A. T. Edgerton, R. T. Sakamoto, and R. M. Mandl. Passive Microwave Measurements of Snow and Soil. Space General Corporation, Contract No. NOnr4767(00); NR387-033, Office of Naval Research, Technical Report No. 2 (Vols. 1 and 2), Washington, D. C.: ONR, 5 November, 1966.

Kennedy, J. M. "Interaction Mechanisms." Manual of Remote Sensing, Vol. 1. Ed. Robert G. Reeves. Falls Church, Virginia: American Society of Photogrammetry, 1975, pp. 163-165.

Kniskern, Frank, NOAA-NESS, private communication, 1975.

Koffler, Russell, NOAA-NESS, private communication, 1975.

Koffler, Russell, NOAA-NESS, private communication, 1976.

La Rocca, Anthony J. "Methods of Calculating Atmospheric Transmittance and Radiance in the Infrared." Proceedings of the IEEE, Vol. 63, No. 1 (January, 1975), pp. 75-94.

Leeman, Virginia, Diane Earing, Robert K. Vincent, and Sharon Load. The NASA Earth Resource Spectral Information System: A Data Compilation. Willow Run Laboratories, University of Michigan, NASA Contract Report (CR)--31650-24-T, Houston, Texas: NASA Manned Spacecraft Center, May, 1971.

Legeckis, Richard and John Pritchaird. Algorithm for Correcting the VHRR Imagery for Geometric Distortions Due to the Earth's Rotation and Curvature. Preprint, NOAA Technical Memorandum, Washington, D. C.: NOAA-NESS, January, 1976.

Lillestrand, Robert L. "Techniques for Change Detection." IEEE Transactions on Computers, Vol. C-19, No. 7 (July, 1972), pp. 654-659.

Macleod, I. D. G. "Correction of Pictorial Output With a Line Printer." IEEE Transactions on Computers, Vol. C-19, No. 9 (Sept. 1970), p. 851.

McGillem, D. D., and M. Swedlow. "Image Registration Error Variance as a Measure of Overlay Quality." IEEE Transactions on Geoscience Electronics, Vol. GE-14, No. 1 (January, 1976), pp. 44-49.

Moore, Robert P. "Microwave Radiometric All-Weather Imagery and Piloting Techniques." Conference on the Guidance and Control of V/STOL Helicopters at Night and in Poor Visibility, NATO, AGARD Conference Proceedings (CP-148), May, 1975, pp. 8-1--8-10, unclassified.

Mundie, Lloyd G., Robert F. Hummer, Robert, L. Sendall, and Donald S. Lowe. "System Design Considerations for Advanced Scanners for Earth Resources Applications." Proceedings of the IEEE, Vol. 63, No. 1 (Jan. 1975), pp. 95-103.

Nathan, Robert. "Picture Enhancement for the Moon, Mars and Man." In Pictoral Pattern Recognition, Proceedings of the Symposium on Automatic Photointerpretation. Ed. George C. Cheng. Washington, D. C.: Thompson Book Company, 1968, pp. 239-266.

National Aeronautics and Space Administration (NASA) (Deerwesster, J. M., et al.). Data Acquisition Systems for Operational Missions. NASA Technical Memorandum, TMX-62, 107. Washington, D. C.: NASA, February, 1972.

National Aeronautics and Space Administration--Jet Propulsion Laboratory (NASA-JPL)(Siegal, Barry S., et al.). Final Report on the Detection of Geothermal Areas from Skylab Thermal Data. NASA Technical Memorandum, Technical Memorandum 33-728, Pasadena, California: Jet Propulsion Laboratory, NASA, June, 1975.

National Aeronautics and Space Administration--Johnson Space Center-1 (NASA-JSC-1). Operation and Maintenance Manual, Multispectral/Microwave Data Analysis Station. NASA Contract NASA 9-9-9627, TM 1353-1. Houston, Texas: NASA, Vol. 1, May, 1971.

NASA-JSC-2. Aircraft Data Storage Tape Format, LARYSYS Version 2. NASA, 1974.

NASA-JSC-3 (Pitts, D. E., et al.). Atmospheric Transmission Computer Program CP. NASA Technical Memorandum, TM X-58137. Houston, Texas: NASA-JSC, December, 1974.

NASA-JSC-4. NASA 24 Channel Multispectral Scanner System Training Course. Houston, Texas: Information Systems Division, NASA-JSC, n. d.

NASA-JSC-5. Data Quality, Multispectral Scanner. LEC/HASD 640-TR-056, NASA Contract NAS 9-12200. Houston, Texas: Lockheed Electronics Company, December, 1971.

National Oceanic and Atmospheric Administration (NOAA-1)(Schwalb, A.). Modified Version of the Improved TIROS Operational Satellite (ITOS D-G). NOAA Technical Memorandum, NESS-35. Washington, D. C.: NOAA-NESS, 1972.

NOAA-2. Tape Format and Temperature Conversion Information for ITOS VHRR Scanners. Suitland, Maryland: NOAA-NESS, n.d.

Office of Naval Research. Handbook of Military Infrared Technology. Ed. William L. Wolfe, University of Michigan, Contract Nonr1224 (12), Office of Naval Research, Washington, D. C.: ONR, 1965.

Phinney, Dale, Lockheed Electronics Company, HASD, private communication, 1975.

Pitts, D. E., NASA-JSC, private communication, 1975.

Pohn, H. A., T. W. Offield, and Kenneth Watson. "Thermal Inertia Mapping from Satellite--Discrimination of Geologic Units in Oman." Jour. Research U. S. Geologic Survey, Vol. 2, No. 2 (March-April, 1974), pp. 147-158.

Rand McNally, Rand McNally Road Atlas. New York, New York: Rand McNally and Company, 1975, p. 19.

Reeves, Robert G. (Ed.). "Image Interpretation." Manual of Remote Sensing, Vol. 2. Falls Church, Virginia: American Society of Photogrammetry, 1975, pp. 964-965.

Riffman, Samual S. "Evaluation of Digitally Corrected ERTS Imagery." Management and Utilization of Remote Sensing Data. Ed. Abraham Anson, Falls Church, Virginia: American Society of Photogrammetry, 1973, pp. 206-221.

Ronsefled, Azriel. "Automatic Detection of Changes in Reconnaissance Data." Proc. 5th Conv. Mil. Electron. (1961), pp. 492-499.

Schaerer, G. A Comparison of Thermal Imagery at Microwave and Infrared Wavelengths. Bern, Switzerland: Bern University (for Swiss Department of Military, NTIS Number N76-10553), June, 1974.

Siegel, R., and John R. Howell. Thermal Radiation Heat Transfer. New York, New York: McGraw-Hill Book Company, 1972.

Tisdale, Glen E. "A Versatile Technique for the Automatic Extraction of Information from Reconnaissance Images." Proceedings of the 1971 National Aerospace Electronics Conference, IEEE, (1971), pp. 166-171.

United States Army Map Service (USAMS). Mexicali (N-1 11-S)(1:500,000 Topographic Map). Washington, D. C.; Edition 1, 1938.

United States Geological Service-1 (USGS-1). El Centro (NI 11-12)(1:250,000 Topographic Map). USGS, Denver, Colorado, Edition 3, 1969.

USGS-2. Needles (NI 11-6)(1:250,000 Topographic Map). USGS, Denver, Colorado, Edition 4, 1969.

USGS-3. Salton Sea (NI 11-9) (1:250,000 Topographic Map). USGS, Denver, Colorado, Edition 4, 1969.

USGS-4. San Bernardino (NI 11-5) (1:250,000 topographic map), USGS, Denver, Colorado, Edition 3, 1969.

USGS-5. San Diego (NI 11-11) (1:250,000 topographic map), USGS, Denver, Colorado, Edition 4, 1970.

USGS-6. Santa Anna (NI 11-8) (1:250,000 topographic map), USGS, Denver, Colorado, 1969.

Watson, K., L. C. Rowan and T. W. Offield. "Application of Thermal Modeling in the Geologic Interpretation of IR Images." Proceedings of the International Symposium on Remote Sensing of the Environment, Vol. III. Ann Arbor, Michigan: University of Michigan, 1971, pp. 2017-2041.

APPENDIX A

THERMAL IR AND MICROWAVE RADIATION ANALYSIS

Since remotely sensed thermal data was used in this analysis a review of the governing physical relationships in the thermal IR and microwave regions of the spectrum is presented.

If we assume that an object behaves as a blackbody (a perfect emitter in each direction and at every wavelength where the total radiation is a function only of temperature) then the amount of energy emitted by that object into a unit hemisphere at a given wavelength is given by (Siegel and Howell, 1972, p. 19):

$$e_{\lambda b}(\lambda) = \frac{2\pi hc_{\ell}^2}{\lambda^5(e^{hc_{\ell}/\lambda kT} - 1)} \frac{\text{power}}{(\text{area})(\text{wavelength})} , \qquad (2.1)$$

where $e_{\lambda b}(\lambda)$ is known as Planck's spectral distribution of emitted power;

λ = the wavelength of radiation;

T = the absolute temperature of the body;

h = the Planck's constant;

k = the Boltzman constant; and

c_{ℓ} = the speed of light in a vacuum.

To simplify the evaluation of eq. 2.1 two approximations are often employed. The first, known as Wien's approximation, is applicable for wavelengths of $\sim$10μm or less and is implemented by neglecting the -1

factor in the denominator (Hooper and Seybold, 1974). This approximation is accurate to within 1% for $\lambda T <\sim 3{,}125(\mu m)(^{o}K)$.

The second, known as the Rayleigh-Jeans approximation, expands the exponential term in the demonimator of eq. 2.1 as a power series:

$$(e^{hc/\lambda kT} - 1) = 1 + (\frac{hc_{\ell}}{\lambda kT}) + \frac{1}{2!}(\frac{hc_{\ell}}{\lambda kT})^2 + \ldots + \frac{1}{w!}(\frac{hc_{\ell}}{\lambda kT})^w - 1 \quad , \qquad (A.1)$$

which for $\lambda kT >> hc$ becomes:

$$e^{hc_{\ell}/\lambda kT} \cong 1 + \frac{hc_{\ell}}{\lambda kT} \qquad (A.2)$$

An attempt can be made to linearize Planck's equation by using the Rayleigh-Jeans approximation in the thermal IR region by substituting the truncated power series (eq. A.2) into eq. 2.1. If the linearization is justifiable, the resulting form of Planck's equation can be simply integrated over the desired wavelength band to obtain the emitted power at a given temperature. If this approximation is invalid, however, the resulting integration of the non-linear form of Planck's equation is much more difficult.

Though correct in the microwave portion of the spectrum the linearization is incorrect in the thermal IR because the product of wavelength and temperature is far too small. Specifically, the power series approximation of the exponential (eq. A.1) is incorrect for $\lambda T < 14{,}388(\mu m)(^{o}K)$ (because $hc_{\ell}/\lambda kT > 1$), and the Rayleigh-Jeans approximation (eq. A.2) is accurate to within 1% for $\lambda T > \sim 96{,}850(\mu m)(^{o}K)$. This λT product ($\lambda T > 96{,}850$) is well outside the range generally encountered in thermal radiation problems since a blackbody emits over 99.9% of its energy at λT values below this (Siegel and Howell, 1972, p. 746).

At T = 292°K, λ would have to be $\sim$50μm or more for eq. A.1 to be valid, and $\sim$.332 mm or more for eq. A.2 to be accurate within 1%.

Hence the assumption that eq. A.2 properly expresses the expansion of eq. A.1 for usual λ, T found in thermal IR data, and can be substituted into eq. 2.1 and integrated to obtain a linear relationship between emitted energy and temperature in invalid except in very small temperature and wavelength intervals.

The governing factor to the accuracy of linearization in a small λ, T range is the product of the two variables. This is demonstrated by Figure 7 where $e_{\lambda b}(\lambda)$ (eq. 2.1) has been normalized by T^5; thus replacing multiple blackbody curves at a given T by a single curve of $e_{\lambda b}(\lambda,T)/T^5$ in terms of the single variable λT (Siegel and Howell, 1972, p. 22). Here the peak of the normalized equation occurs at λT = 2,898 (μm)(°K). The linearization errors resulting from the improper use of eq. A.2 can be traced to this peak region. When λ = 10μm and 285°K $\leq$ T $\leq$ 295°K the function rapidly changes slope, passes through zero slope, the slope changes sign and the function again rapidly changes slope. Thus any linearization attempt in the 8 to 14 micron thermal IR range for ambient temperatures (centered near the λT peak) will lead to substantial extrapolation errors outside this interval. This is demonstrated by Figure 8 for 9.3μm $\leq \lambda \leq$ 11.7μm and 253°K $\leq$ T $\leq$ 333°K, where a maximum error of 7°C exists between the linearization and integration of eq. 2.1 (Bartolucci, et al., 1973). In fact, this error increases non-linearly as the width of the temperature interval increases (with a constant λ interval) in the thermal IR λT range.

It is possible over a thermally homogeneous region that a temperature range of $\leq$ 10°C may exist and linearization thus be accurate. To

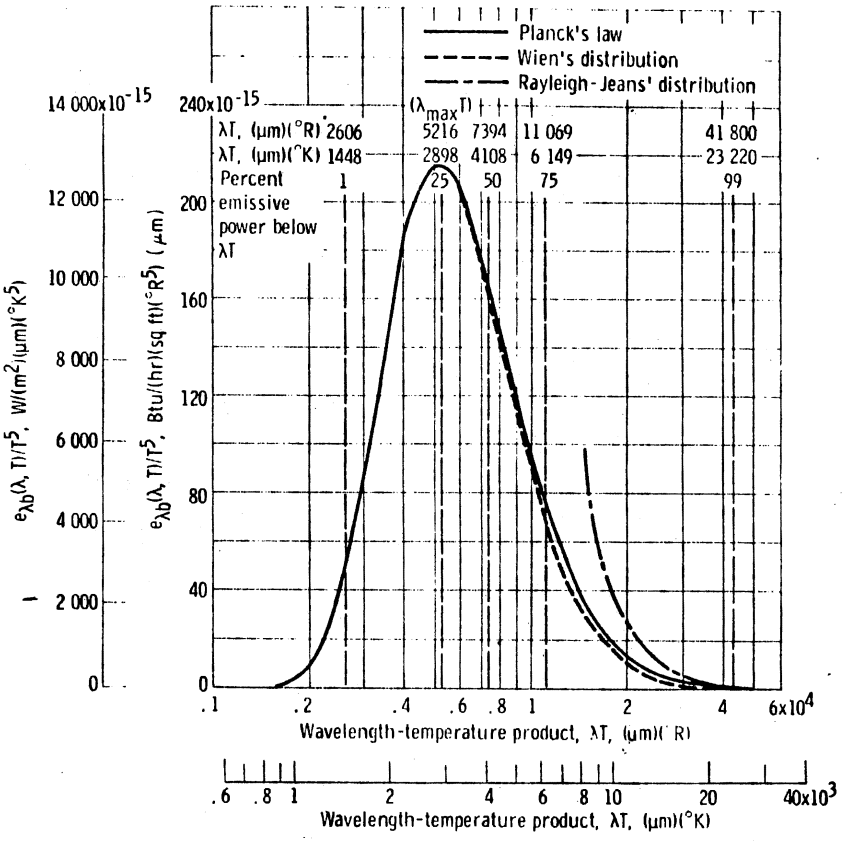

Source: Siegel, R., and John R. Howell. Thermal Radiation Heat Transfer. New York, New York: McGraw-Hill Book Company, 1972, p. 22.

Figure 7. Spectral Distribution of Blackbody Hemispherical Emissive Power

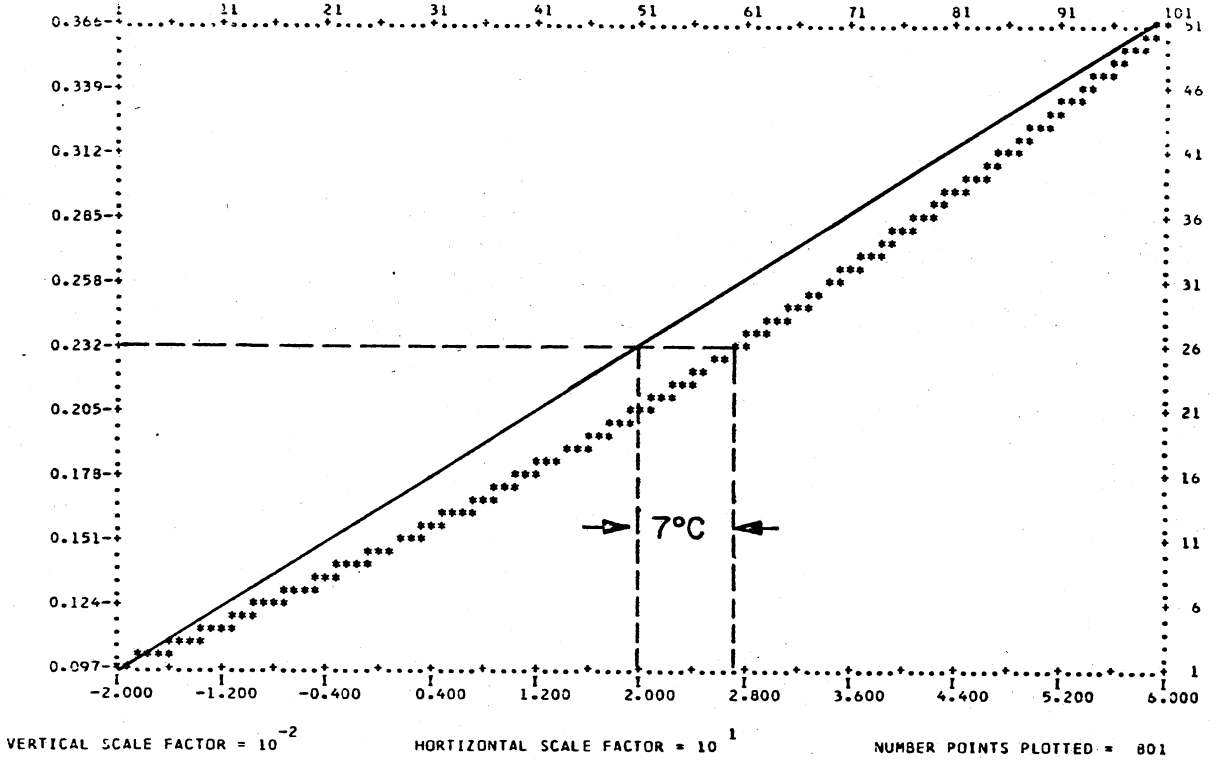

Source: Bartolucci, L. A., R. M. Hoffer, and T. R. West. Computer-Aided Processing of Remotely Sensed Data for Temperature Mapping of Surface Water From Aircraft Altitudes. LARS Information Note 042373, Laboratory for Applications of Remote Sensing. West Lafayette, Indiana: Purdue University, 1973, p. 62.

Figure 8. Computer-Plotted Curve (Asterisks) Showing the Relationship Between the Amount of Emitted Energy by a Blackbody (Vertical Axis) and Its Temperature (Horizontal Axis) in the 9.3-11.7 Micrometer Spectral Band. Integration Between -20°C and 60°C.

be valid for an overall quantitative analysis, however, this requires an "a priori" knowledge of the thermal properties of the region being investigated. In high altitude airborne and satellite imagery where sensor system parameters (such as aircraft velocity/height ratio, pixel size and total scan angle) may vary significantly from low altitude airborne imagery, thermally dissimilar regions may be scanned having temperature variations >> $10^{o}C$.

For cloud-free NOAA-3 vhrr thermal IR data (pixel size = .91km at nadir) obtained under conservative thermal conditions, temperature variations in a small subframe (400 lines by 800 elements) typically exceed $25^{o}C$ over land and $40^{o}C$ over land/water (ocean) (Conrow, 1975 and 1976). Due to the mission nature of the NOAA-ITOS satellites, the internally calibrated vhrr thermal IR sensors have a dynamic operating range of $150^{o}C$ or more (Koffler, 1976). Here numerical integration of eq. 2.1 between $10.5\mu m \leq \lambda \leq 12.5\mu m$ for $180^{o}K \leq T \leq 330^{o}K$ is required to maintain calibration accuracy (Breaker, 1975). In plotting $e_{\lambda b}(\lambda)$ versus T over this temperature range and narrower ones for other thermal IR sensors a quasi-linear relationship may exist within small regions ($\sim 10^{o}C$), but slope extrapolation outside a given temperature interval can introduce unacceptably large calibration errors. Furthermore, these errors can be several times greater than the sensor system NEΔT; thus negating any benefit obtained by using relatively "noise-free" data in a thermal investigation where temperature conversion is utilized followed by a quantitative analysis.

For microwave wavelengths (large λ; consequently λT is generally >> $96{,}850(\mu m)(^{o}K)$) eq. A.2 is an accurate representation of the power series and can be utilized with negligible error. Substituting eq. A.2

into eq. 2.1 for microwave wavelengths we find that

$$e_{\lambda b}(\lambda) = \left[\frac{2\pi k c_{\ell} T}{\lambda^4} \right] \frac{\text{power}}{(\text{area})(\text{wavelength})} \quad . \tag{2.2}$$

Thus in this wavelength region the emitted power is directly proportional to the absolute temperature of the radiating body. In the thermal IR if we utilize Wien's approximation and integrate the modified eq. 2.1 over a wavelength band we find that the emitted power is proportional to the fourth power of the absolute temperature. Specifically the hemispherical emissive power over a wavelength interval (λ_1 to λ_2) in the thermal IR is:

$$e(T)\Big|_{\lambda_2}^{\lambda_1} = \varepsilon(T)\Big|_{\lambda_2}^{\lambda_1} \sigma T^4 \quad , \tag{A.3}$$

where σ = Stefan-Boltzman constant, and ε = the ratio of emissive power of the object to that of a blackbody. (For a blackbody $\varepsilon(T) = 1.00$.)

Watson (1971) developed a model relating absorbed thermal flux into the ground to a product of physical properties and diurnal surface temperature. Since the temperature of an object is a result of its energy balance and material characteristics, these relationships allow a preliminary examination of the thermal response of a material to its environment. The thermal flux absorbed into the ground (in a given period) is equal to the sum of the incident solar flux, the atmospheric heat transfer flux and the reradiation flux from the ground (negative). Specifically, the general thermal flux and those for daytime and nighttime are given by:

$$\phi_n = \phi S_n + \phi A_n - \phi G_n \quad , \tag{A.4}$$

$$\text{daytime } \phi_n = c_c S_0 (1 - \rho_g) H_T(Z) \cos Z + \sigma T_{AD}^4 - \varepsilon \sigma T_n^4 \quad , \tag{A.5}$$

$$\text{nighttime} \quad \phi_n = \sigma T_{AN}^4 - \varepsilon\sigma T_n^4 \quad , \tag{A.6}$$

where ϕ_n = absorbed thermal flux in the nth interval into the ground;

ϕS_n = absorbed solar flux in the nth interval;

ϕA_n = atmospheric heat transfer flux in the nth interval;

ϕG_n = reradiation from ground in the nth interval;

c_c = cloud cover factor;

S_0 = solar constant;

ρ_g = (short wave) reflectivity of ground;

ε = mean emissivity of ground (spectral average);

σ = Stefan-Boltzman constant;

T_{AN} = effective nighttime air temperature;

T_{AD} = effective daytime air temperature; and

$H_T(Z)$ = atmospheric transmission.

For simplicity the photometric effects of the surface, including topography, surface roughness, and scattered illumination from the sky are ignored, and atmospheric heat transfer and reradiation from the ground are treated as effective heat transfer terms, using the Stefan-Boltzman law. Since $S_0 = 0.0$ at night, eq. A.5 effectively reduces to eq. A.6.

With these relationships, the thermal flux can be computed and related to predicted temperature by:

$$\phi_n = \frac{P_i}{(\pi\zeta)^{\frac{1}{2}}} \sum_{s=1}^{w} T_{g,s}\psi_{q-s+1} \tag{A.7}$$

where P_i = thermal inertia of the ground;

ζ = period of the thermal flux;

$T_{g,s}$ = ground temperature in the sth interval; and

ψ_{q-s+1} = set of coefficients determined by the number of incremental steps, q, in the period ζ.

With the relationships given in eqs. A.4 through A.7, the effect of altering any group of parameters can be determined and displayed as predicted temperature versus local solar time. One plot of interest in this work is presented in Figure 9 and given diurnal surface temperature variations computed at local solar time for different seasons at 30°N latitude for a constant set of material and atmospheric properties.

As Figure 9 shows, the slopes of the seasonal curves are nearly constant with respect to each other except within approximately ±2 hours of the equinox sunrise and sunset times. Since the test site was centered near 33°N latitude this predicted relationship at 30°N latitude should apply with minimal differences. In essence this plot demonstrates that if the D.C. bias is removed the resulting curves are similar except near sunrise and sunset where differences in slope (and magnitude) appear.

Also plotted on Figure 9 is the scan time/season intersection for each of the seven data sets utilized in this work. From this it appears that the day and night data was obtained a sufficient time after local sunrise and sunset to minimize "seasonal effects". In these cases mean-biasing can theoretically remove an average temperature component present due to differences in the sun's declination.

Another plot of interest in this work is that of diurnal surface temperature variations computed at local solar time for materials of differing thermal inertia as given in Figure 10. The thermal inertia of a material is a measure of the rate of heat transfer between two dissimilar media at an interface and in its simplest form is equal to the material's heat conductivity divided by the square root of its thermal

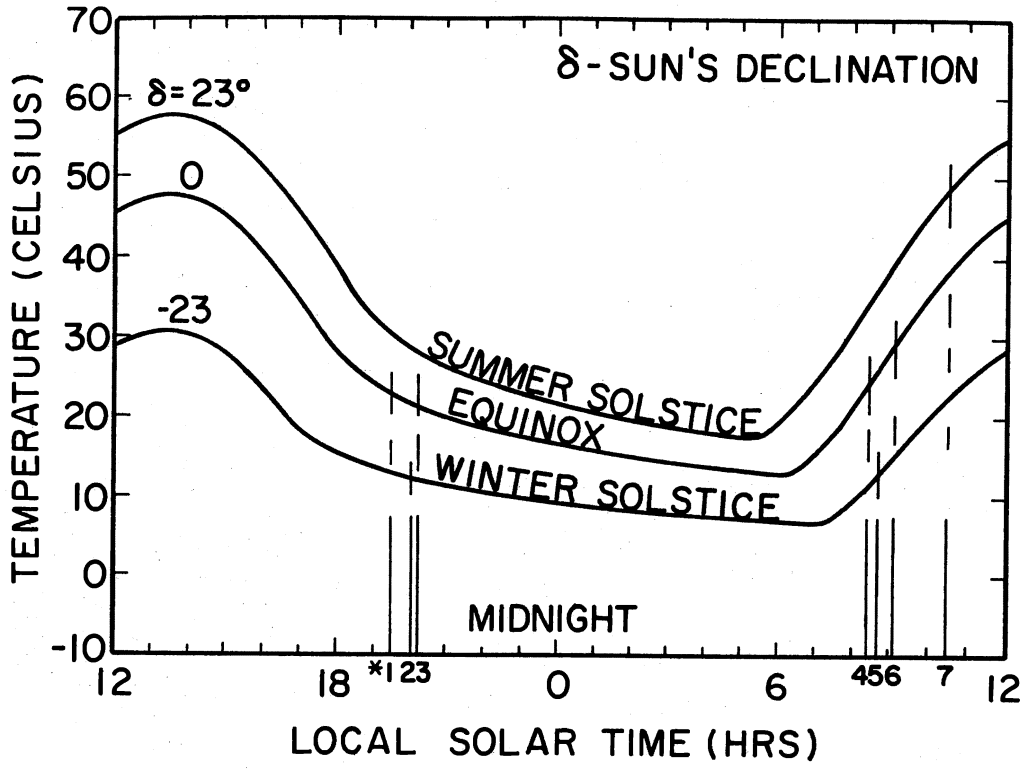

*Data Sets:

1	=	September night	5	=	December day
2	=	January night	6	=	October day
3	=	October night	7	=	June day
4	=	September day			

| indicates scan time of data sets (intersection indicates season obtained).

Source: Watson, K., L. C. Rowan and T. W. Offield. "Application of Thermal Modeling in the Geologic Interpretation of IR Images." Proceedings of the International Symposium on Remote Sensing of the Environment, Vol. III. Ann Arbor, Michigan: University of Michigan, 1971, p. 2028.

Figure 9. Diurnal Surface Temperature Variation Computed for Different Seasons at 30°N Latitude. The Effect of Seasonal Change Is Due to the Dependence of Insolation on the Sun's Declination Which Affects Both the Amplitude of the Incident Solar Flux and the Time of Sunrise and Sunset. Noon 12 Hours, Midnight 0 Hours.

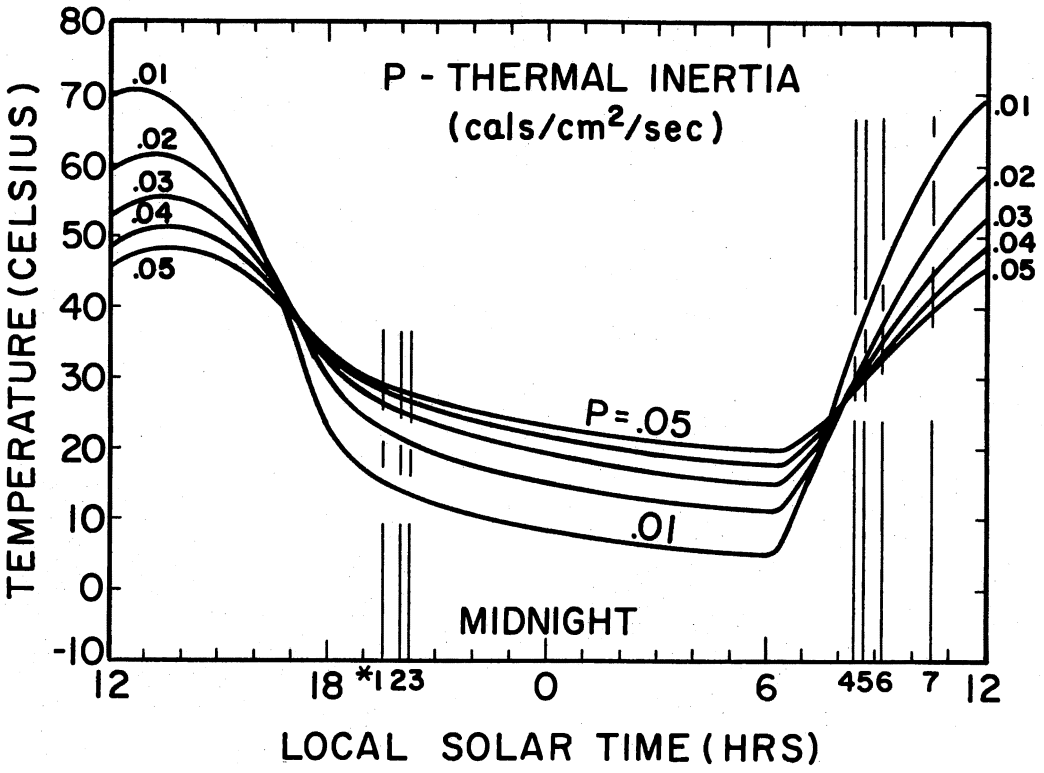

*Data Sets:

1	=	September night	5	=	December day
2	=	January night	6	=	October day
3	=	October night	7	=	June day
4	=	September day			

| indicates scan time of data sets (intersection indicates range of most thermal inertias (.03 to .05))

Source: Watson, K., L. C. Rowan and T. W. Offield. "Application of Thermal Modeling in the Geologic Interpretation of IR Images." Proceedings of the International Symposium on Remote Sensing of the Environment, Vol. III. Ann Arbor, Michigan: University of Michigan, 1971, p. 2027.

Figure 10. Diurnal Surface Temperature Variation With Local Solar Time Computed From Model for Materials With Different Thermal Inertias. Thermal Contrast Is Greatest 1 Hour After Local Noon; Maximum Nighttime Contrast Occurs at Dawn.

diffusivity. The thermal inertia range of most rock and soil types (dry and moist) found within the test site was between ($\sim$.03 and $\sim$.05) (Here a low thermal inertia indicates an "impedance" to the rate of heat transfer through a material. Consequently surfaces of materials with a low thermal inertia will have a high daytime and a low nighttime temperature associated with them. The reverse is true for materials with a high thermal inertia.)

If we plot the scan times on Figure 10 with intersections of the above range of thermal inertias we can determine the differential temperature ranges between data sets due to this property alone. Assuming all other properties (atmospheric, seasonal and material) constant the temperature differential between night edits due to P_i (.03 to .05) is $\sim 5^{o}C$. Likewise between day edits this range is $\sim 17^{o}C$; if the June day case is omitted this drops to $\sim 8^{o}C$, and between the day/night cases (October day reference) this differential is $\sim 13^{o}C$. Since thermal inertia is a local property, there is no reason to believe that its time-dependent effects on the difference temperature observed at a location between two data sets can be removed by simply eliminating the average temperature component present between scenes.

In the microwave portion of the spectrum the remotely sensed temperature of an object is dependent on the antenna characteristics, as well as the temperatures of the radiating object and the sky which surrounds it. For simplicity if we eliminate the angular dependence of the emissivity and reflectivity and assume the earth's surface is opaque to microwave energy transmitted through it from the subsurface (i.e., $\varepsilon_g T_g = 0.0$), then the brightness temperature of an object at the antenna is given by:

$$T_B = \rho_g T_s + \varepsilon_g T_g + \varepsilon_a T_a + \rho_g T_a \quad , \tag{A.8}$$

where ε_a = the emissivity of the atmosphere; and

T_a = the absolute atmosphere temperature;

ρ_g = the reflectivity of the object;

ε_g = the emissivity of the object;

T_s = the absolute sky temperature; and

T_g = the absolute ground temperature.

If the sky is cloud-free then the last two terms in eq. A.8 vanish and we have:

$$T_B = \varepsilon_g T_g + \rho_g T_s \; . \tag{2.3}$$

While the emissivities of many natural materials in the thermal IR portion of the spectrum (specifically between 8μ-14μ) are between .85 and .99 (Leeman, et al., 1971), no general rule holds for these properties in the microwave region. (In the thermal IR region a well known example of emissivity change (known as reststrahlen) between 8μ and 12μ occurs in silicate rock where ε varies with SiO_2 concentration. As the SiO_2 percentage increases the emissivity minimum magnitude shifts to shorter wavelengths.) Though emissivities of materials in the microwave region often do not exhibit large variations as a function of wavelength, one noticeable natural exception, water, exists. Schaerer (1974) reported a difference in the emissivity of water of .25 between microwave wavelengths of 3cm (.38) and 3mm (.63). In addition to this the sky temperature (T_s) in the microwave region increases due to the absorbing atmosphere below λ = 1.5cm. T_s is approximately 3°K for $\lambda > \sim$ 1.5cm but can increase to 40°K or more under clear sky conditions at 3.26 mm (Schaerer, 1974).

In the thermal IR region commonly used in remote sensing ($8\mu \rightarrow 14\mu$) surface roughness is generally >> λ; thus effects due to polarization are minimal. In the microwave region, however, the wavelength range of commonly utilized scanning frequencies is between 3 cm $\leq \lambda \leq$ .13 cm. Here polarization effects can become significant as λ may be much larger than the surface roughness of the object being scanned. In fact, these effects are often so great in the microwave region that receiving antennas are scanned in a horizontal or vertical polarized mode. Brightness temperatures thus obtained as a function of incidence angle and polarization mode can yield information of the angular dependence of the emissivity and reflectivity of the observed materials. Metallic objects, however, have reflectivities $\simeq$ 1.00 under most angles of incidence and modes of polarization. In addition to this, materials with high dielectric constants, such as water (ε_r = 81) have reflectivities $\simeq$ 1.00.

Kennedy (1975) found that brightness temperature--angle of incidence curve shapes for dry soils were dominated by emissivity while those for damp soils were governed by reflectivity. The microwave brightness temperature for both polarization modes is thus a function of water content. The changes in brightness temperature with changes in water content are not linear, but appear to be complex functions of the composite dielectric coefficient of soil and water. In addition to this the reflectivities of water and snow are significantly different in the microwave region. This is primarily due to the large differences in the complex dielectric constants between these materials caused by significant differences in their densities (as much as a factor of 10).

Both thermal IR and microwave wavelength intervals are affected by atmospheric and environmental conditions as is all of the electromagnetic spectrum. Attenuation from a dry non-aerosol atmosphere is low in both microwave and thermal IR windows commonly utilized in remote sensing. This is not true in general for these types of electromagnetic radiation, but regions of low absorption (or high transmission) through the atmosphere exist between $\sim 9\mu \rightarrow\rightarrow 12.5\mu$ (ONR, 1965) in the thermal IR; above 1.67 cm (below 18GHZ), at $\sim$.86cm (35 GHZ), and $\sim$.32 cm (94 GHZ) in the microwave (Hooper and Seybold, 1974). Because of this, most remote sensing measurements that utilize the atmosphere only as a transmission medium are made in these windows. Some regions in the thermal IR are utilized, however, to determine atmospheric temperatures as a function of altitude (NOAA-1, 1972, pp. 41-45). Narrow, high absorption bands in the 13.4μ to 15.0μ range act as blackbodies at the ambient temperatures of particular altitudes in the atmosphere. Since all energy reaching these bands at their respective altitudes and wavelength interval is reradiated upward because of the blackbody properties they possess, accurate atmospheric temperature measurements at selected altitudes can be made by this technique.

These bands are directly related to molecular absorption in both the thermal IR and microwave intervals and limit the electromagnetic transmission in these regions. In the thermal IR and microwave windows (previously noted) which are commonly used for remote sensing, however, atmospheric absorption and emission effects are generally small enough that adequate corrections can be made.

The effects of aerosols, both water and non-aqueous on remote sensing data are, however, more difficult to quantify. In general with

aerosols, as the diameter of the particle increases to the scanning wavelength, the attenuation increases until the diameter approaches or surpasses the scanning wavelength. Broadly speaking, because of this fact, aerosol penetration increases with wavelength for a constant particle diameter. Hence in fog or clouds, visible, thermal IR, short wavelength microwave and longer wavelength microwave (in order of increasing λ) should have the greatest degree of penetration. This observation is demonstrated in Table XI, where the attenuation decreases rapidly with increased scanning wavelength. In each spectral case, signal attenuation is caused by absorption and scattering, and is a complex function of several atmospheric and physical factors.

TABLE XI

ELECTROMAGNETIC RADIATION ATTENUATION THROUGH FOG AND CLOUDS AT SEA LEVEL IN A HORIZONTAL PATH

Visibility		Optical (0.4-0.7μm) (dB/km)	Infrared (8-12μm) (dB/km)	Microwave Band	
Feet	Meters			94 GHz (dB/km)	37 GHz (dB/km)
500	152	120	24	0.88	0.19
1,000	305	60	12	0.32	0.062
2,000	610	30	6	0.13	0.022
4,000	1,219	15	3	0.044	0.009

Source: Hooper, J. O., and J. B. Seybold, "Microwave Radiometric Images", In Remote Sensing of Earth Resources, Vol. 3--Proceedings of the Third Conference on Earth Resources Observation and Information Analysis System, Tullahoma, University of Tennessee, p. 178.

Even microwave wavelengths, however, can be severely attenuated by large dimension cloud droplets. Because of this, microwave attenuation (particularly shorter wavelengths) increases noticeably with increased droplet diameter and precipitation activity.

Water vapor affects electromagnetic radiation in atmospheric windows by producing an anomalous signal attenuation. In microwave regions this factor is often small (as shown in Table XI in the highest visibility case) but in the thermal IR it can be significant, and hence must be computed and removed. In addition, in portions of the microwave region, the sky temperature can be strongly influenced by water concentrations present in cloud cover as shown in Table XII. Consequently, microwave brightness temperature measurements should always be referenced to the sky temperature and cloud cover; particularly if ε_g or ρ_g are being investigated.

Temporal effects occur in both thermal IR and microwave imagery. In thermal IR data the ground temperature varies with time of day due to differential heating and cooling, which is related to sun angle and intensity (Reeves, 1975). Seasonal effects arise due to differences in the sun angle, which causes differential heating in different areas, and due to vegetation changes such as drying and trampling (Reeves, 1975). Microwave imagery is not devoid of diurnal and seasonal effects either. From eq. 2.3 it is apparent that materials with high emissivities will produce diurnally and seasonally varying brightness temperatures as a function of their absolute temperatures. This generally will be related to material with low water porosity or concentrations, as the term $\rho_g T_s$ is minimized.

TABLE XII

THE EFFECT OF METEOROLOGICAL CONDITIONS ON T_s AT λ = .326 CM

Brightness Temperature (°K)	Weather Condition	Air Temperature °Centigrade	Humidity
40-80	Clear sky	25-30	50-60
80-120	High clouds/cirrus	20-26	50-60
120-200	Medium and low clouds/ stratus strato cumulus/ altocumulus	16-20	50-60
200-240	Dark thunderstorm clouds	10-15	60-70

Source: Schaerer, G., A Comparison of Thermal Imagery at Microwave and Infrared Wavelengths, Bern University; for Swiss Department of Military, NTIS Number N76-10553, June, 1974, p. 12.

From the previous material it appears that both microwave and thermal IR remote sensing data have relative disadvantages and advantages to each other for use as in experimental applications. As was shown, even though thermal IR cloud and fog penetration is significantly bettern than that in visible wavelengths it is never-the-less at least one to two orders of magnitude less than that available in microwave wavelengths. In addition, both thermal IR and microwave imagery can be affected by diurnal and seasonal factors. One drawback to current microwave imagery is, however, due to poor systems resolutions compared to those available in the thermal IR region. Specifically, when a small antenna is used the angular resolution (specifically, the crosstrack ifov, $d\nu$) of a microwave system is diffraction limited, and

is approximately given for an aperture diameter D and an operating wavelength λ by:

$$d\nu \tilde{=} \lambda/D \quad . \tag{2.4}$$

Since physical antenna size is often a problem better resolutions can be achieved at shorter wavelengths. Thus a trade-off exists between improved resolution at small λ, and decreased weather penetration and atmospheric transmission (except in small windows) when compared to longer λ. In addition to this the effective resolution is also dependent on the SNR present. In the microwave region the antenna acts as a low-pass filter and the higher spatial frequencies associated with smaller objects are attenuated by the antenna to the point of being obscured by the system noise (Moore, 1975).

In example, the angular resolution of the NOAA-3 vhrr scanner is .60 milliradians; substantially larger than state-of-the-art in thermal IR systems design. Using the microwave system described by Moore (1975), the maximum resolution for a rectangular aperture is given by 1/8 of the the 3db beamwidth and the current resolution is 1/5 of the 3db beamwidth. Given the 3db beamwidth of 1.1^{o} the best possible resolution is 2.40 mr and the current resolution is 3.84 mr, or four to six times worse than the vhrr system utilized.

In addition, brightness temperature images scanned at one microwave wavelength may not be identical to those scanned at another wavelength even for the same resolution element sizes. This is primarily due to changes in ε_g and T_s as a function of λ. In data (Scharer, 1974) for ε_{water} (.83 at 3 cm and .63 at 3 mm) and T_s ($3^{o}K$ at 3 cm and $40^{o}K$ at 3 mm) the difference in computed brightness temperature for water at

λ = 3 cm and λ = 3 mm under a clear sky using eq. 2.3 is $\sim 86^{o}K$. In addition to this, soil moisture content is the dominant reflectivity factor in natural terrain. Hence large differences in brightness temperatures can be observed in (moist) soil when viewed simultaneously by two microwave radiometers at different λ values as well as between identical soils of differing moisture at the same microwave scanning wavelength. The latter point has been experimentally verified in at least two examples (Kennedy, 1975). In the first case at λ = .811 cm a 1% soil moisture change produced brightness temperature changes of between $.7^{o}K$ and $.8^{o}K$ (depending on the angle of incidence). In the second example at λ = .882 cm a 1% soil moisture change produced a brightness temperature change of $\sim .8^{o}K$. For large soil moisture variations this factor can have a significant effect on the perceived brightness temperature and hence the thermal signature of the site in the microwave region.

Kennedy et al. (1966) investigated the brightness temperature--angle of incidence properties of several natural materials, including beach sand. In one set of measurements a 15 minute shower approximately one hour before the investigation was made caused an $\sim 50^{o}K$ decrease in brightness temperature at λ = 2.222 cm versus a similar observation taken the day before the rainfall.

Since soil porosity and drainage are local properties that may vary significantly over a test site, the microwave spectral signature of an area is sensitive to the amount of soil moisture present; particularly after precipitation. Consequently, this may be a limiting factor in utilizing microwave data for a real time correlation system, since significant local thermal signature changes between registered

sets would lead to decreased correlation. Adequate correlation may be obtainable at airborne altitudes if man-made features are present because of the high reflectivity and negligible porosity of metals. At satellite altitudes, however, man-made features are overshadowed in area by the terrain and would be of little or no use in a correlation system. Large free-standing water bodies, such as oceans or lakes, might be needed to insure an acceptable degree of correlation if significant temporal soil moisture changes occur in the scene terrain.

Soil moisture will also affect thermal IR data since the signal is related to the thermal properties of the upper fraction of the terrain, and influenced by the subsurface thermal properties and history. Water tends to drain and evaporate out of the upper fractional region rapidly, but because it has a moderate thermal inertia (a measure of the rate of heat transfer at an interface between two dissimilar media), it can have an influence on the temperature of the surface (ground). In fact, the thermal inertia of both loose (sandy) and compact (clay) soils increases significantly with increases in soil moisture content. This tends to decrease daytime surface temperatures and increase those during the night. In addition to this, evaporative cooling from the added moisture present will lower the surface temperature both in the day and night. The overall effect of both of these factors will be to cause a decrease in the daytime surface temperature and a slight increase in the nighttime temperature. Thus, the effect of water as soil moisture on the observed temperatures in the thermal IR as in the microwave portions of the spectra depends on several factors; including the amount present (as moisture), thermal properties of the surface and the depth of location. These effects on the thermal IR scanned temperature,

however, will generally be much less than on the microwave brightness temperature.

APPENDIX B

NON-LINEAR REGISTRATION ERROR SOURCES

Geometric distortions identified in the data used in this work were principally due to topographic and scan angle effects, and rotation and curvature of the earth relative to the satellite platform. Roll errors were not detected in the test site data utilized, but in a few instances were identified in portions of a data frame outside the region used. Again, X and Y refer to untransformed along-track lines and cross-track columns (pixels) respectively, and U and V refer to transformed lines and columns respectively. In both cases elements are addressed in matrix (location) notation; i.e., the +j element of the +i row would be (X_i,Y_j) in old coordinates and (U_i,V_j) in new coordinates from the (0,0) location.

The topographic errors present were due to neglecting terrain (elevation) variations in the data, and appeared as a cross-track error in the untransformed scene. Hence in the transformed data the primary component will be in columns (V), but a smaller line error component (in U) will also exist. The effective ground displacement due to neglecting topography is given by (Baker and Mikhail, 1975, pp. 53-55):

$$\Delta E_d = Z_e \tan \alpha \qquad (B.1)$$

where ΔE_d = the resulting displacement at ground scale in the untransformed data,

α = the radiometer scan angle, and

Z_e = the element elevation relative to the datum.

The displacement may become appreciable at large scan angles (i.e., $\geq 45^{o}$). In this work, however, the largest scan angle encountered to a vertex in the transformed data scene was 26.47^{o}, and the resulting topography displacement errors were generally ≤ 1 column in the worst case. This error was noticed when potential g.c.p.'s were obtained from high elevation mountain peaks in the north and west portions of the test site and used with lower elevation (desert) g.c.p.'s to determine mean transformation coefficients. A resulting column displacement (in addition to that due to scan angle effects and curvature) was observed at the high elevation points, and in severe cases they were eliminated from consideration as g.c.p.'s.

The data is discrete along-track due to the forward motion of the satellite in its orbital plane, and cross-track due to the radiometer scanning through a fixed ifov. From Legeckis and Pritchard (1976):

> Since the vhrr scan rate (W) is constant, equal increments ($d\alpha$) of the scan angle (α) subtend unequal distances along a scan line. Since the data sampling rate (S) is also constant, these geometric distortions appear in all standard vhrr images as a contraction of the Earth's features at an increasing distance from nadir.(p. 5).

A redistribution algorithm was developed by Legeckis and Pritchard (p. 7) to remove this error from the data. This algorithm was available but not used, since a goal of this work was to simulate a real-time correlation system where such preprocessing would be very costly. Instead an analysis was performed to find the extent of along-track and cross-track distortions present in the data utilized. To compute the magnitude of these non-linear distortions it is first necessary to determine the maximum and minimum cross-track and along-track pixel spacing

spacing and dimensions that occur in each scene. The cross-track pixel dimension and spacing (neglecting terrain elevation variations) can be computed as follows. The scanner-earth scene representation is given by Figure 11 where cylindrical coordinates are applicable.

The first step is to find Redγ in terms of the scan angle α. From Figure 11 we have:

$$\gamma + \beta + \alpha = 90^{o} \quad , \tag{B.2}$$

and

$$\beta = \cos^{-1}\left[\left(\frac{Re + Ho}{Re}\right)\sin\alpha\right] \quad , \tag{B.3}$$

so that

$$\gamma + \cos^{-1}\left[\left(\frac{Re + Ho}{Re}\right)\sin\alpha\right] + \alpha = 90^{o} \quad , \tag{B.4}$$

or

$$\gamma = 90^{o} - \alpha - \cos^{-1}\left[\left(\frac{Re + Ho}{Re}\right)\sin\alpha\right] \quad . \tag{B.5}$$

(For NOAA-3 data $\left(\frac{Re + Ho}{Re}\right) = 1.237$.) By differentiating eq. B.4 we get:

$$d\gamma = -\left[d\left[\cos^{-1}\left[1.237\left[\sin\alpha\right]\right]\right] - d\alpha \quad , \tag{B.6}$$

which reduces to

$$d\gamma = \frac{1.237\cos\alpha\, d\alpha}{\sqrt{1 - (1.237)^{2}\sin^{2}\alpha}} - d\alpha \quad . \tag{B.7}$$

Combining terms in eq. B.7 gives:

$$d\gamma = \left[\frac{1.237\cos\alpha}{\sqrt{1 - (1.237)^{2}\sin^{2}\alpha}} - 1\right] d\alpha \quad . \tag{B.8}$$

Multiplying both sides of eq. B.8 by R_e gives the equivalent cross-track spacing distance (C_S) between pixels as a function of α. Similarily if we replace the value of $d\alpha$ in eq. B.8 by $d\nu$, and again multiply both sides by R_e, we have the cross-track pixel dimension (C_D) as a function of α, since $d\nu$ is also a scanner constant.

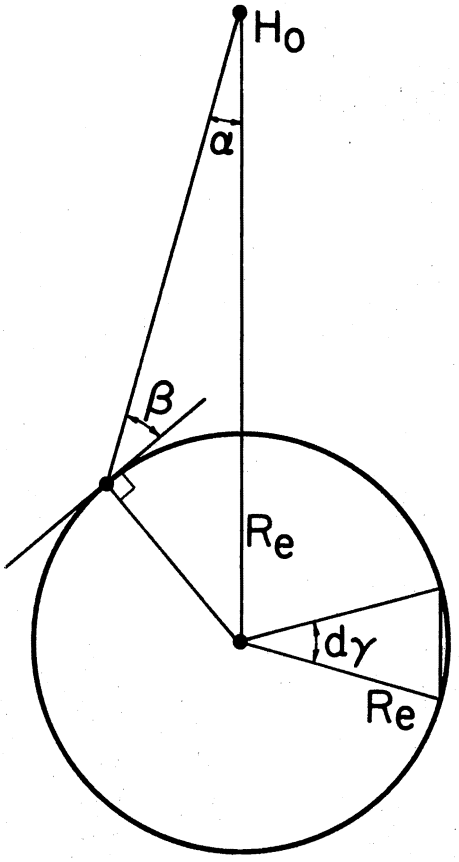

Where H_o = radiometer altitude (1508 Km);

R_e = radius of earth (6371 Km);

α = radiometer scan angle;

β = target angle to radiometer;

γ = earth center angle;

$d\alpha$ = differential scan angle (.3927 mr);

$d\upsilon$ = cross-track ifov of scanner;

$d\gamma$ = differential ground pixel angle; and

$Red\gamma$ = effective cross-track differential ground distance in terms of pixel spacing ($d\alpha$) or length ($d\upsilon$).

Figure 11. Representation of Scanning Geometry

Values of cross-track pixel spacing and length (actually the ifov length) computed for representative scan angles are given in Table XIII. At $\alpha = 0$ and at the subsynch lines the computed values for pixel spacing and length agree closely with observed ones (Legeckis, 1976). Beyond the subsynch lines the values for both these factors increase rapidly with scan angle.

TABLE XIII

COMPUTED NOAA-3 VHRR CROSS-TRACK SPACING AND LENGTH VERSUS SCAN ANGLE

α	Pixel Spacing (Km)	Pixel (ifov) Length (Km)
0^o	.593	.906
5^o	.599	.916
10^o	.619	.945
15^o	.654	.999
20^o	.708	1.081
25^o	.788	1.205
32.76^o	1.001	1.530
40^o	1.407	2.150

If curvature is neglected (commonly done at airborne attitudes), the cross-track pixel dimension relationship reduces to:

$$C_D = d\nu \, H_o \sec^2 \alpha \, . \qquad (B.9)$$

If eq. B.9 is utilized at satellite altitudes, however, significant error due to neglecting curvature will occur. A similar relationship exists to determine the along-track dimension in the data. (Here curvature effects are not included, since the earth scene is treated in cylindrical coordinates.) The relationship is given by:

$$A_D = (ds)H_o \sec \alpha \tag{B.10}$$

where A_D = along-track pixel dimension, and

ds = along-track ifov of scanner. (In vhrr data ds = $d\nu$ = .60 mr.)

The along-track spacing distance in NOAA-3 vhrr data is given by (Legeckis):

$$A_S = L_D \cos \gamma \tag{B.11}$$

where A_S = the along-track spacing; and

L_D = the distance between scan lines at nadir. (L_D is a constant for fixed satellite period and yaw angle, and for NOAA-3 data is .876 Km.)

The largest scan angles at transformed boundary vertices in this work were found in orbit 8477 data and equal to 26.47^o and 15.48^o. The maximum percent variations of A_D and A_S within this data scene computed by eqs. B.10 and B.11 were found to be 7.66% and .50% respectively. Similarly for C_D and C_S computed from eq. B.8 the maximum variation was 24.47%. Computing C_D from eq. B.9 produced a 15.90% variation; hence the component due to curvature between these two methods was 8.57%. From the above, the variation of $C_D > A_D$ and $C_S >> A_S$, and the

curvature effect at scan angles encountered in this case was significant.

Clarification is given here between the significance of A_D, A_S, C_D, and C_S. In a linear geometric transformation the pixel spacing distances (A_S and C_S), and not the pixel dimension distances (A_D and C_D) determine the scale factor of the imagery. If resampling is utilized then pixel dimensions can effectively be altered by intensity recomputation. The only effect on the data of varying A_D and C_D will be to change the amount of pixel overlap in the along-track or cross-track dimension. Increasing this pixel overlap can have a smoothing effect in the data.

To compute the along-track or cross-track pixel spacing, or the error introduced in linear transformation by neglecting the non-linear factors present, it is first necessary to determine the scan angle at the desired points. The scan angle is present in the untransformed data in the cross-track direction only. Hence, it is sufficient to compute Y (old columns) from U (new lines) and V (new columns) by eq. 2.10. The scan angle at the desired location in Y can then be determined from (Phinney, 1975):

$$\alpha = 32.76 + (Y_1 - SI)(65.52)/Y_0 \qquad (B.12)$$

where α = the radiometer scan angle,

Y_0 = the number of pixels (columns) between subsynch lines,

Y_1 = the number of pixels (columns) to the first (closest) subsynch line, and

SI = the sample (pixel) number (Y calculated from eq. 2.10).

Given the scan angles at the transformed data vertices, the registration error in the transformed data due to neglecting the non-linear scan angle and curvature effects can be calculated. The first step is to determine the ratio of the cross-track pixel spacing at the two untransformed vertices. Here, an untransformed vertex refers to a point in (X,Y) that will form a vertex in the transformed data scene (in U,V). Of the four vertices that exist, only two are of interest in the untransformed data. Specifically, they are located at the maximum and minimum scan angles of any points that will be contained within the transformed scene. If scan angle and curvature effects did not exist then this ratio would approach unity, and scale factor errors due to these sources would disappear. Since a mean scale factor is utilized in linear geometric registration, the resulting transformation error due to scan angle and curvature effects will increase as the ratio decreases from a maximum value of unity.

If C_{S1} and C_{S2} are the pixel spacings at the two vertices where $C_{S1} > C_{S2}$, then the relationship between these spacings and the mean spacing is given by:

$$\overline{C}_S + \Delta = C_{S1}$$

and

$$\overline{C}_S - \Delta = C_{S2}$$

where $C_{S1} - C_{S2} = 2\Delta$; and

Δ = the incremental spacing distance.

The exact form of the ratio of C_{S1} and C_{S2} is thus given by:

$$R = \frac{C_{S1} + C_{S2}}{2C_{S2}} = \frac{\bar{C}_S}{C_{S1}} = \frac{\bar{C}_S}{(\bar{C}_S + \Delta)}$$

$$= 1 - (\frac{\Delta}{\bar{C}_S}) + (\frac{\Delta}{\bar{C}_S})^2 - \ldots \quad . \tag{B.13}$$

Since a linear transformation was used in this work for geometric registration, the linear approximation of the ratio (R) utilized was:

$$R_{approx} = \frac{2C_{S2}}{C_{S1} + C_{S2}} = \frac{C_{S2}}{\bar{C}_S} = (\frac{\bar{C}_S - \Delta}{\bar{C}_S})$$

$$= 1 - (\frac{\Delta}{\bar{C}_S}) \quad . \tag{B.14}$$

From eqs. B.13 and B.14 the difference between R and R_{approx} lies in the higher order terms. Having determined C_{S1} and S_{S2} from eq. B.8 (where C_{S1} will be on the side of the test site with the largest scan angle from nadir), R_{approx} was computed from eq. B.14.

The maximum spacing error in the transformed data (due to approximating the non-linear scale factor with scan angle by a linear (mean) one) is produced at the vertices of the registered data scene. In the untransformed data, however, due to rotation these vertex locations will generally not be at the same pixel location from the scene center. (Although the scene center point will remain in the same location in either case if measurement errors in determining g.c.p.'s are not significant, the vertex locations in X and Y will be different from those in U and V.) Consequently, though the location of the points in U (±142 lines) and V (±190 columns) are known, a technique is needed to find the distance from the test site center in X and Y. Since we are

only interested in the magnitude of the maximum distance from center, the sign of the locations in U and V can be neglected.

The relationship between coordinate systems can be derived from eqs. 2.9 and 2.10, where X and Y are determined in terms of U and V. To compute the location from scene center of a point in X and Y in terms of a known location from scene center in U and V the relationships are given by:

$$X_c = \left[\frac{\bar{a}_1}{\bar{a}_1\bar{b}_2 - \bar{a}_2\bar{b}_1} U_c - \frac{\bar{b}_1}{\bar{a}_1\bar{b}_2 - \bar{a}_2\bar{b}_1} V_c \right] \tag{B.15}$$

and

$$Y_c = \left[\frac{-\bar{a}_2}{\bar{a}_1\bar{b}_2 - \bar{a}_2\bar{b}_1} U_c + \frac{\bar{b}_2}{\bar{a}_1\bar{b}_2 - \bar{a}_2\bar{b}_1} V_c \right] \tag{B.16}$$

where X_c and Y_c = the line and column distances from scene center in old coordinates, and

U_c and V_c = the line and column distances from center in new coordinates.

Equations B.15 and B.16 are equivalent to:

$$X_c = \bar{d}_1 U_c + \bar{d}_2 V_c \tag{B.17}$$

and

$$Y_c = -\bar{c}_2 U_c + \bar{c}_1 V_c \quad . \tag{B.18}$$

Equations B.17 and B.18 as given are valid for day orbit data. Because of the differences in scanner-scene aspect angles produced by the day (descending) and night (ascending) satellite orientations, the signs of $\bar{d}_2$ and $\bar{c}_2$ in eqs. B.17 and B.18 are reversed in the night case, while those of $\bar{d}_1$ and $\bar{c}_1$ remain the same. The derivation

employed in eqs. B.17 and B.18 was verified by computing $\bar{c}_1$, $\bar{c}_2$, $\bar{d}_1$ and $\bar{d}_2$ (from $\bar{a}_1$, $\bar{a}_2$, $\bar{b}_1$ and $\bar{b}_2$ obtained from "TRNSFM") from the appropriate terms in eqs. B.15 and B.16 and comparing these mean coefficients to ones ($\bar{c}_1$, $\bar{c}_2$, $\bar{d}_1$ and $\bar{d}_2$) generated directly by solving the simultaneous equations in "TRNSFM". In all day and night cases, the coefficient values determined from the two methods were identical.

Since along-track scan angle and curvature effects (in X) are negligible, the maximum spacing error (at the vertices) due to cross-track effects (in Y) in the transformed data is given by:

$$EU_{max} = \bar{b}_1 Y_{ver} \left(\frac{1 - R_{approx}}{2}\right) \tag{B.19}$$

and

$$EV_{max} = \bar{a}_1 Y_{ver} \left(\frac{1 - R_{approx}}{2}\right) \tag{B.20}$$

where EU_{max} and EV_{max} = the maximum new transformed line and column errors due to neglecting the non-linear scan angle and curvature effects present in the data; and

Y_{ver} = the column distance from scene center to the vertex contained in the transformed data (and hence is the maximum value of Y_c for points within the transformed scene, (U,V)).

The factor of two is needed since the mean scale error is present in the registered data; at the center this error is zero, while at the vertices this error is a maximum. The value of Y_{ver} is computed from eq. B.16 where $U_c = U_{ver}$ = 142 lines and $V_c = V_{ver}$ = 190 columns. Values of α_{max} (at C_{S1}), α_{min} (at C_{S2}), X_{ver}, Y_{ver}, R_{approx}, EU_{max} and EV_{max} at the vertices of the seven data scenes are given in Table XIV. The total number of untransformed lines (X) and columns (Y) contained

in the transformed scene are given by $2X_{ver}$ and $2Y_{ver}$ respectively. Similarly, the maximum differential spacing error (in U and V) between data sets can be determined. This is of interest in change detection since it is necessary to know the minimum cell size in which individual observations can be made. In fact, this minimum cell size can be estimated as ΔEU_{max} lines by ΔEV_{max} columns, and thus is conservative over a large area, since the spacing errors decrease toward the center of the site. The maximum differential line (ΔEU_{max}) and column (ΔEV_{max}) spacing errors for difference sets analyzed were computed from EU_{max} and EV_{max} values in Table XIV and presented in Table XV.

TABLE XIV

MINIMUM AND MAXIMUM SCAN ANGLES, MAXIMUM POSITION, SCALE RATIO AND MAXIMUM SPACING ERRORS FOR TRANSFORMED DATA VERTICES

Orbit	α_{min}	α_{max}	X_{ver} (lines)	Y_{ver} (columns)	R_{approx}	EU_{max} (lines)	EV_{max} (columns)
2590	12.19°	24.55°	182.67	247.27	.895	4.71	10.27
8477	15.48°	26.47°	187.64	243.66	.891	4.24	10.72
8483	-11.64°	-22.81°	243.52	247.70	.912	5.92	8.43
8874	-12.78°	-25.08°	222.29	247.14	.892	5.89	10.57
8880	13.47°	25.48°	189.07	240.85	.891	4.42	10.78
9481	1.37°	13.36°	227.05	240.03	.962	1.62	3.73
9859	6.49°	18.75°	223.48	245.83	.932	3.12	6.72

The largest differential spacing errors encountered in the differencing analyses were present between the October and December day scenes. This was caused by the large difference in scan angles between the two observations over the test site.

TABLE XV

MAXIMUM DIFFERENTIAL LINE AND COLUMN ERRORS PRESENT IN DIFFERENCE SETS (Equivalent to the Minimum Cell Size)

Reference	Test	$\pm EU_{max}$ (lines)	$\pm EV_{max}$ (columns)
8874	2590	1.18	.30
8874	8477	1.65	.15
8874	8483	.03	2.14
8874	8880	1.47	.21
8874	9481	4.27	6.84
8874	9859	2.77	3.85
8880	8483	1.50	2.35
8880	9859	1.30	4.06

The total random line and column error between two data sets can also be determined. This is often of interest since it represents the best possible registration between two data sets even after redistribution to eliminate scan angle and curvature effects. When redistribution has not been employed the total line and column errors present

between data sets are simply the total random line and column errors, plus the line and column differential spacing errors respectively. Specifically, this is given by

$$TRLE_1^2 = TLE_1^2 - \Delta EU \tag{B.21}$$

and

$$TRCE_1^2 = TCE_1^2 - \Delta EV \tag{B.22}$$

where $TRLE_1^2$ and $TRCE_1^2$ are the total random line and column errors between data sets at a given location;

TLE_1^2 and TCE_1^2 are the total line and column errors between data sets at that location; and

ΔEU and ΔEV are the differential line and column spacing errors between data sets at that location.

The values of TLE_1^2 and TCE_1^2 can be approximated at a given location by performing a subscene crosscorrelation between the two data sets centered around the region in question. If the subscene region does not contain isolated thermal anomalies far from center, then the shift location of the magnitude peak provides a good estimate of these total errors.

The differential line and column spacing errors can be computed in manner similar to that previously presented in eqs. B.12 through B.20. In fact, the only difference here will be that the location of interest will generally not be at the vertices, and hence, $EU \leq EU_{max}$ and $EV \leq EV_{max}$. (Specifically $Y_c \leq Y_{ver}$, and R_{approx} must be recomputed from the location of interest in Y to the opposite vertex. Since this location will generally be closer to the center of the scene than a vertex, the resulting ratio will be greater than that obtained (i.e., it will

be closer to 1.00) between the two vertices.) Once these variables are known, the total random line and column errors between the data sets at a given location can be computed.

Another distortion present in the untransformed data is due to the rotation of the earth during the time the satellite transverses the test site. This will be present in the data as an along-track and cross-track distortion, most of which, however, can be removed by linear geometric registration. A rectangular test site will appear as a parallelogram with elongation in both along-track and cross-track dimensions which are parallel and perpendicular to the orbital direction of the scanner. Specifically, the displacement of the earth parallel to the orbital plane in the time interval between two adjacent scan lines is given by (Legeckis and Pritchaird, 1976, pp. 10-11):

$$K_2 = \frac{2\pi R_e}{T_r W} \cos Q \qquad (B.23)$$

where K_2 = the parallel displacement, between two adjacent scan lines;

T_r = the earth's rotational period (23.9345 hours);

Q = the angle of inclination in retrograde of the satellite's orbital plane (78^o);

R_e = the radius of the earth (6371 Km); and

W = the radiometer scan rate (6.667 rev/sec).

Similarly the perpendicular component is given by:

$$K_1 = \frac{2\pi R_e}{T_r W} \cos\theta \sin[\cos^{-1}(\frac{\cos Q}{\cos \theta})] \qquad (B.24)$$

where K_1 = the perpendicular displacement between two adjacent scan lines, and

θ = the angle of the latitude.

(Note that K_2 is independent of latitude.)

The number of displaced pixels in a given scene along-track is given by:

$$Disp_a = \frac{(N_a)K_2P_sW}{2\pi R_e + K_2P_sW} \qquad (B.25)$$

where $Disp_a$ = the along-track displacement in the data due to the earth's rotation;

N_a = the total number of scan lines (X) in the data transformed to (U,V); and

P_s = the satellite period (116.2 min.).

Similarly, in the cross-track dimension:

$$Disp_c = \frac{(N_a)K_1P_sW}{2\pi R_e + K_2P_sW} \qquad (B.26)$$

where $Disp_c$ = the cross-track displacement in the data due to the earth's rotation.

Since K_1 is a function of latitude, $Disp_c$ will also vary with latitude. This will introduce a non-linear distortion in the data since the test site lies between boundaries of different latitudes. The magnitude of this distortion is related to the difference between the boundary latitudes and the location of the site. (The greatest variation/degree of latitude change occurs near the poles; the least, near the equator.) This can be realized from the fact that the component of the earth's velocity cross-track to the scanner varies with latitude,

and hence the scanner-earth track appears distorted. The non-linear distortion present in the data is given by:

$$\Delta Disp_c = [Disp_c(\theta_1) - Disp_c(\theta_2)] \quad (B.27)$$

where $\Delta Disp_c$ = the difference in cross-track displacements between test site boundary latitudes; and

$Disp_c(\theta_1)$ and $Disp_c(\theta_2)$ = the cross-track shift at the test site boundary latitudes ($\theta_1 < \theta_2$).

Worst case values of $Disp_c(\theta_1)$, $Disp_c(\theta_2)$, $\Delta Disp_c$ and $Disp_a$ were computed from eqs. B.25 thru B.27 for orbit 8483 (largest N_a of any scene) data where the total number of lines in (X) present in (U,V) = 2(243.52) or 487.04. Here $Disp_c$ (32°) = 31.860 pixels, $Disp_c$ (35°) = 30.709 pixels, $\Delta Disp_c$ = 1.154 pixels, and $Disp_a$ = 8.058 pixels. Since mean coefficients are used to register the data around a center point the actual value of $\Delta Disp_c$ present in the transformed scene will be one-half this or ±.576 pixels.

The average $Disp_c$ component and the entire $Disp_a$ component can be removed by linear geometric registration if a sufficient along-track and cross-track "spread" of g.c.p.'s exists to determine representative registration coefficients. If g.c.p.'s are determined from a local region within the test site, sufficient translation information may not be contained to remove these components.

The non-linear cross-track distortion ($\Delta Disp_c$) is present in transformed data sets after a linear registration, but it is constant between data sets since the site latitude boundaries are fixed. Consequently, for any point-by-point analysis between multiple data sets

(such as differencing or crosscorrelation) from the same site, this distortion will have a negligible effect.

APPENDIX C

FORMATS FOR TRANSFERRED, TRANSFORMED AND DIFFERENCED DATA

Raw or temperature converted data transferred by "UNSPEC" utilizes the following format. Here, records are unformatted with record length and blocksize of 3240 bytes in PL1 single precision. It is possible in this case to transfer up to 800 pixels per record in sub-blocks of 4 ($L \leq 4$). When the number of transferred pixels per record is not an integer multiple of 200, sub-blocks are filled beginning with L = 1 to the end of data. The remaining space within a sub-block and/or remaining sub-blocks are zeroed out. In example, if 500 pixels/data line are to be transferred, L = 1 and 2 are filled; L = 3 is filled half way, with the remaining 100 locations zeroed; and L = 4 is zeroed out. (This assumes that a full storage of 200 pixels/sub-block is utilized.)

In addition, each data word is stored in an array of four positions (originally designed for LANDSAT data with four spectral channels); thus a word would be represented as Data (word number, 4). Since the data used here comprised a single spectral channel it was stored in position one, with positions two, three and four zeroed. In addition to this, ten single position trailer words as Data (dummy number, 1) are stored at the end of each sub-block of data; even though their values are zeroed. These trailer words were intended to carry calibration data but were not used in this work. Hence each sub-block

of 200 words contains 200 (4) + 10(1) = 810 bytes or a maximum of 200 pixels from the single spectral band data used in this work. Furthermore, since these trailer words are only included to "fill out" the record length they are not included for pixel numbering purposes in the data. In example, data words 200 and 201 would be stored in positions 797 to 800 (sub-block 1) and 811 to 814 (sub-block 2) respectively.

Within a sub-block the data is arranged in consecutive order. Consequently, if the first two pixels of the second data record had (energy) values of 220 and 230 they would be represented as:

220.0	0.0	0.0	0.0	230.0	0.0	0.0	0.0
(1,1)	(1,2)	(1,3)	(1.4)	(2,1)	(1,1)	(2,3)	(2.4)
WORD 1				WORD 2			

within the first sub-block. From this it can be seen that a sub-block is given by:

$$\text{Data (word number, 4)}\Big|^{i=1 \text{ to } 200 \text{ by } 1},$$

plus

$$\text{Data (dummy number, 1)}\Big|^{i=201 \text{ to } 210 \text{ by } 1}.$$

Since there are four sub-blocks per 3240 byte record (810 times 4) the resulting transferred record appears as 4((200,4) + (10,1)) or 3240 positions. Hence, sub-block one begins and ends on positions one and 810 respectively, sub-block two on positions 811 and 1620 respectively, sub-block three on positions 1621 and 2430 respectively, and sub-block four on positions 2431 and 3240 respectively. In addition, sub-block one begins and ends on data words one and 200 respectively, sub-block two on 201 and 400 respectively, sub-block three on 401 and 600 respectively and sub-block four on 601 and 800 respectively.

The above process of sub-block storage is repeated for the total number of data lines present. Hence, if 100 data lines were transferred with 800 non-zero pixels/data line there would be 4(100) or 400 total sub-blocks of data, 400 (810) or 324,000 total data positions and 100 (800) or 80,000 total non-zero data elements. In addition to this, since it is necessary to provide for a numbering system for line printer output, a header record is placed at the beginning of each of the four sub-blocks present. The first line number of the desired scene is in position one, first pixel (column) number of the desired scene in position two, the total number of lines to be transferred in position three and the total number of pixels per sub-block to be transferred ($\leq$ 200) in position four (always $\equiv$ 200 in this work). Values for positions one thru three of the header record are determined from the photographic imagery.

Consequently, for the above example of 100 data lines transferred, the header record would be record number one in the transferred scene, the first data line would be in record number two,(skipping to the end), and the last data line (number 100) would be in record number 101. To use the numbering information on the header record it is only necessary to read the first word (four positions) on the first sub-block and bypass the rest of the record, then begin reading data on record two. For very small scenes numbering may not be necessary; hence one could bypass the entire first record, but on moderate or large scenes line and column numbering is highly desirable to remove possible location errors in measurement. Finally, all data transferred to an output tape in this work employed the IBM Standard Label (SL) numbering process. In example, if two data sets were transferred consecutively to a

clean output tape, the first one would have Standard Label number one (1,SL) and the second, Standard Label number two (2,SL). For atmospheric corrected, temperature converted data T_c (^oC) is obtained by subtracting 123.00 from the given value at a (U,V) location. This constant was incorporated to insure that no negative values would occur in the LARS-II format data. (There was no provision for a minus sign in the 8 bit-byte data word storage.)

For geometrically registered data transformed by "NOAATR" or "NIGHT" the format utilized is similar to that given for data transferred by "UNSPEC". In fact, there are only two major differences in the format. Again, in this case records are unformatted with record length and blocksize of 3240 bytes in PL1 single precision. In addition, there are four sub-blocks of 200 words (800 positions + 10 trailer word positions) present per record, and the first record in the transformed scene is the header record. Word and position numbering within a sub-block is identical to that used for transferred data by "UNSPEC".

The first variation from the "UNSPEC" transferred data format is in the first word (four positions) of the header record. Here the first line number of the transformed scene is in position one, first pixel (column) number of the transformed scene in position two, the total number of transformed lines in position three and the total number of columns in position four. The first word of sub-blocks two, three and four is that given to the transferred data by "UNSPEC", and consequently remains unchanged after registration. Hence only the first word of sub-block one should now be utilized as a numbering marker for transformed data, since this information will be different from that given in the untransformed (transferred) data case.

The second variation lies in the number of transformed data lines lines stored per record. In this work the total number of pixels per transformed line was 380. Consequently, two lines of transformed data are stored per record. Here, the first 200 data words are stored consecutively in sub-block one, and the next 180 data words are stored consecutively in sub-block two. The remaining 20 data words in sub-block two are zeroed out, as are the 10 single position trailer words per sub-block. Sub-blocks three and four are used to store the next line of transformed data. In example, if four lines of data (380 pixels per line) are transformed the resulting output format would be as follows. Record number one (header) would contain the necessary marker information, record number two would contain lines one (in sub-blocks one and two) and two (in sub-blocks three and four) and record number three would contain lines three (in sub-blocks one and two) and four (in sub-blocks three and four). The 284 transformed lines of data used in this work were thus stored in [(284)/2 + 1] total records. Consequently, when reading in transformed data from a tape, a provision is needed to unstructure the records into data lines of the transformed array.

The computed intensities (temperatures) from the bilinear interpolation algorithm may not be integers. As before, only position one of a given data word can have non-zero magnitudes since the single spectral form is still (obviously) present. Standard Labels are again used to separate data sets on output tapes as in the transferred data case. Again, T_c is obtained from the interpolated data at a given (U,V) location by subtracting 123.00 from the indicated value.

The differenced output from "NOAADIFF" utilizes the same format as that used for transformed data, except in this case there are four computed values per data word (or one per position). (Since differencing

is only performed on transformed data, the resulting header record, number of data lines (two) and sub-blocks (four) per output record, and the number of points per line remain the same as in the transformed data case.) The values in the first and second positions per data word are the straight and mean-biased difference (signs and) magnitudes between a reference and test data set for a given point in (U,V). The values in positions three and four of the data word are the straight and mean-biased difference classes (boundaries given in Table IV) between the reference and test data sets at the same point in (U,V). (Here the values in data word positions three and four are integer numbers between one and seven and represent the ΔT class (seven different classes) a given point in (U,V) between reference and test sets will have.) In this case the first word in each sub-block of the header record contains the information of the first word of the first sub-block of the transformed data. Specifically, the first position of each word is the first line number, second position is the first column number, third position is the total number of lines and fourth position is the total number of columns.

APPENDIX D

ANALYSIS OF PERTURBATIONS PRESENT BETWEEN 30×30 POINT SUBSCENES

An attempt was made to determine whether thermal perturbations between subscene (30×30 pixel Palo Verde Valley) crosscorrelation pairs were correlated or not. There were three possible cases that could be analyzed: the June, September and December day case; the September day, October day and October night, day/night case; and the September, October and January night case. Each point in the 30×30 subscene was considered as a coordinate of a dimension 900 "vector", and here we were only concerned with the "scene" component and removed the average temperatures by subtracting the mean. The crosscorrelation in each case can be expressed as the direction cosine between test (t) and reference (r) vectors as shown in Figure 12.

Thus, the crosscorrelation between t_1 and r was given by $t_1 \cdot r = |t_1||r|\cos\theta_A$, between t_2 and r as $t_2 \cdot r = |t_2||r|\cos\theta_B$, and between t_1 and t_2 as $t_1 \cdot t_2 = |t_1||t_2|\cos\theta_{AB}$. (For this analysis it was convenient to label the June day, September day and September night subscenes as t_1; the September day, October day and October night subscenes as r; and the December day, October night and January night as t_2 in the respective day, day/night and night cases.

If the vectors t_i contain a portion of r; i.e., $t_i = (\alpha_i * r) + (\beta_i *$ perturbation) then the crosscorrelation is fixed for t_i lying anywhere

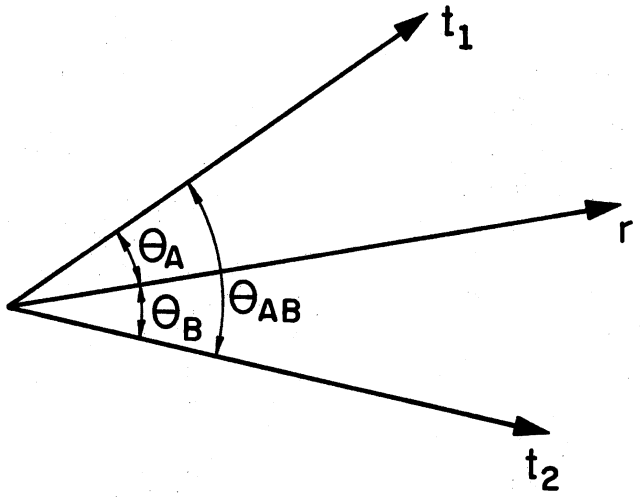

Figure 12. Representation of Reference and Test Subscene Vectors

on a cone of the same angle θ_i; where r is the axis of the cone and t_i is a ray on the cone. Here t_1 and r would form a plane and t_2 and r would form a second plane. The cone thus describes the possible locations of t_2 to the plane defined by t_1 and r. If the perturbation vectors are uncorrelated then $(t_1 \cdot t_2)/|t_1||t_2| = (\cos \theta_A)(\cos \theta_B) = \cos \theta_{AB}$. By definition in this case the perturbation from r to t_1 would be perpendicular to the perturbation from r to t_2.

From the above diagram the minimum value of $t_1 \cdot t_2$ occurs when θ_A and θ_B (or t_1 and t_2) are on opposite sides of r and the maximum value of $t_1 \cdot t_2$ occurs when θ_A and θ_B (or t_1 and t_2) are on the same side of r. If the perturbation that carries r to t_1 is uncorrelated with that from r to t_2, then the two perturbations are at right angles and the dot product between them is zero. In this case $\cos \theta_A \cos \theta_B = \cos \theta_{AB}$. Hence the similarity between the crosscorrelation of t_1 and t_2 subscenes and the expected product of $(\cos \theta_A)(\cos \theta_B)$ is an indication of whether or not the thermal perturbations present are uncorrelated.

In the day case analyzed $\frac{t_1 \cdot r}{|t_1||r|} = .8217$, $\frac{t_2 \cdot r}{|t_2||r|} = .7178$ and $\frac{t_1 \cdot t_2}{|t_1||t_2|} = .6012$. The product of the first two is .5898 or +1.90% below the actual value of $\frac{t_1 \cdot t_2}{|t_1||t_2|}$. The maximum crosscorrelation possible in this case was .9866 = $[\cos(\theta_A - \theta_B)]$ while the minimum crosscorrelation possible was .1930 = $[\cos(\theta_A + \theta_B)]$. In the day/night case analyzed $\frac{t_1 \cdot r}{|t_1||r|} = .6764$, $\frac{t_2 \cdot r}{|t_2||r|} = .4288$, and $\frac{t_1 \cdot t_2}{|t_1||r_2|} = .6263$. The product of the first two is .2900 or 53.70% below the actual value of $\frac{t_2 \cdot t_2}{|t_1||t_2|}$. The maximum crosscorrelation possible in this case was .9554 = $[\cos(\theta_A - \theta_B)]$, while the minimum crosscorrelation possible

was $-.3754 = \cos(\theta_A + \theta_B)$. In the night case $\frac{t_1 \cdot r}{|t_1||r|} = .8609$, $\frac{t_2 \cdot r}{|t_2||r|} = .8415$ and $\frac{t_1 \cdot t_2}{|t_1||t_2|} = .7975$. The product of the first two is .7244, or 9.17% below the actual value. The maximum crosscorrelation possible in this case was $.9993 = [\cos(\theta_A - \theta_B)]$ and the minimum cross-correlation possible was $.4496 = [\cos(\theta_A + \theta_B)]$.

From this analysis it appears that the perturbations present in the day and night cases were only weakly correlated. In the day/night case the perturbations were neither highly correlated nor were they uncorrelated; in fact, the observed magnitude of $\frac{t_1 \cdot t_2}{|t_1||t_2|}$ was $\simeq$ $[\cos(\theta_A - \theta_B) + \cos(\theta_A + \theta_B)]$ and $\simeq$ the average of the magnitude of the two extreme values. Since each perturbation was caused by a combination of factors (i.e., meteorological, material and seasonal effects) then from these few observations there is no evidence to suggest that they are predictable and can be compensated for.

APPENDIX E

ANALYSIS OF ATMOSPHERIC AND GROUND TEMPERATURE GRADIENTS

Air temperature gradients determined from NOAA-EDS data between Needles and Yuma (north→south) and Daggett and Yuma (northwest→southeast) near scan times were computed by simple subtraction and given in Table XVI. An evaluation of the atmospheric gradient present via 850 mb charts, known ground temperatures and elevations was also made and given in Table XVII. Here the temperature at 850 mb at a known time, location and elevation was determined and added to the standard atmospheric gradient of 6.5°C/1000 meters to obtain an equivalent air surface temperature. These temperatures were then compared to known ground station air temperatures obtained at the scan time and the (temperature) differences that resulted were reported as inversion (in), slight gradient (sl), normal gradient (nor), and unstable (un).

Both of these analyses were prepared as an aid to interpreting the point-by-point differencing results and were only approximate in nature. In the first case, where (north→south and northwest→southeast) air temperature gradients were given, the Blythe Station was often abnormally warm compared to the other reporting stations. In addition, because of the mountains that surround the Coachella Valley, Salton Sea, and Imperial Valley the northwest→southeast gradient was often inaccurate in this region. Outside this region, however, in most cases

TABLE XVI

NORTH-SOUTH AND NORTHWEST-SOUTHEAST AIR TEMPERATURE GRADIENTS PRESENT AT DATA SCAN TIMES

Orbit	Edit Time and Date[1]	Temperature[1] Observation Time	North-South[2] Gradient (°C)	Northwest-Southeast[3] Gradient (°C)
2590	1031: 4 June 1974	1000	-4.44	-1.11
8477	0823: 21 Sept 1975	0800	2.78	3.33
8483	1923: 21 Sept 1975	2000	1.11	5.00
8874	0907: 23 Oct 1975	0900	2.78	5.56
8880	2009: 23 Oct 1975	2000	2.22	3.89
9481	0833: 11 Dec 1975	0900	-.56	-6.67
9859	1958: 10 Jan 1976	2000	-1.11	4.44

[1]PST (Add 1 hour for Arizona-MST).

[2]Needles-Yuma air recording station temperatures.

[3]Daggett-Yuma air recording station temperatures.

TABLE XVII

ATMOSPHERIC GRADIENT ANALYSIS (GROUND TO 850 MB) OF TEST SITE GROUND TEMPERATURE RECORDING STATION

Orbit	Station						
	Yuma	Blythe	Needles	Daggett	Thermal	Imperial	Zulu Time of Determination
2590	sl	sl	sl	sl	sl	in	12Z 4 June, 1974
8477	sl	nor	sl	sl	sl	sl	12Z 21 Sept, 1975
8483	nor	nor	nor	nor	nor	nor	00Z 22 Sept, 1975
8874	sl	sl	sl	sl	sl	sl	12Z 23 Oct, 1975
8880	nor	nor	nor	nor	nor	nor	00Z 24 Oct, 1975
9481	in	in	in	in	in	in	12Z 11 Dec, 1975
9859	sl	sl	sl	nor	nor	sl	00Z 11 Jan, 1976

in = inversion; sl = slight gradient; nor = normal gradient; un = unstable

it was representative of the ground temperatures present in the thermal IR scanner surface data. A noteworthy exception was the inverted December day scene, where the air temperature increased slightly with elevation while the ground temperature did not. In this case surface temperatures in northwest valleys were actually colder than those in the southeast, but for air temperatures the reverse was true. The other unusual case was the (abnormal) reversed north→south air temperature gradient of the June day scene, where air and ground temperatures in the north were several degrees centigrade warmer than the south.

This negative gradient occurred over most of the test site and since the October day scene had a moderately positive north→south temperature gradient, caused the October/June difference set to have large regions ($3^{o}C$ to $6^{o}C$) below the mean in the north and ($3^{o}C$ to $6^{o}C$) above the mean in the south. This condition (along with anomalies due to the influence of differing scan times on the locally varying thermal inertia present) led to the small population near the average ΔT in this difference set, and the large resulting difference set variance contributed to the low site correlation coefficient in this case.

The atmospheric temperature gradient analysis was limited by two major factors. The first was that data was only available at 12Z and 00Z GMT which is equivalent to 4→5 am and pm respectively (the Arizona side of the Colorado River being one hour later than the California side). Data was scanned 3½ to 6 hours from the nearest available 850 mb reports in some instances. The general trend of this analysis showed that small gradients or inversions were present over the test site (stable atmosphere) at 12Z GMT and normal or unstable conditions

were present by 00Z GMT. Thus, conditions that usually prevailed over the test site favored a positive (ground station to predicted) difference for day edits and a negative difference for night edits. Since the atmospheric temperature gradient changes non-linearly with time due to many factors (seasonal-sun elevation, relative humidity, barometric pressure, etc.) whose effects could not be quantified, the analysis presented was only qualitative in nature. The other factor that reduced accuracy was the necessity to utilize isotherm information from charts since Yuma was the sole reporting ground station (only at 12Z). Here, a linear gradient between 5°C isotherms was assumed, and a non-reporting 850 mb location could be as much as ±2½°C in error.

In the four day edits inspection of atmospheric gradients at 12Z and 00Z GMT revealed that the atmosphere was in order of decreased stability for the December, June, September and October scenes. Likewise for the three night edits at 00Z and 12Z GMT (next day) the order of decreased stability was for the January, October and September scenes.

No attempt was made to quantify ground temperatures with surface station air temperatures at the time the edits were scanned. It was noticed and expected, however, that ground temperatures at the five recording stations were less than the air temperatures at the same locations within the test site for the three night edits. (Daggett was outside the area of the transformed data set.) In some day scene cases, however, air temperatures at recording stations were higher than surface temperatures at the edit scan time, in other cases the reverse was true. This phenomena was influenced by factors such as the time of day and season of edit, material properties and the previous air

temperature history. Additional analysis of air and ground temperatures was beyond the scope of this research.

VITA 2

Edmund Henry Conrow

Candidate for the Degree of

Doctor of Philosophy

Thesis: THE TEMPORAL CORRELATABILITY OF DIGITAL THERMAL INFRARED SCANNER DATA

Major Field: General Engineering

Biographical:

Education: Graduated from Cortez High School, Phoenix, Arizona; in May, 1971 received Bachelor of Science Degree in Nuclear Engineering from the University of Arizona; received Master of Science degree in Nuclear Engineering from the University of Arizona in 1974; enrolled in doctoral program at Oklahoma State University in 1974 and completed requirements for the Doctor of Philosophy degree in December, 1976.

Professional Experience: Participated in laser optics research from 1969-1970 and medical basic science research from 1971-1974 at the University of Arizona, Graduate Student Summer Researcher, Department of Surgery, University of Arizona, 1971, Analytical Chemist, Magma Copper Company, 1972, Instructor; part time and graduate research assistant, Schools of Mechanical and Aerospace Engineering and General Engineering, Oklahoma State University, 1974-1976, participated in auditory physiology, control systems, laser optics and remote sensing research from 1974-1976 at Oklahoma State University.

Professional Societies: AIAA, ASP, IEEE, NSPE, and OSPE.